Spectrally Efficient Modulation Formats for Fast Reconfigurable Optical Networks

Tam N. Huynh

B.Sc., M.Sc.

A Dissertation submitted in fulfillment of

the requirements for the award of

Doctor of Philosophy (Ph.D.)

To the

Dublin City University

Faculty of Engineering and Computing

School of Electronic Engineering

Supervisor: Prof. Liam P. Barry

April, 2014

Declaration

I hereby certify that this material, which I now submit for assessment on the programme of study leading to the award of Doctor of Philosophy (Ph.D.) is entirely my own work, and that I have exercised reasonable care to ensure that the work is original, and does not to the best of my knowledge breach any law of copyright, and has not been taken from the work of others save and to the extent that such work has been cited and acknowledged within the text of my work.

Signed:

Student ID: 58127348

Date:

To my mother,
Thanh Huyen.

Acknowledgements

Firstly, I would like to thank my mother, Thanh Huyen, who is always beside me, encourages me and has been dedicating her whole life for me.

I would like to thank my supervisor, Professor Liam P. Barry, for his initial faith in my ability, and for the support and guidance that he has given me throughout this PhD. Without his continued motivation and support the completion of this work would have been impossible.

I would also like to thank Professor Lim Nguyen, University of Nerbraska-Lincoln for his thoughtful support and encouragement throughout my PhD.

I am indebted to my colleagues past and present, for the role they have played, both academically and socially, in my time with the Radio and Optical Communications Group, Dublin City University, especially Dr. Frank Smyth and Dr. Prince Anandarajah who guided me from the initial steps in the experimental works, and Dr. Josue Parra Cetina who connected me with the Irish social life. I would like to acknowledge Dr. Sean O'Duill for his time and kind help for the preparation of this thesis.

Lastly, I would like to thank Professor Leslie A. Rusch and all my friends in Laval University, Canada for their kind collaboration.

Contents

Abstract

The desire for multi-media content and richly interactive data services is shaping a new era for telecommunications networks. Future networks will need to be capable of offering Triple Play, Internet Protocol Television, Video-on-Demand, Voice-over-Internet-Protocol and High-Speed Internet Access, combined with guaranteed Quality of Service. These networks will employ optical transport networks with wavelength division multiplexing (WDM) technology, and advanced modulation formats, in order to achieve the high capacities required. In addition, given the bursty nature of this data it is expected that dynamic allocation of the bandwidth will be implemented to efficiently use the available capacity. The key component in these networks will be the tunable laser transmitters that generate the different wavelength packets. This thesis has explored novel applications and implementations of the sampled-grating distributed Bragg reflector (SG-DBR) laser, in optical WDM metro, and access networks. Through theory, simulations and experiments, I have investigated the use of SG-DBR lasers for advanced modulation formats in fast reconfigurable optical networks. Firstly, the phase noise properties of the SG-DBR laser and its impacts on coherent optical communications have been intensively characterized. Subsequently, I proposed techniques to overcome these obstacles for advanced modulation format communication systems. Finally, the application of advanced modulation formats in dynamic optical packet switching scenarios employing SG-DBR lasers have been evaluated.

List of Figures

List of Tables

Nomenclature

ADC Analog-to-Digital Converters

ASE Amplified Spontaneous Emission

AWGN Additive White Gaussian Noise

BER Bit Error Rate

BPSK Binary Phase Shift Keying

CO-OFDM Coherent OFDM

CS Cycle Slips

CSP Cycle Slip Probability

DAC Digital-to-Analog Converters

DBR Distributed Bragg Reflector

DD-PLL Decision-Directed Phase-Locked Loop

DFB Distributed Feedback Laser

DFT Discrete Fourier Transform

DLI Delay Line Interferometer

DPSK Differential Binary Phase Shift Keying

DQPSK Differential Quadrature Phase Shift Keying

DSH Delayed-Self Homodyne

DSH-PM Delayed Self-Heterodyne using Phase Modulation Detection

DSP Digital Signal Processing

DWDM Dense Wavelength Division Multiplexing

E-field Electric Field

ECL External Cavity Laser

EDFA Erbium-Doped Fiber Amplifier

ENoB Effective Number of Bits

EVM Error Vector Magnitudes

FEC Forward Error Correction

FIR Finite Impulse Response

FM Frequency Modulation

FM-noise Frequency Modulation noise

FWHM Full-Width-at-Half-Maximum

GCSR Grating-Assisted Coupler with Sampled Reflector

IP Internet Protocol

IQ Modulator Inphase/Quadrature Modulator

ISI Inter-Symbol Interference

LMS Least Mean-Squared

LO Local Oscillator

MAC Media Access Control

MAN Metropolitan Area Network

MAP Maximum a Posteriori

MCF Multi-Core Fiber

MIMO Multiple-Input-Multiple-Output

MLSE Maximum Likelihood Sequence Estimation

MMF Multi-Mode Fiber

MZM Mach-Zehnder Modulator

NRZ-OOK Non-Return-to-Zero OOK

OBS Optical Burst Switching

OFDM Orthogonal Frequency Division Multiplexing

OOK On/Off Keying

OPS Optical Packet Switching

OSA Optical Spectrum Analyzer

OSNR Optical-Signal-to-Noise ratio

OTDM Optical Time Division Multiplexing

OXC Optical Crossconnect

PAPR Peak-to-Average Power Ratio

PD Photo-Diode

PDF Probability Density Function

PDM Polarization Division Multiplexing

PLL Phase-Locked Loop

PM Phase Modulation

PMD Polarization Mode Dispersion

PPG Pulse Pattern Generator

PS-QPSK Polarization Switched QPSK

PSD Power Spectral Density

QAM Quadrature Amplitude Modulation

QPSK Quadrature Phase Shift Keying

ROADM Reconfigurable Optical Add/Drop Multiplexers

RZ-OOK Return-to-Zero OOK

SDM Space-Division Multiplexing

SDN Software Defined Networks

SG-DBR Sampled Grating Distributed Bragg Reflector

SMF Single Mode Fiber

SNR Signal-to-Noise Ratio

SSG-DBR Superstructure Grating Distributed Bragg Reflector

STH Schawlow-Townes-Henry

TIA Transimpedance Amplifier

VOA Variable Optical Attenuator

WDM Wavelength Division Multiplexing

XPM Cross Phase Modulation

Introduction

Due to the exponential growth of the internet traffic (60% every 18 months), the current optical transportation networks are moving towards higher spectral efficiency communications links with lower latency. Coherent detection using advanced modulation formats, accompanied by fast re-configurable optical networks, would enable the ability to achieve this target for future communications networks. In this work, I will extensively investigate the important aspects of fast re-configurable optical networks deploying advanced optical modulation formats. The key component in such a network is the fast-wavelength-switching tunable laser, particularly, the Sampled-Grating Distributed Bragg Reflector (SG-DBR) laser. However, SG-DBR lasers exhibit sophisticated phase noise properties that would significantly impact the performance of systems using advanced modulation formats. This leads to the need for novel signal processing algorithms and transmission methods to tackle the impact of SG-DBR laser phase noise. The main contribution of this research work can be summarized as below.

I firstly proposed and experimentally demonstrated laser phase noise measurement methods to characterize the SG-DBR laser in detail. From the measurement results, I can resolve, and confirm with the theoretical analysis, that the phase/frequency noise of the SG-DBR laser consists of: (1) the Schawlow-Townes-Henry phase noise (random-walk process in phase) with relaxation oscillation above 5GHz; (2) the filtered Frequency Modulation noise (FM-noise) from the dynamics of carriers in passive sections; and especially the low frequency noise including the flicker $1/f$ noise and the frequency random-walk $1/f^2$ noise. The impact of the different phase noise processes in optical communication systems were then carefully examined. I found that the low frequency noise can lead to instability of the system performance while the Schawlow-Townes-Henry phase noise basically defines the lower limit for the Bit Error Rate (BER) performance of the coherent communications systems. I then proposed the use of a second order decision-directed phase-locked loop phase tracking algorithm to overcome this issue in fully optically coherent communications links. I also proposed two novel transmission schemes: the self-heterodyne receiver using phase modulation detection technique, and baudrate-pilot-aided quadrature amplitude modulation transmission scheme with direct detection to effectively overcome the significant impact of the laser phase/frequency noise in the SG-DBR lasers. Finally, the application of the SG-DBR lasers in optical packet switching networks employing advanced modulation formats was carefully examined. The baudrate-pilot-aided quadrature amplitude modulation transmission scheme has proven to be a suitable candidate for such a highly dynamic system.

The structure of this thesis is as follows:

Chapter 1 reviews the current status of the optical communication networks. Firstly, the fundamental limits of the optical communications links will be revised. Advanced optical modulation formats employing coherent detection technique which offers high spectral efficiency and high energy efficiency are reviewed. The current trend in research and development of space division multiplexing systems are also presented. Finally, reconfigurable optical networks and the application of advanced modulation formats in these networks will be discussed.

Chapter 2 re-derives the general Schawlow-Townes-Henry phase noise formula for semiconductor lasers. Based on that I then develop an analytical model for phase noise processes in monolithic tunable lasers with multi-sections, particularly the Distributed Bragg Reflector - style lasers. The complete Frequency Modulation-noise spectrum of a SG-DBR laser is finally formulated.

Chapter 3 proposes and demonstrates the novel delayed-self-heterodyne phase noise measurement method employing the phase modulation detection technique. The proposed method was then compared and confirmed with the conventional delayed-self-homodyne phase noise measurement method employing a coherent receiver. The phase noise measurement techniques were then utilized to extensively study the phase noise processes in different types of semiconductor lasers, especially the SG-DBR lasers.

Chapter 4 examines the laser phase noise issue in advanced modulation format optical communication systems employing monolithic tunable lasers. I firstly investigate the effects of the SG-DBR laser phase noise processes in a coherent optical communication system. The novel phase noise tracking algorithm utilizing a second-order decision-directed phase-locked loop has then been proposed and evaluated. In this chapter, two novel transmission schemes to effectively overcome the problem of phase/frequency noise in SG-DBR lasers are proposed while satisfying the target of high spectral efficiency for communications links: Differential

Quadrature Phase Shift Keying signaling with the coherent-self-heterodyne receiver employing phase modulation detection technique; and baudrate-pilot-aided Quadrature Amplitude Modulation transmission with direct detection scheme.

Chapter 5 investigates the applications of advanced optical modulation formats in the fast reconfigurable optical networking scenario. I found that the performance of a Differential Quadrature Phase Shift Keying system employing the SG-DBR laser for fast-wavelength-switching experiences performance degradation during the wavelength switching event. This performance degradation is examined and discussed through the experimental results. Finally, I confirm that the baudrate-pilot-aided Quadrature Amplitude Modulation transmission scheme with direct detection is a good fit for such an application in optical packet switching networks.

Chapter 6 summarizes and concludes the thesis. Some possible future research directions are discussed at the end of this chapter.

Chapter 1

Optical Communication Networks

Beginning with the pioneering experiment on data transmission over a short glass fiber carried out by Charles K. Kao at the Standard Telecommunication Laboratories - Harlow in 1965, optical communications has developed tremendously over the past 50 years. The photon has manifested itself as the most efficient data transport carrier up-to-date. In this chapter we briefly review some essential constituents of modern optical communication networks. The chapter is as follows. We firstly evaluate the capacity limit of the optical channel employing Wavelength Division Multiplexing (WDM) in section 1.1. In section 1.2, the current status of advanced modulation formats used in optical networks will be reviewed. Re-configurable optical networks are reviewed in section 1.3. We finally present the feasibility of combining advanced modulation formats with re-configurable optical networks to achieve optimum efficiency of resources in the entire optical network in section 1.4.

1.1 Capacity limit of optical fiber utilizing WDM transmission

To evaluate the capacity limit of optical communications over fiber, we start with a brief review on the Shannon limit for communications, particularly for Additive White Gaussian Noise (AWGN) channel [1]. The estimation of channel capacity of optical fiber will be based on considering this limitation with the nonlinear Schrodinger wave equation in the fiber [2, 3, 4, 5].

1.1.1 Shannon limit in communications

The dawn of modern digital communications began with the *Information Theory* proposed by Claude E. Shannon in 1948 [1]. A rigorous derivation of capacity for an AWGN channel was presented in [1, 3]. To describe the capacity, the *entropy* of a transmitting signal X (a random variable) to the channel could be defined as [1, 3]

$$H(X) = \sum_{a} -P_X(a) \log_2 P_X(a) \tag{1.1}$$

where P_X is the probability that the random variable X takes the value a in the modulation constellation. The *mutual information* of the transmitted signal X and received signal Y has been defined as [3]

$$I(X;Y) = H(X) - H(X|Y) = \sum_{a,b} P_{XY}(a,b) \log_2 \frac{P_{XY}(a,b)}{P_X(a)P_Y(b)} \tag{1.2}$$

The capacity of a channel for *reliable communications* is then the maximum mutual information over all possible input distributions $P_X(.)$, i.e. the capacity in bits per symbol is [1, 3]

$$C = \underset{P_x(.)}{max} I(X;Y) \tag{1.3}$$

Theoretically for an AWGN channel with continuous input - continuous output, the equation 1.3 yields a well-known formula of channel capacity in bits per second (or information rate) [1, 3]

$$C = \log_2(1 + SNR) \tag{1.4}$$

where SNR is the Signal-to-Noise ratio. Nevertheless, in a practical communication system, the input constellation used to be a discrete set of symbols that yields a more realistic channel with discrete input - continuous output. Particularly we pay attention to two families of modulation formats named Phase Shift Keying (M-PSK) and Quadrature Amplitude Modulation (M-QAM) where M is defined as the constellation size or the number of points in the modulation constellation. Obviously the maximum capacity of these discrete modulation formats is $\log_2(M)$. Fig. 1.1 illustrates the Shannon limit for an AWGN channel and the capacity for some widely used modulation formats.

1.1.2 The nonlinear Shannon limit of WDM system

Optical communications employing the optical fiber as a nonlinear transmission medium makes it unique to conventional wire-line and wireless communications. In addition to the Amplified Spontaneous Emission (ASE) noise induced by optical amplifiers, the most important propagation nonlinearity of this medium is the

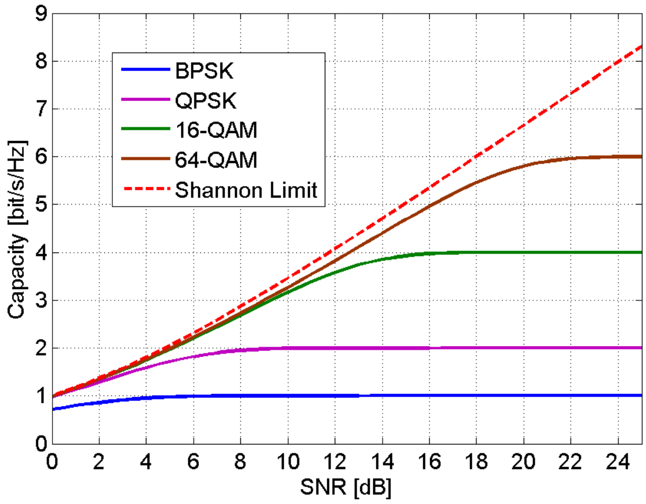

Figure 1.1: Shannon limit for AWGN channel

intensity dependence of the refractive index [2, 3, 5]. In WDM systems, the channel capacity limit is mainly defined by the nonlinearity induced by cross phase modulation (XPM) from the neighbouring channels to the channel-of-interest as argued in [2] and proven in [3, 5]. Following the pioneering work in [2], to estimate the capacity limit of information transmitted over the "*optical channel*", we begin with the Schrodinger equation which governs the evolution of the optical field of the channel-of-interest i in the single mode fiber.

$$j\frac{\partial E_i(z,t)}{\partial z} = \frac{\beta}{2}\frac{\partial^2 E_i(z,t)}{\partial t^2} + V(z,t)E_i(z,t) \tag{1.5}$$

where $V(z,t) = -2\gamma\sum\limits_{k\neq i}|E_k(z,t)|^2$ appears as a random noise term to the channel-of-interest and $E_k(z,t)$ are the independent E-field from the other channels. By introducing a nonlinear intensity scale I_0, the analytic expression for lower-bound C_{LB} to the total channel capacity of the stochastic Schrodinger equation 1.5 can be expressed as [2, 5]

$$C_{LB} = n_c B \log_2\left(1 + \frac{e^{-(I/I_0)^2} I}{I_0 + \left(1 - e^{-(I/I_0)^2}\right) I}\right) \tag{1.6}$$

where $I_0 = \sqrt{\frac{BD\Delta\lambda}{2\gamma^2 \ln(n_c/2) L_{eff}}}$. The parameters in the above equation are: n_c - the number of WDM channels, B - the signal bandwidth in each channel, D - the fiber dispersion coefficient, $\Delta\lambda$ (or Δf)- the channel spacing (in wavelength or frequency) of WDM grid, γ - the nonlinear coefficient of the fiber, the effective length of the system $L_{eff} \approx n_s/\alpha$ where n_s is the number of spans and α is the fiber loss coefficient. Figure 1.2a plots the lower bounds of Spectral Efficiency $SE = \frac{C_{LB}}{n_c \Delta f}$ for the optical fiber versus the input power per channel

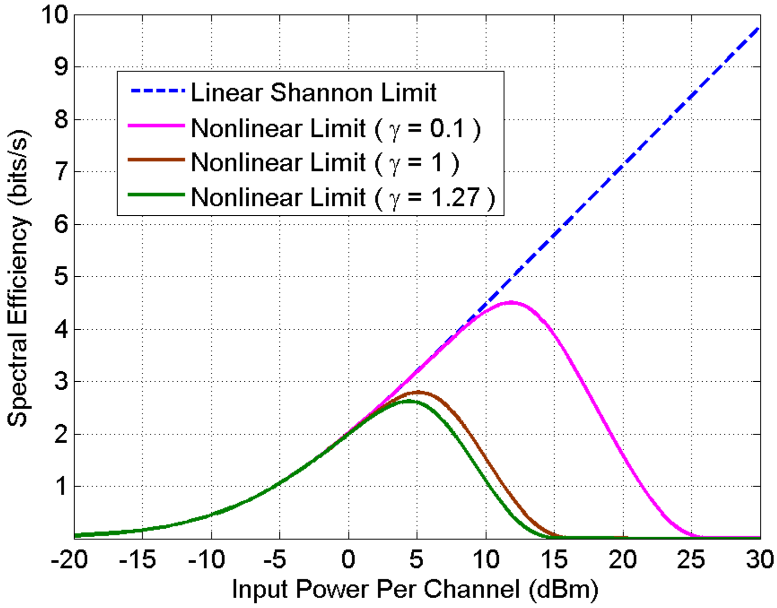

(a) Spectral Efficiency limit with different γ

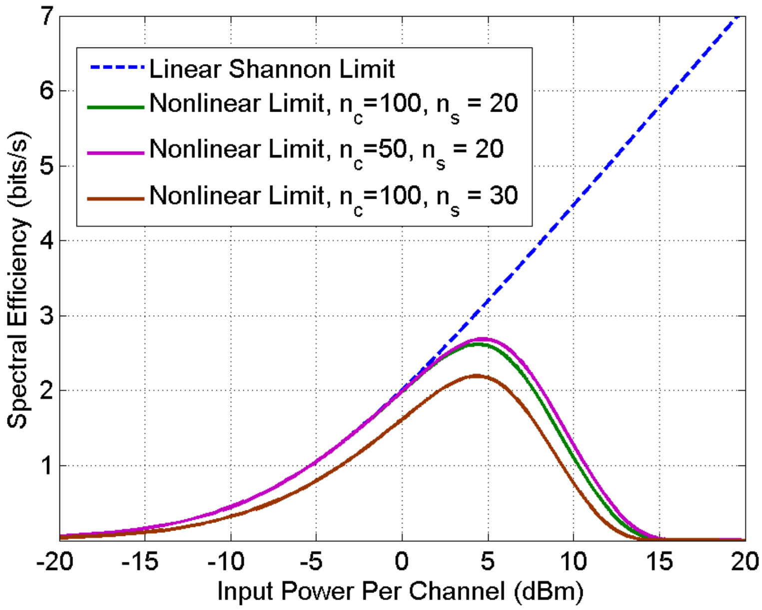

(b) Spectral Efficiency limit with different n_c & n_s

Figure 1.2: The lower bounds of spectral efficiency of nonlinear Shannon limit for optical fiber with $\alpha = 0.2dB/Km$, parameters for WDM system: $B = 40GHz$, $\Delta f = 50GHz$, $n_c = 100$, $D = 17ps/nm/km$, $n_s = 20$ and different values of nonlinear coefficient γ for (a); (b) presents the dependency of channel capacity on system length (or n_s) and number of WDM channel n_c with $\gamma = 1.27W^{-1}km^{-1}$.

with the parameters given below, assuming that all channels have the same input power. Equation 1.6 yields a conclusion that in a WDM system, the channel capacity increases with fiber dispersion, channel spacing, signal bandwidth, and decreases with the number of channels and the number of spans. Figure 1.2b clearly demonstrates this.

Optical-Signal-to-Noise ratio (OSNR): In optical communications, besides the SNR, the OSNR has been frequently used as a measure to manage the quality of signal in transmission. The definition of OSNR differs from SNR by a normalization factor based on the particular choice for the fixed reference noise bandwidth B_{ref}, and how the polarization modes are accounted for. The relationship between OSNR and SNR can be expressed as [3, 4]

$$OSNR = \frac{pR_s}{2B_{ref}} SNR \tag{1.7}$$

where p is the number of polarization modes modulated in transmission, R_s is the symbol rate and B_{ref} is the reference noise bandwidth, usually $B_{ref} = 0.1nm$.

1.2 Review of advanced modulation formats for optical communications

Due to the capacity crunch in Dense Wavelength Division Multiplexing (DWDM) optical networks, and data traffic increasing exponentially by 30 to 60% every year [4, 6], the conventional On-Off Keying modulation format in optical communications is surely not capable of coping with this capacity trend. Advanced optical modulation formats, especially with coherent detection, which offer high spectral efficiency are being increasingly investigated in research and installed in commercial systems from 2012. Fig. 1.3 reviews the evolution of experimentally achieved system capacity and spectral efficiency of advanced optical modulation formats over the last two decades [6]. This section gives an overview of the current status of advanced modulation formats being actively employed in optical communication networks.

1.2.1 High spectral efficiency modulation formats with coherent detection

Coherent detection schemes were intensively studied in the early 1980s due to the high sensitivity of the coherent receiver. However, with the advent of Erbium-

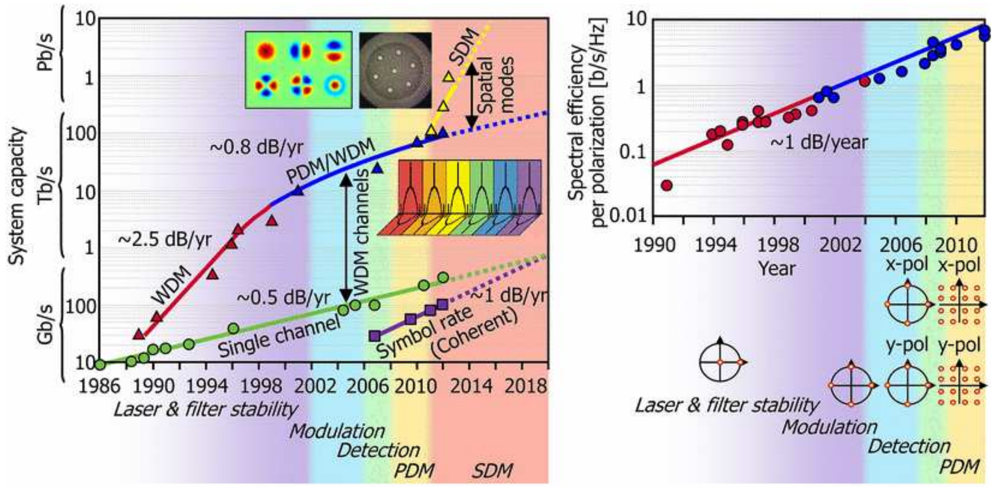

Figure 1.3: The *left figure* summarizes the experimentally achieved single-channel bit rates (single-carrier, single-polarization, electronically multiplexed; green circles), symbol rates in digital coherent detection (purple squares), and aggregate per-fiber capacities (triangles) using wavelength-division multiplexing (WDM; red), polarization-division multiplexing (PDM; blue), and space-division multiplexing (SDM; yellow). Experimentally achieved per-polarization spectral efficiencies in single- (red) and dual-polarization (blue) experiments are also shown in the *right figure*. [6]

doped fiber amplifier (EDFA) in combination with high-capacity Wavelength Division Multiplexing systems, the research and development of coherent systems were interrupted for nearly 20 years [7, 8]. The use of EDFA's and WDM resulted in the significant increase in system capacity in experimental demonstration (about 2.5 dB/year) during the 1990s as observed in Fig. 1.3. Since then, On/Off Keying modulation format (OOK), with its simplicity, has dominated optical communications in the last decades. OOK was also the first modulation scheme used in commercially available products of 40 Gbit/s [9] communication systems and was taken all the way to 100 Gbit/s in research demonstrations [10].

Even though the technical difficulties associated with the bandwidth of electronic components for OOK at 100 Gbits/s were shown to be manageable, it was realized early on that the spectral efficiency of OOK would not be sufficient for future optical transport network, and research on 100 Gb/s started to include higher order modulation formats such as Differential Quadrature Phase Shift Keying (DQPSK) with delay line interferometers (DLIs) and direct detection by 2002 [11, 12]. Recently, 100 Gb/s DQPSK systems was taken to field trials for live HDTV video traffic using the LambdaExtreme platform over 504 Km [13].

Although DQPSK was demonstrated for 100 Gb/s systems, it could only support a 100 GHz channel spacing. For migrating to even higher bitrate and supporting 50 GHz channel spacing (DWDM), higher spectral efficiency modulation formats would be required. The next stage of optical communications has been opened up with high-speed Digital-to-Analog converters (DAC), Analog-to-Digital converters (ADC), digital signal processing (DSP) processor and optical coherent detection. The real and imaginary components of the complex amplitude of the optical carrier could be coherently detected and retrieved with a digital coherent receiver using an optical 90^o hybrid. Modern optical coherent receivers with DSP are built on the intradyne principle where the intermediate frequency falls somewhere within the signal band (because a small frequency offset is consistently introduced between the lasers at the transmitter and the receiver). In addition, polarization division multiplexing (PDM) could be combined with advanced modulation formats to double the spectral efficiency. In this way, 111 Gb/s PDM-QPSK was first demonstrated over 2550 Km for 50 GHz channel spacing DWDM in [14].

With the commercial popularity of Lithium-Niobate based Nested-Mach-Zehnder modulators (I-Q modulator), coupled with polarization/phase diversity optical 90^o hybrids, higher spectral efficiency has been achieved by employing coherent detection with high order Quadrature Amplitude Modulation (QAM) formats [15]. However as observed from Fig. 1.1 the richer constellation of higher order QAM requires the received signal to have higher Signal-to-Noise ratio, and also requires more complicated DSP at the receiver side. The spectral purity of laser source was considered as one of the pronounced obstacles for QAM formats with coherent detection. Recently Polarization-Multiplexed 16-QAM at 224Gbits/s has been reported in [15] using an External Cavity Lasers with narrow linewidth for both transmitter side and local oscillator (LO) at receiver side. Subsequently 32-QAM and 64-QAM for single carrier transmission with DSP-offline has been experimentally reported [6]. Apart from using advanced DSP after coherent detection to overcome the laser phase noise issue, the idea of Phase Locked Loop in RF communications was also adopted in an Optical Phase Locked Loop incorporated by transmitting a pilot tone [16]. In this technique, Nakazawa's group have reported remarkable coherent optical detection of 512-QAM at 54 Gbit/s over 4.1 GHz optical bandwidth using C_2H_2 fiber lasers with extremely low linewidth (4 KHz) [17]. They also combined their coherent QAM systems with Optical Time Division Multiplexing (OTDM) to achieve even higher bitrate with high spectral efficiency. A 400 Gb/s 32 RZ/QAM system was reported over 225 Km on a single carrier at 10 Gsymbol/s $\times$ 4-OTDM in [18].

In parallel with increasing the spectral efficiency by simply using denser constellation, to pack more information bits into a given bandwidth of the C-band (and extended L-band) of the EDFA, researchers have proposed new techniques to reduce the guard bands between the DWDM channels by introducing the *Superchannel* technology [19]. A closely-spaced Superchannel could be formed by : (i) maintaining the orthogonality in the frequency domain of the transmitted sub-channels (subcarriers), and the time-aligned symbols in the temporal domain should satisfy the Nyquist criteria [20]; (ii) spectral confinement with pulse shaping filters in the digital domain [21] or in optical domain [22], namely *Nyquist-WDM*; (iii) or placing multi-band electrical Orthogonal Frequency Division Multiplexing (OFDM) signals [23, 24] on a frequency-locked multi-carrier light source [25]. The first approach also requires a frequency-locked source and an oversampling rate of about 2 samples/symbol [20]. The digital Nyquist-WDM approach employs the digital Nyquist-type filters, such as Raised-Cosine or Root-Raised-Cosine filters, to shape the pulses of the transmitted signals prior to driving the I/Q modulator. In this way the sub-channels can be placed so close as to have a guard band of 1% signal bandwidth, when employing PDM-32-QAM modulation format [21]. In another approach, the authors in [22] proposed to use optical filtering to aggressively confine the spectrum of each sub-channel to a *sub-Nyquist* bandwidth such that a 28 Gbaud PDM-RZ-QPSK signal is constrained in 25GHz bandwidth. This sub-Nyquist signaling induces modulation memory, and symbol-by-symbol detection is in turn not effective anymore. That would require a symbol sequence detection scheme at the receiver such as Maximum a Posteriori (MAP) or Maximum Likelihood Sequence Estimation (MLSE) [22].

In the third approach utilizing coherent OFDM (CO-OFDM), the guard interval presented as cyclic-prefix [24] to protect the OFDM symbol from fiber dispersion can be reduced to increase the total spectral efficiency. As reported with Reduced-Guard-Interval-CO-OFDM in [26], the long memory inter-symbol interference (ISI) from fiber dispersion is compensated prior to OFDM signal processing as done in single-carrier frequency domain equalization, while the remaining reduced-cyclic-prefix is used to accommodate the short memory ISI induced by transmitter bandwidth limitation and polarization mode dispersion (PMD). The well-known issue of high peak-to-average power ratio (PAPR) in Superchannel CO-OFDM has also been attracted research attention and could be mitigated by some addition DSP techniques such as DFT-spread-OFDM [27] adopted from wireless communications. Moreover on applying OFDM-type signals into optical communications, the authors in [28] proposed a novel all-optical OFDM transmitter/receiver configuration which is a high potential for future optical communications applications. The Superchannel technology offers a considerable increase in spectral efficiency with the expense of additional requirements on DAC at the transmitter, ADC at the receiver and advanced DSP.

As discussed, the choice of high spectral efficiency modulation format is not a unique answer and really depends on the system requirements such as channel interface rate, available optical bandwidth, transmission distance, power consumption, transponder complexity, OSNR, etc. Careful consideration of the chosen modulation format is based on some trade-offs [6] in terms of the following issues:

DAC and ADC performance: A single IQ modulator needs two DAC with minimum resolution of $\log_2(\sqrt{M})$ for a M-size constellation, and higher resolution allows compensation for modulator nonlinearity. In addition, oversampling would be required for pulse shaping and OFDM. In a parallel modulators approach enabled by photonic integration [29], the binary driving signals are sufficient. At the receiver side, for a pre-FEC BER of 10^{-3}, the ADC would require approximately 3 bits more than $\log_2(\sqrt{M})$ in terms of effective number of bits (ENoB). With current CMOS technology, a DAC is available for up to 65 GSamples/s with 8-bit resolution and a ADC can achieve 65GSamples/s at 6 ENoB across 20 GHz [30].

Equalization digital filter: Fiber chromatic dispersion is well compensated by applying a digital FIR filter with $T_S/2$ spacing in DSP [31]. However the longer reach and higher system baudrate, equivalent with longer channel memory, would require longer tap lengths of the FIR filter.

Laser phase noise: Semiconductor lasers introduce high phase noise as will be discussed in the next chapters [32]. That significantly limits the choice of constellation size M to achieve higher spectral efficiency [33]. Another important aspect induced from the laser spectral impurity is equalization-enhanced phase noise [34]. The high-speed signals have less tolerant to the laser phase noise in long digital filter for dispersion compensation.

Transmission reach: As observed in Fig. 1.1, denser constellations require higher OSNR or less accumulated ASE over the transmission link. Stronger Forward Error Correction (FEC), coded modulation and/or lower loss fiber could improve the reach with the expense of lower spectral efficiency. Also new fiber design with lower nonlinearity and/or nonlinear distortion compensation techniques such as *Digital Back Propagation* [35], *Phase-Conjugated Twin Waves* [36] would increase the optical launched power and consequently transmission reach.

Spectral confinement: As in the discussion of Superchannels above, with the support of the high speed ADC, DAC and DSP, pulse shaping can confine the transmitted signal spectral and improve the spectral efficiency with the trade-offs of transceiver complexity and an increase in PAPR. *Sub-Nyquist* signaling (or *super-Nyquist* signaling) can be achieved to over-filter the transmitted signal but requires a symbol sequence detection such as MLSE which in turn increases the receiver latency and complexity.

1.2.2 Space-Division Multiplexing: the next dimension to explore

Even with the best effort to push up the transmission capacity (and transmission length) of the single-mode fiber close to the non-linear Shannon limit as recently demonstrated by the experiment that achieved 640 Gb/s PDM-16QAM at 80 Gbaud [37], or the remarkable 101.7 Tb/s transmission with PDM-128QAM-OFDM over 165 Km SMF-28 fiber [38], experimental results have approached the theoretical limit to within a factor of *two* as illustrated in Fig. 1.4 [39]. That clearly shows the current technology utilizing the time-, quadrature-, wavelength (frequency)-, polarization- multiplexing ability of the single-mode fiber would not be able to address the future *optical networks capacity crunch* [40, 41]. In order to overcome this issue, in the last few years, researchers around the world are extensively exploring the last dimension for multiplexing in optical communications: the *spatial dimension* or Space-Division Multiplexing (SDM). SDM can not only solve the issue of capacity crunch but also enables large reduction in cost-per-bit or energy-per-bit [39]. In general, Space-Division Multiplexing falls into two main categories: low-crosstalk SDM over multi-core fiber (MCF) and high-crosstalk SDM over multi-mode (few modes) fiber (MMF) [41, 42].

In the first approach, a new fiber design is proposed with multi-core and each core is essentially an "isolated single-mode fiber". An MCF has each core operating as an independent channel and spatially multiplexing all the cores (channels) to increase the total capacity. To achieve SDM in this case, the mandatory issue that needs to be tackled is crosstalk between the spatial channels especially after fiber transmission. The second issue is how to couple the light into the independent cores with the lowest crosstalk level, so called Fan-In/Fan-Out, given the separation between the cores is very small (30-50 μm). The development of a practical multi-core optical amplifier is the next crucial key to enable this type of system. Recently, transmission experiments of low-crosstalk MCF with 7-core [43, 44], 12-core [45] and 19-core [46] have been impressively reported. The MCF fibers can also be used to generate the *orbital angular momentum* multiplexing signal [47] where the Laguerre-Gaussian modes were chosen for multiplexing instead of

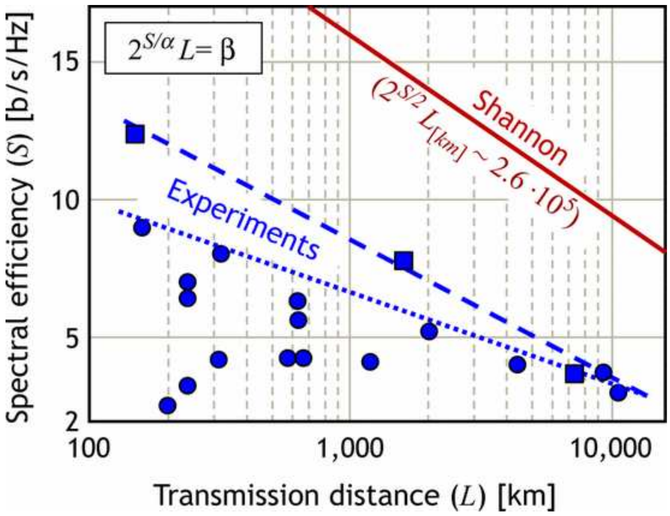

Figure 1.4: Spectral efficiencies versus transmission distances achieved in WDM experiments (circles, dotted line) and in narrowband filtered single-channel experiments (squares, dashed line). The solid line also shows the nonlinear Shannon limit of SMF with PMD. [39]

widely used TEM modes [48].

High-crosstalk SDM is achieved in MMF by selectively exciting, and coherently detecting, the complete orthonormal set of modes with *multiple-input-multiple-output* (MIMO) techniques at the receiver side. The key challenges associated with this system are: (i) the differential group delays in coupled-mode waveguides must be small enough to be handled by MIMO-DSP, (ii) the mode-dependent loss (and/or gain) and noise variation between the modes, (iii) and the complexity of DSP-MIMO receiver. The modal dispersion in MMF is analogous to multipath delay spread in wireless communications and does not fundamentally limit system performance [49], while the mode-dependent loss is analogous to mutipath fading in wireless systems and reduces the MIMO capacity [50]. Various experimental demonstrations of coupled-mode MIMO-SDM transmission have been reported recently, including transmission of six spatial and polarization modes in few mode fiber [51] or in strongly coupled multi-core fiber [52].

1.2.3 Energy efficient optical modulation formats

As outlined in the previous section, the main trend of modern optical communications is to pack more transmission bits into a given optical bandwidth by migrating to higher spectral efficiency modulation formats. However, regarding Fig. 1.1, Shannon's Information Theory [1] tells us that the trade-off of moving to a higher spectral efficiency is the lower energy efficiency of the given modulation format. It also means that with the acceptance of losing spectral efficiency one can improve the power efficiency or receiver sensitivity of a modulation format. In this subsection we review some proposed advanced modulation formats that can improve the receiver sensitivity.

By exploring the nature of two orthogonal polarizations of the complex optical field transmitted in the single mode fiber, some multi-dimensional (3-D, 4-D) modulation formats have been recently proposed to achieve a sensitivity even better than the well-known BPSK format in the ASE limit. Instead of independently modulating the two polarizations as with Polarization Multiplexed - QAM, the Polarization Switched QPSK (PS-QPSK) format has been proposed in [53] to employ the first two bits to modulate the complex E-field as a normal QPSK signal, and the third bit to switch between the two polarizations. In general for an uncoded transmission the PS-QPSK format offers an asymptotic 1.76 dB power efficiency[1] advantage over PM-QPSK (or QPSK, or BPSK) based on sphere packing theory [53, 54]. That leads to the extensive experimental demonstrations of this modulation format to confirm the improvement in receiver sensitivity [55, 56]. Experimental results also show that PS-QPSK is more tolerant to fiber nonlinearity than the widely-deployed PM-QPSK. However, when taking into account a sufficient Forward Error Correction, the authors in [57] argue that with the same data rate, bandwidth and transmit power, PS-QPSK is actually not as efficient as PM-QPSK.

The Pulse Position Multiplexing (PPM) modulation format also offers high sensitivity with of-course the extension in occupied bandwidth. By combining M-ary PPM with PM-QPSK into a new modulation format namely PM-QPSK - 16-PPM (or PQ-16PPM) the authors in [58] experimentally reported a record receiver sensitivity of 3.5 photons per bit[2] (2.5 photons/bit in theory) at $BER = 10^{-3}$ in a 2.5 Gbit/s system employing pre-amplified receivers. A brief summary of theoretical performance of the above modulation formats is given in Table 1.1 [54, 58].

1.3 Review of re-configurable optical networks

In previous sections, we have discussed in detail the optical transmission in a point-to-point link with single carrier or WDM systems. The focus on increasing

[1]The power efficiency of a modulation format is defined as $PE = \frac{d_{min}^2}{4E_b}$, where E_b is the *energy per bit* and d_{min} is the *minimum distance* of the constellation.

[2]In coherent optical communications, the physical interpretation of SNR per bit is $\frac{E_b}{N_0} = \frac{n_b}{N_a n_{sp}}$ where n_b is the average number of photons per bit, N_a is the number of in-line amplifiers with spontaneous emission factor n_{sp}.

Modulation Format	Spectral Efficiency (bits/sym/pol)	Sensitivity @ $BER = 10^{-3}$ (E_b/N_0) (dB)
BPSK	1	6.8
PM-QPSK	4	6.8
16-QAM	4	10.5
PS-QPSK	3	5.8
16-PPM	4	6.7
PQ-16PPM	8	3.9

Table 1.1: Power Efficiency of high sensitivity modulation formats

point-to-point link capacity in combination with electronic switching elements and *optical-electrical-optical* (OEO) transponders was the first phase of optical networking, which is often referred to as the *first-generation* [59]. However, the real advantage of optical networking arises from the ability to reconfigure the entire network directly in the optical layer without involving electronics in the data plane. Hence the *second-generation* of optical networks achieves reconfiguration of the optical circuit by properly configuring the *lightpath* using the optical network elements [60, 61]. With the introduction of EDFAs, reconfigurable optical add/drop multiplexers (ROADMs) and optical crossconnects (OXCs), optical circuit switched networks have become a proven network technology, and are widely deployed in the last decades. However as data traffic keeps increasing exponentially as discussed above, we anticipate the *third-generation* of optical networks will increase the total transport capacity by addressing the switching of *optical data packets* or *optical bursts* directly in the optical layer [60, 61, 62]. The evolution of optical networks is summarized in Fig. 1.5 [59].

Electrons are useful in building up memory devices, but not as effective as a transport carrier. On the other hand, photons have the opposite characteristics. To date all of the electronic switching elements (routers, switches) are based on the efficient *store-and-forward* time processing technology with the utilization of random access memory (RAM) as the buffers. In contrast optical switching technology might tackle the main difficulty posed by the lack of an efficient "*optical memory*" device due to the nature of photons. However, an all-optical router can exploit the wavelength domain to enable switching and contention resolution, and it can also potentially support high line rate multi-wavelength signals in the optical switching fabric with typically much less power and signal interference than its electronic counterpart [61].

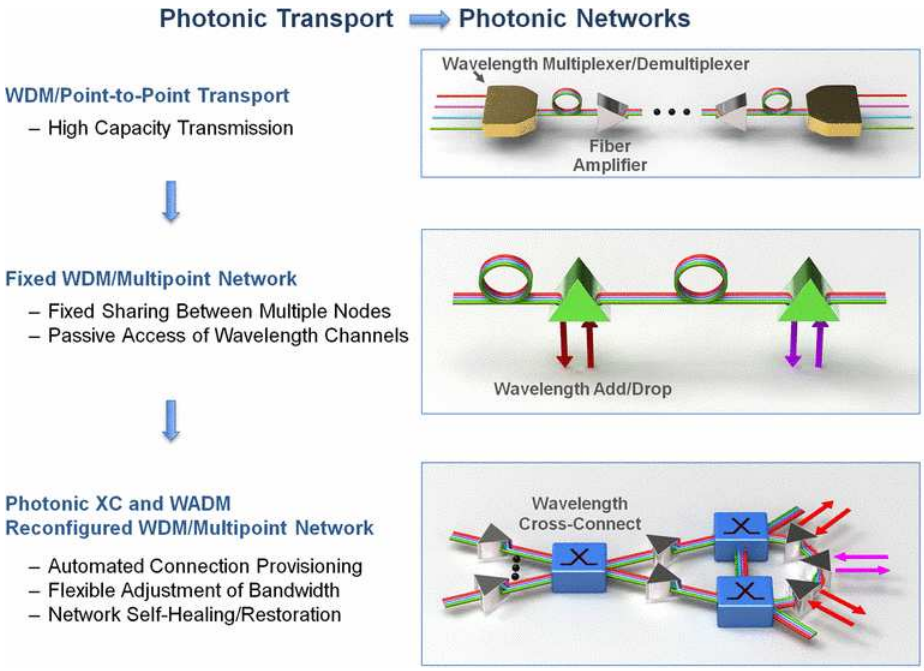

Figure 1.5: The evolution of optical networks. [59]

1.3.1 Switching technology for re-configurable optical networks

As mentioned earlier, re-configurable optical networks maintain the network connections in the optical layer which enables the removal of a tremendous amount of electronic processing from the network, and the attendant cost, power, space, and reliability burdens. Furthermore, all-optical switching elements, by operating on wavelengths, are more scalable than their electronic counterparts [60]. The structures of optical routers with synchronous and fixed-length datagram, or asynchronous with variable-length packets are illustrated in Fig. 1.6 [62]. In the third-generation optical networks, *optical burst switching* and *optical packet switching* technology have been widely investigated in research and development recently. The advantage of optical burst switching compared to conventional optical circuit switching is that it can more effectively accommodate bursty traffic at subwavelength granularity without requiring very fast switching speeds as required with optical packet switching, while optical packet switching seeks to achieve nanosecond switching speeds with much shorter datagram, which in turn significantly enhances the total throughput of the networks. In optical burst switching, firstly, a *burst header cell* (or control data packet) is sent from source to destination on a *control channel* to set up the lightpath, then the data bursts will be transmitted. As a result, the established connection remains in place during the data bursts transmission, and is then torn down afterwards to improve

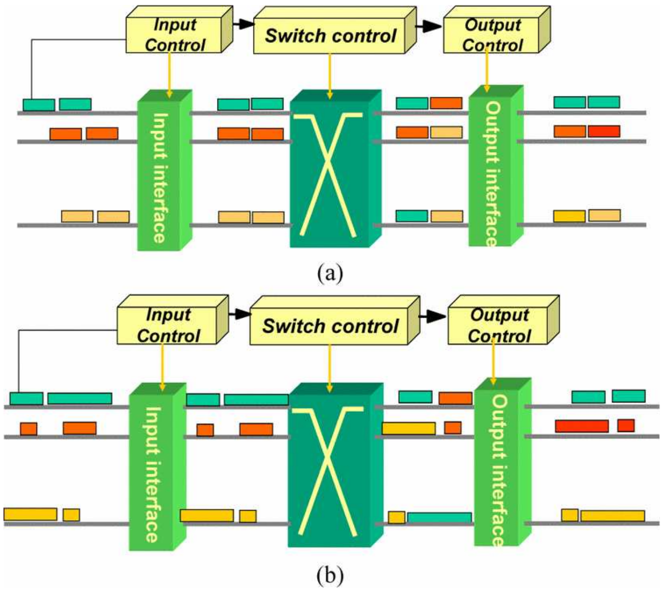

Figure 1.6: Optical router structures for (a) synchronous and fixed-length packet forwarding, and (b) asynchronous and variable-length packet forwarding. [62]

the network utilization efficiency [61].

In optical packet switching, since the optical packets are much shorter than the optical bursts, the systems require rapid switching, typically in a nanosecond time scale [61]. Hence, with the lack of optical buffering, slow switching can cause loss of bits in a packet during the switching transition, unless there is enough time gap or "*guard time*" between the packets to account for the switching transition. This guard time must be short for the optical packet switched network to be efficient, which in turn requires fast switching operation for the optical routers. Fig. 1.7 depicts an implementation of optical routers with novel hierarchical contention resolution and arbitration in wavelength-time-space domains [61, 62]. The router includes feedback fiber delay lines as "optical buffers", arrayed waveguide grating router (AWGR) with fast tunable-wavelength converters at the input, and fixed-wavelength converters at the output of the switching fabric. The tunable wavelength converter therein consists of the key component - the fast-switching tunable laser such as a superstructure grating distributed Bragg reflector (SSG-DBR) or sampled grating distributed Bragg reflector (SG-DBR) lasers to meet the requirement of reducing the guard time of the optical packets (on a time scale in the other of nano-seconds).

1.3.2 Examples of optical packet switching projects

A variety of reconfigurable optical networking technologies and architectures have been developed and examined over the past few years. Erbium doped fiber

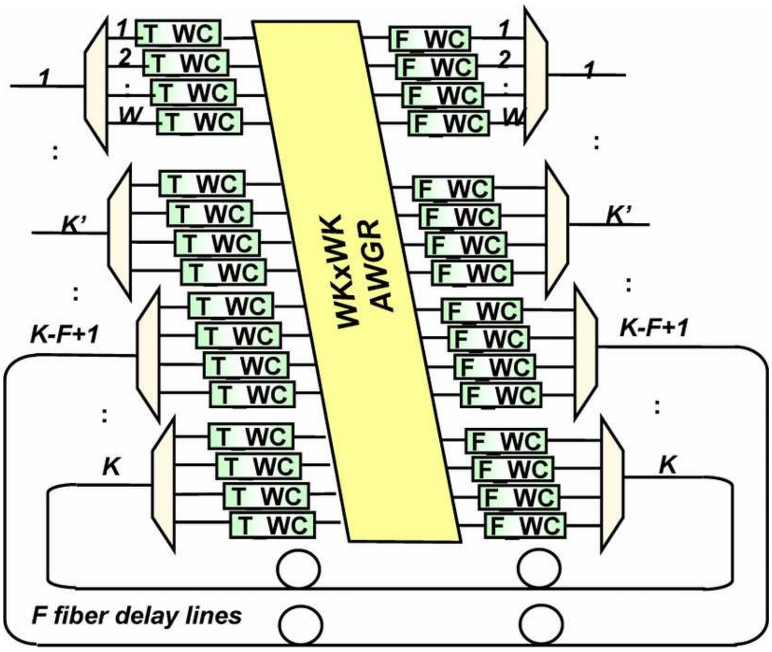

Figure 1.7: An implementation of an optical router supporting wavelength-time-space domain contention resolution. [61, 62]

amplifiers (EDFAs), reconfigurable optical add/drop multiplexers (ROADMs), wavelength crossconnects (WXCs), and tunable lasers are the key components to enable these optical networks [63]. As discussed above, among diverse optical switching techniques, such as Generalized Multiprotocol Label Switching (GM-PLS), Waveband Switching (WBS), Photonic Slot Routing (PSR), Optical Flow Switching (OFS), Optical Burst Switching (OBS), and Optical Packet Switching (OPS), optical packet switching technology is particularly attractive for a true IP-over-WDM architecture, where the IP packets are switched and routed over the all-optical WDM network without excessive electronic processing in the data plane. In the following, we review recent testbed activities on OPS proposed for Metropolitan Area Network (MAN).

- HORNET Project (2003): The Hybrid Optoelectronic Ring Network HORNET [64], proposed by the research group in Stanford University, is a packet-over-WDM ring network which employed fast-tunable packet transmitters and wavelength routing. The sampled grating DBR laser and grating-assisted coupler with sampled reflector laser (GCSR) was the key component for the tunable transmitter, with tuning times ranging between 5-20 ns. The receiver in each node was fixed to its home wavelength channel which could be shared by other nodes.

- RingO Project (2004): The RingO project [65, 66] demonstrated a unidirectional synchronous WDM ring network. Each fixed-size packet was carried by equally sized time slots. The RingO node consists of a fixed-receiver, which corresponds to its home channel, and an array of fixed-tuned transmitters, one for each home channel. The fast-tunable transmitters are made by an array laser. The channel monitoring can be carried out by simply measuring the power level of each slot and wavelength (without any required label/header processor). The MAC and Physical layer operation is simpler than HORNET and was presented in [65]. RingO was successfully demonstrated with 2 nodes and 4 channels (each channel with a data rate at 2.5 Gbit/s).

- HOPSMAN Network (2006): The High-Performance Optical Packet-Switched WDM ring MAN network - HOPSMAN [67, 68] was proposed by the universities of Taiwan. HOPSMAN is a unidirectional WDM slotted-ring network with multiple WDM data channels (at 10 Gb/s) and one control channel (at 2.5 Gb/s). Each node in the HOPSMAN network has a fixed transmitter and receiver pair for accessing the control channel, and a tunable transmitter and receiver pair for accessing data channels. The ring testbed of HOPSMAN was 38.3 km long, with 10 cycles per ring, 50 slots per cycle, and each slot 320 ns long. The control channel wavelength was set at 1540.56 nm with 2.5 Gbit/s Bitrate, and four data channels at wave- lengths of 1551.72 nm, 1553.33 nm, 1554.94 nm, and 1556.55 nm.

- Scalable Optical Packet switches (2009): This project [69, 70, 71] was proposed by the COBRA Research Institute. They demonstrated an OPS subsystem employing in-band labeling to allow for transparent routing of multi-wave-length packets with multiple data formats and at different data bitrates. The address information of optical packets is encoded in-band with the payload. Experimental results [71] show error-free operation of 1 $\times$ 64 optical packet switch subsystems for 160 Gb/s RZ-OOK, 320 Gb/s NRZ-OOK, 120 (12 $\times$ 10) Gb/s DPSK and 480 (12 $\times$ 40) Gb/s OFDM multi-wavelength with 64-QAM packets.

- Optical label based OPS (2009): The authors demonstrated OPS and buffering operation of a DWDM/NRZ-DPSK optical packet [72, 73]. The data rate of the payload was 640Gbit/s (64$\times$10 Gbit/s) with error-free operation, including 200-Gchip/s PSK optical label processing for all 64-wavelength-channel DPSK packets (label and payload are phase-modulated).

1.4 Advanced modulation formats for re-configurable optical networks

The extensive research works into re-configurable optical networks, (especially with optical packet switching technology) carried out recently, are still implementing low spectral efficiency optical modulation formats such as OOK or Differential BPSK for data transmission. To achieve even higher total capacity (throughput) for the entire network, advanced modulation formats with high spectral efficiency would be applied for the tunable transceivers within the optical routers. Combining advanced optical modulation formats employing coherent transmission techniques with optical packet/burst switching can enable optical networks that are highly efficient both temporally and spectrally. Optical packet switching that employs fully coherent detection PM-QPSK [74, 75], self-homodyne detection DQPSK [76, 77], or 16-QAM polarization multiplexed pilot with self-homodyne coherent detection [78] have been recently reported.

In such a system, the requirement for a fast wavelength-switching tunable laser is inevitable. The monolithic tunable semiconductor lasers utilizing the index-tuning mechanism, such as SG-DBR or SSG-DBR lasers, are considered as the main potential candidates for these optical packet switching systems. However, as mentioned in previous sections, in optical transmission deploying advanced modulation formats, the phase noise of semiconductor lasers in the transceivers is a crucial characteristics that defines the ultimate performance of the systems. Even though the SG-DBR laser has demonstrated a very fast tuning speed of less than 5 ns [79], which is most suitable for optical packet switching, the SG-DBR device has shown complicated phase noise characteristics that impacts its feasibility for higher order modulation formats [32, 80]. The performance degradation caused by the wavelength switching event of the SG-DBR laser also requires investigation to improve the total throughput of the networks when the optical packet becomes shorter. In the next chapters, we investigate in detail the phase noise characteristics of the SG-DBR laser and its effect on systems employing advanced modulation formats. The system performance under both static and dynamic (during wavelength switching of the SG-DBR laser) conditions for optical packet switching networks will also be evaluated.

1.5 Summary

In this chapter, we have reviewed the current status of the optical communications networks, particularly on the optical modulation formats and reconfigurable optical networks aspects. We firstly reviewed the fundamental non-linear Shannon limit of optical communications over the fiber channel. A general formula of the channel capacity limit has been re-derived and discussed. We then had an overview from literature on advanced optical modulation formats in terms of spectral efficiency and energy efficiency. The future trend in spatial division multiplexing for optical communications was also discussed.

At the same time, to further increase the total throughput of the entire optical networks, fast reconfigurable optical networks with optical packet/burst switching would be employed for reducing the latency of the networks. Thus we reviewed the evolution of switching technology in optical communications networks as well as some exemplary testbeds for the optical packet switching networks. Subsequently, the possibility of combining advanced modulation formats and reconfigurable optical networks making use of fast tuning optical transceivers has been proposed.

The discussion on the SG-DBR laser, the key component in the fast tuning optical transceivers, has been briefly presented for the application in the proposed scenario. Especially, the phase noise property of the SG-DBR lasers is quite sophisticated and deviates from the conventional semiconductor lasers with a single active section as mentioned above. Consequently, the next chapter will be dedicated to review the theory on phase noise of conventional semiconductor lasers. Based on that theory, we will develop the theoretical model for the complete phase noise processes exhibited in the multi-section monolithic tunable lasers, particularly the SG-DBR laser with passive grating sections.

Bibliography

[1] C.E. Shannon, "A mathematical theory of communication," Bell Syst. Tech. J., vol 27, pp. 379-423 and 623-656, 1948.

[2] P.P. Mitra, J.B. Stark, "Nonlinear limits to the information capacity of optical fibre communications," Nature, vol. 411, pp. 1027-1030, 2001.

[3] R.-J. Essiambre, G.Kramer, P.J. Winzer, G.J. Foschini, B. Goebel, "Capacity Limits of Optical Fiber Networks," IEEE/OSA Journal of Lightwave Technology, vol. 28, pp. 662 - 701, 2010.

[4] R.J. Essiambre, R.W. Tkach, "Capacity Trends and Limits of Optical Communication Networks," Proceeding of the IEEE, vol. 100, pp. 1035 - 1055, 2012.

[5] J.M. Kahn, K.P. Ho, "Spectral efficiency limits and modulation/detection techniques for DWDM systems," IEEE Journal of Selected Topics in Quantum Electronics, vol. 10, pp. 259 - 272, 2004.

[6] Peter J. Winzer, "High-Spectral-Efficiency Optical Modulation Formats," IEEE/OSA Journal of Lightwave Technology, vol. 30, pp. 3824 - 3835, 2012.

[7] M. Nakazawa, K. Kikuchi, and T. Miyazaki, High spectral density optical communication technologies . Berlin: Springer-Verlag, 2010

[8] P.J. Winzer and R.J. Essiambre, "Advanced Modulation Formats for High-Capacity Optical Transport Networks", J. Lightw. Technol., vol. 24, pp. 4711–4728, 2006.

[9] M. Birk et al., "Field Trial of End-to-End OC-768 Transmission Using 9 WDM Channels over 1000 km of Installed Fiber", OFC 2003, paper TuS4.

[10] J.H. Sinsky et al., "A 107-Gbit/s Optoelectronic Receiver Utilizing Hybrid Integration of a Photodetector and Electronic Demultiplexer", J. Lightw. Technol., vol. 26, pp. 114–120, 2008.

[11] R.A. Griffin and A.C. Carter, “Optical differential quadrature phase-shift key (oDQPSK) for high capacity optical transmission,” OFC-2002, paper WX6.

[12] M. Daikoku et al., “100 Gbit/s DQPSK transmission experiment without OTDM for 100G ethernet transport”, OFC 2006, paper PDP36.

[13] P. J. Winzer et al., ”100-Gb/s DQPSK Transmission: From Laboratory Experiments to Field Trials”, J. Lightw. Technol., vol. 26, pp. 3388–3402, 2008.

[14] G. Charlet et al., “Transmission of 16.4 Tb/s capacity over 2550 km using PDM-QPSK modulation format and coherent receiver”, OFC-2008, paper PDP3.

[15] A. H. Gnauck et al.,”Spectrally Efficient Long-Haul WDM Transmission Using 224-Gb/s Polarization-Multiplexed 16-QAM”, J. Lightw. Technol., vol. 29, pp. 373–377, 2011.

[16] M. Yoshida, H. Goto, K. Kasai, and M. Nakazawa, “64 and 128 coherent QAM optical transmission over 150 km using frequency-stabilized laser and heterodyne PLL detection”, Optics Express, vol. 16, pp. 829-840, 2008.

[17] S. Okamoto, K. Toyoda, T. Omiya, K. Kasai, M. Yoshida, M. Nakazawa, “512 QAM (54 Gbit/s) coherent optical transmission over 150 km with an optical bandwidth of 4.1 GHz”, ECOC 2010, paper PD2.3.

[18] M. Nakazawa, T. Hirooka, M. Yoshida, K. Kasai, “Ultrafast Coherent Optical Transmission”, IEEE J. Sel. Topics Quantum Electron., vol. 18, pp. 363–376, 2011.

[19] S. Chandrasekhar and X. Liu, “OFDM Based Superchannel Transmission Technology,” IEEE/OSA Journal of Lightwave Technology, vol. 30, no. 24, pp. 3816 - 3823, 2012.

[20] S. Chandrasekhar and X. Liu "Experimental investigation on the performance of closely spaced multi-carrier PDM-QPSK with digital coherent detection", Optics Express, vol. 17, pp.12350 -12361, 2009.

[21] Xiang Zhou et. al, “PDM-Nyquist-32QAM for 450-Gb/s Per-Channel WDM Transmission on the 50 GHz ITU-T Grid,” IEEE/OSA Journal of Lightwave Technology, vol. 30, no. 4, pp. 553 - 559, 2012.

[22] Jin-Xing Cai et. al, “20 Tbit/s Transmission Over 6860 km With Sub-Nyquist Channel Spacing,” IEEE/OSA Journal of Lightwave Technology, vol. 30, no. 4, pp. 651-657 , 2012.

[23] W. Shieh, C. Athaudage, “Coherent optical orthogonal frequency division multiplexing,” Electron. Lett., vol. 42, pp. 587-589, 2006.

[24] J. Amrstrong, ”OFDM for Optical Communications”, J. Lightw. Technol., vol. 27, pp. 189–204, 2009.

[25] W. Shieh, Q. Yang, Y. Ma, “107 Gb/s coherent optical OFDM transmission over 1000 km SSMF fiber using orthogonal band multiplexing,” Optics Express, vol. 16, pp. 6378-6386, 2008.

[26] X. Liu, S. Chandrasekhar, B. Zhu ; P.J. Winzer, “Transmission of a 448-Gb/s reduced-guard-interval CO-OFDM signal with a 60-GHz optical bandwidth over 2000 km of ULAF and five 80-GHz-Grid ROADMs”, OFC 2010, paper PDPC2.

[27] Qi Yang et. al, "Coherent optical DFT-Spread OFDM transmission using orthogonal band multiplexing", Optics Express, vol. 20, no. 3, pp.2379 - 2385, 2012.

[28] D. Hillerkuss et. al, “26 Tbit s^{-1} line-rate super-channel transmission utilizing all-optical fast Fourier transform processing,” Nature Photonics, vol. 5, pp. 364–371, 2011.

[29] F. A. Kish et. al, "Currentstatus of large-scale InP photonic integrated circuits", J. Sel. Topics Quantum Electron., vol. 17, no. 6, pp.1470 -1488, 2011.

[30] http://www.fujitsu.com/emea/services/microelectronics/dataconverters/chais.

[31] S. J. Savory, "Digital filters for coherent optical receivers", Optics Express, vol. 16, no. 2, pp.804 -817, 2008.

[32] Tam N. Huynh, L. Nguyen, and L.P. Barry “Phase Noise Characterization of SGDBR Lasers Using Phase Modulation Detection Method With Delayed Self-Heterodyne Measurements,” IEEE/OSA Journal of Lightwave Technology, vol. 31, no. 8, pp. 1300-1308, 2013.

[33] M. G. Taylor, "Phase estimation methods foroptical coherent detection using digital signal processing", J. Lightw. Technol., vol. 27, no. 7, pp.901-914, 2009.

[34] W. Shieh and K.-P. Ho, "Equalization-enhanced phase noise for coherent-detection systems using electronic digital signal processing", Opt. Exp., vol. 16, no. 20, pp.15718-15727, 2008.

[35] E. Ip and J. M. Kahn, "Fiber impairment compensation using coherent detection and digital signal processing", J. Lightw. Technol., vol. 28, no. 4, pp. 502 -519, 2010.

[36] Xiang Liu, A. R. Chraplyvy, P. J. Winzer, R. W. Tkach, S. Chandrasekhar, “Phase-conjugated twin waves for communication beyond the Kerr nonlinearity limit,” Nature Photonics, vol. 7, pp. 560–568, 2013.

[37] G. Raybon et. al, “All-ETDM 80-Gbaud (640-Gb/s) PDM 16-QAM Generation and Coherent Detection,” IEEE Photon. Technol. Lett., vol. 24, no. 15, pp. 1328-1330, 2012.

[38] D. Qian et. al, “High Capacity/Spectral Efficiency 101.7-Tb/s WDM Transmission Using PDM-128QAM-OFDM Over 165-km SSMF Within C- and L-Bands,” J. Lightw. Technol., vol. 30, no. 10, pp. 1540-1548, 2012.

[39] P. J. Winzer, “Energy-efficient optical transport capacity scaling through spatial multiplexing,” IEEE Photon. Technol. Lett., vol. 23, no. 13, pp. 851–853, 2011.

[40] Peter J. Winzer, “Optical Networking Beyond WDM,” IEEE Photonics Journal, Vol. 4, No. 2, pp. 647-651, 2012.

[41] T. Morioka, Y. Awaji, R. Ryf, P. Winzer, D. Richardson, and F. Poletti, “Enhancing optical communications with brand new fibers,” IEEE Commun. Mag., vol. 50, no. 2, pp. s31–s42, 2012.

[42] D. J. Richardson, J. M. Fini, L. E. Nelson, “Space-division multiplexing in optical fibres,” Nature Photonics, vol. 7, pp. 354–362, 2013.

[43] B. Zhu et. al, “112-Tb/s Space-division multiplexed DWDM transmission with 14-b/s/Hz aggregate spectral efficiency over a 76.8-km seven-core fiber,” Optics Express, vol. 19, no. 17, pp. 16 665–16 671, 2011.

[44] S. Chandrasekhar et. al, “WDM/SDM transmission of 10×128-Gb/s PDM-QPSK over 2688-km 7-core fiber with a per-fiber net aggregate spectral-efficiency distance product of 40,320 km.b/s/Hz,” ECOC 2011, Paper Th.13.C.4.

[45] H. Takara et. al, “1.01-Pb/s (12 SDM/222 WDM/456 Gb/s) Crosstalk-managed Transmission with 91.4-b/s/Hz Aggregate Spectral Efficiency,” ECEOC.2012, paper Th.3.C.1.

[46] J. Sakaguchi et. al, "19-core fiber transmission of 19 × 100 × 172-Gb/s SDM-WDM PDM-QPSK signals at 305Tb/s," OFC 2012, paper PDP5C.1.

[47] Y. Awaji et. al, "World first mode/spatial division multiplexing in multi-core fiber using Laguerre-Gaussian mode," ECOC 2011, paper We.10.P1.55.

[48] J. Wang et. al, "Terabit free-space data transmission employing orbital angular momentum multiplexing," Nature Photonics, vol. 6, pp. 488–496, 2012.

[49] Keang-Po Ho and J.M. Kahn, "Statistics of Group Delays in Multimode Fiber With Strong Mode Coupling," IEEE/OSA Journal of Lightwave Technology, vol. 29 , no. 21, pp. 3119 - 3128, 2011.

[50] Keang-Po Ho and J.M. Kahn, "Mode-dependent loss and gain: statistics and effect on mode-division multiplexing," Optics Express, Vol. 19, no. 17, pp. 16612-16635, 2011.

[51] R. Ryf et. al, "Mode-Division Multiplexing Over 96 km of Few-Mode Fiber Using Coherent 6×6 MIMO Processing," IEEE/OSA Journal of Lightwave Technology, vol. 30 , no. 4, pp. 521 - 531, 2012.

[52] R. Ryf et. al, "Space-division multiplexed transmission over 4200 km 3-core microstructured fiber," OFC 2012, Paper PDP5C.2.

[53] M. Karlsson and E. Agrell , "Which is the most power-efficient modulation format in optical links?," OSA Optics Express, vol. 17, pp. 10814-10819, 2009.

[54] E. Agrell and M. Karlsson, "Power-Efficient Modulation Formats in Coherent Transmission Systems," Journal of Lightwave Technology, vol. 27, pp. 5115 - 5126, 2009.

[55] D. Millar, et al., "Generation and long-haul transmission of polarization switched QPSK at 42.9 Gb/s," OSA Optics Express, vol. 19, pp. 9296–9302, 2011.

[56] L. Nelson, X. Zhou, N. Suibhne, A. Ellis, and P. Magill, "Experimental comparison of coherent polarization-switched QPSK to polarization multiplexed QPSK for 10×100 km WDM transmission," Optics Express, vol. 19, pp. 10849–10856, May 2011.

[57] B. Krongold, T. Pfau, N. Kaneda, and S. Lee, "Comparison Between PS-QPSK and PDM-QPSK With Equal Rate and Bandwidth," IEEE Photonics Technology Letters, vol. 24, pp. 203–205, 2012.

[58] Xiang Liu, Thomas H. Wood, Robert W. Tkach, and S. Chandrasekhar, "Demonstration of Record Sensitivities in Optically Preamplified Receivers by Combining PDM-QPSK and M-Ary Pulse-Position Modulation," Journal of Lightwave Technology, vol. 30, pp. 406 - 413, 2012.

[59] R.C. Alferness, "The Evolution of Configurable Wavelength Multiplexed Optical Networks—A Historical Perspective," Proceeding of the IEEE, vol. 100, pp. 1023 - 1034, 2012.

[60] A.A.M. Saleh, J.M. Simmons, "All-Optical Networking—Evolution, Benefits, Challenges, and Future Vision," Proceeding of the IEEE, vol. 100, pp. 1105 - 1117, 2012.

[61] S. J. Ben Yoo, "Optical Packet and Burst Switching Technologies for the Future Photonic Internet," IEEE/OSA Journal of Lightwave Technology, vol. 24 , no. 12, pp. 4468 - 4492, 2006.

[62] S. J. Ben Yoo, "Energy Efficiency in the Future Internet: The Role of Optical Packet Switching and Optical-Label Switching," IEEE Journal of Selected Topics in Quantum Electronics, vol. 17, no. 2, pp. 406 - 418, 2011.

[63] M. Maier et. al, "A Global Overview of Optical Switching Network Testbed Activities," J. Lightw. Technol., vol. 27, pp. 4377 - 4384, 2009.

[64] I.M. White et. al, "A summary of the HORNET project: a next-generation metropolitan area network," IEEE Journal on Selected Areas in Communications, vol. 21, pp. 1478 - 1494, 2003.

[65] A. Carena et. al, "RingO: an experimental WDM optical packet network for metro applications," IEEE Journal on Selected Areas in Communications, vol. 22, pp. 1561 - 1571, 2004.

[66] R. Gaudino et. al, "RINGO: a WDM ring optical packet network demonstrator," ECOC 2001 - 27th European Conference on Optical Communication, vol. 4, pp. 620 - 621, 2001.

[67] M. Yuang et. al, "HOPSMAN: An Experimental Testbed System for a 10-Gb/s Optical Packet-Switched WDM Metro Ring Network," IEEE Communications Magazine, vol. 46, pp. 158 - 166, 2008.

[68] M.C. Yuang et. al, "HOPSMAN: An Experimental Optical Packet-Switched Metro WDM Ring Network With High-Performance Medium Access Control," IEEE/OSA Journal of Optical Communications and Networking, vol. 2, pp. 91 - 101, 2010.

[69] N. Calabretta et. al, "Scalable optical packet switch for optical packets with multiple modulation formats and data rates," 35th European Conference on Optical Communication, pp. 1 - 2, 2009.

[70] N. Calabretta et. al, "Scalable Optical Packet Switches for Multiple Data Formats and Data Rates Packets," IEEE Photon. Technol. Lett., vol. 22, pp. 483 - 485, 2010.

[71] N. Calabretta et. al, "Scalable and agnostic optical packet switch sub-system for optical packets with multiple modulation formats and data rates," 12th International Conference on Transparent Optical Networks (ICTON), pp. 1-4, 2010.

[72] H. Furukawa et. al, "640 Gbit/s (64-wavelength × 10 Gbit/s) data-rate wide-colored NRZ-DPSK optical packet switching and buffering demonstration," J. Lightw. Technol., vol. 28, pp 336-343, 2010.

[73] N. Wada et. al, " Prototype 160-Gbit/s/port optical packet switch based on optical code label processing and related technologies," IEEE J. Sel. Topics Quantum Electron., vol. 13, pp 1551-1559, 2007.

[74] J. E. Simsarian et. al, "Fast-Tuning 224-Gb/s Intradyne Receiver for Optical Packet Networks," OFC 2010, paper PDPB5.

[75] J. E. Simsarian et. al, "Optical Packet Switches," ECOC 2011, paper Mo.2.A.1.

[76] S. Shinada, H. Furukawa, N. Wada, "Huge capacity optical packet switching and buffering," Optics Express, vol. 19(26), B406–B414 (2011).

[77] T.N. Huynh, K. Shi, F. Smyth, L.P. Barry, "DQPSK optical packet switching using an SGDBR laser," in CLEO Europe 2011, paper CI1.

[78] S. Shinada, M. Nakamura, Y. Kamio, N. Wada, "16-QAM optical packet switching and the real-time self-homodyne detection using polarization-multiplexed pilot-carrier," Optics Express, vol. 20, pp. B535–B542, 2012.

[79] J.E. Simsarian et. al, "Less than 5-ns wavelength switching with an SGDBR laser," IEEE Photon. Technol. Lett., vol. 18, pp. 565–567, 2006.

[80] Tam N. Huynh, Frank Smyth, Lim Nguyen, Liam P. Barry, "Effects of phase noise of monolithic tunable laser on coherent communication systems," OSA Optics Express, vol. 20, no. 26, pp. B244-B249, 2012.

Chapter 2

Phase Noise in Semiconductor Lasers

Optical communications would not be practical without the invention of semiconductor lasers in the early 1960s. From a communications systems perspective, one of the most important property of continuous wave semiconductor lasers is the laser phase noise or the spectral purity of the output light. Moreover, as reviewed in the previous chapter, optical communications is currently moving towards leveraging coherent detection technique to replace the conventional intensity modulation/direct detection systems in longhaul and metro networks. Coherent optical communications employing advanced modulation formats utilizes both phase and amplitude of the optical field to transmit the data. That in turn poses a more stringent requirement on the spectral purity of the semiconductor lasers used for these systems. It's obvious that the laser phase noise is setting the lower bound for the bit error rate of any systems using the optical phase to carry the information data. Consequently, a full understanding of the phase noise processes in semiconductor lasers is indispensable for this work.

In this chapter, we firstly review the conventional theory on phase noise of semiconductor lasers which was developed in the 1980s. Section 2.1 will briefly review the Schawlow-Townes-Henry theory of semiconductor lasers that includes the gain-phase coupling associated with the semiconductor amplifying medium and the associated carrier density relaxation oscillation. From that we then continue the investigation of phase noise in multi-section monolithic tunable lasers which is the main concern in this work. An analytical model describing the complete instantaneous frequency noise spectrum of a four-section Sampled-Grating distributed Bragg reflector laser with more additional phase noise processes due to the fluctuating carrier densities in the passive tuning sections is derived in section 2.2. Finally, section 2.3 will conclude the chapter.

2.1 Fundamental theory of phase noise in semiconductor lasers

The laser is essentially a special *optical oscillator*, i.e. it has many behaviors of a typical oscillator [1]. In this work, we are solely interested in operation of semiconductor lasers above threshold, where the amplitude of the optical field is nearly constant while the phase can take any value. The optical phase in a semiconductor laser exhibits a relatively slow wandering which could be basically described by a Brownian random process [2, 3, 4]. In this section, we will review the theory of laser phase noise in conventional single mode - single section semiconductor laser that would include: the quantum noise limit with the Henry linewidth enhance factor α, the relaxation oscillation and the low frequency flicker noise.

2.1.1 Schawlow-Townes-Henry model of phase noise in semiconductor lasers

The phase noise in an oscillator will obviously broaden its spectral line-shape in the frequency domain. Therefore the spectral purity becomes an interesting property of semiconductor lasers. There have been extensive investigations of this area from the early stage of laser physics up to date. The full-width-at-half-maximum (FWHM) spectral linewidth ($\Delta\nu$) is the important parameter which is usually used for evaluating the phase noise property of lasers. In the pioneering paper proposing the optical maser (or early laser) [1], Schawlow and Townes derived a formula for the laser linewidth which is inversely proportional to the output power (P_0) and valid for operating below threshold. Lax then pointed out that above threshold, the amplitude fluctuations of the laser are stabilized and this is accompanied by a factor of 2 times reduction in the $\Delta\nu P_0$ product [4]. Later in the seminal paper on theory of the linewidth of semiconductor lasers [2], Henry showed that semiconductor lasers exhibit an additional broadening factor of $(1 + \alpha^2)$ to the original quantum noise linewidth from Schawlow-Townes-Lax formula (where $\alpha = \frac{\Delta n'}{\Delta n''}$ [2]).

In semiconductor lasers, the discrete spontaneous emission events alter the phase and the amplitude of the output optical field. This leads to the fluctuation in the phase of the optical field, and subsequently defines the width of the optical spectrum. Beside the abrupt phase change of the optical field after a spontaneous emission event, the intensity change during this event results in an even larger *delayed phase change*. This change is brought about by a gain change associ-

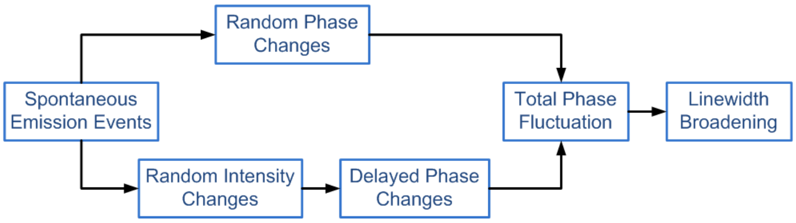

Figure 2.1: The generation of phase noise in conventional semiconductor lasers

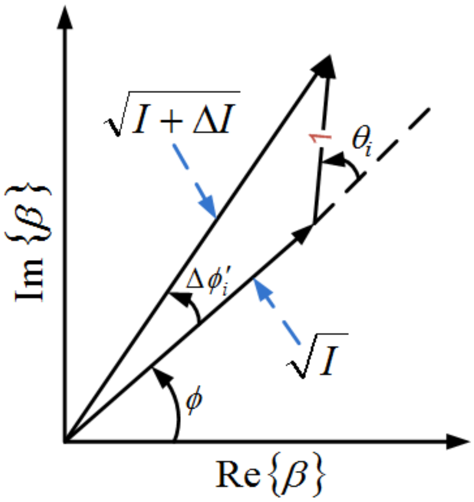

Figure 2.2: The instantaneous changes of phase and intensity of the optical field caused by a spontaneous emission event [2]

ated with the relaxation oscillation that follows the spontaneous emission event and restores the laser intensity back to the steady stage [3]. These phase noise generation processes are summarized in Fig. 2.1.

To briefly review the derivation for the phase noise in semiconductor lasers, we follow the notation of Henry in [2, 3, 4]. The laser optical field can be expressed in a complex amplitude notation as:

$$E_{laser}(t) = Re\left\{\sqrt{I(t)}e^{i(\omega_0 t+\phi(t))}\right\} = Re\left\{\beta e^{i\omega_0 t}\right\} \tag{2.1}$$

where $\beta = \sqrt{I(t)}e^{i\phi(t)}$ is the slowly varying field, I(t) is the intensity and $\phi(t)$ is the optical phase. We now relate the output optical spectrum $G(\omega)$ with the laser phase to derive the formula of phase noise induced laser linewidth. The power spectral density (PSD) of the optical field is the Fourier transform of the auto-correlation of the complex field [3]:

$$G(\omega) = \int \langle E_{laser}(t)E_{laser}(0)\rangle\, e^{i\omega t}dt \tag{2.2}$$

In this subsection, we assume that the intensity fluctuation after a spontaneous emission event is stabilized, i.e. the observation time is large enough for the relaxation oscillations to have died away. In this case we arrive at [3]:

$$G(\omega) = \int e^{i\omega_0 t} \left\langle e^{i\Delta\phi(t)} \right\rangle e^{i\omega t} dt = \int e^{i\omega_0 t} e^{(-\frac{1}{2}\left\langle \Delta\phi^2(t) \right\rangle)} e^{i\omega t} dt \tag{2.3}$$

where $\Delta\phi(t) = \phi(t) - \phi(0)$ is the phase change (or named as phase error in the later chapters) over the interval time t. The simplification has been performed in equation 2.3 based on the justification that the phase noise $\phi(t)$ is undergoing a random walk process (Brownian motion), i.e. $\Delta\phi(t)$ has a Gaussian distribution [2, 3, 4]. We now need to derive the expression for $\langle \Delta\phi^2(t) \rangle$. To do so, we pay attention to the spontaneous emission events and their consequences.

Figure 2.2 illustrates the change in the complex amplitude of the optical field after a spontaneous emission event. With an assumption that a spontaneous emission event causes unit amplitude change in the optical field, the field change $\Delta\beta_i$ can be expressed as:

$$\Delta\beta_i = e^{(i\phi + i\theta_i)} \tag{2.4}$$

and the corresponding instantaneous change in phase and amplitude of the field envelope are:

$$\Delta\phi_i' = \sqrt{I}\sin(\theta_i) \tag{2.5}$$

$$\Delta I_i = 1 + \sqrt{I}\cos(\theta_i) \tag{2.6}$$

With the aid of the coupled rate equations for I and ϕ, we can show that the amplitude change ΔI_i will lead to a subsequent delayed phase change given by [2]:

$$\Delta\phi_i'' = -\frac{\alpha}{2I}(1 + 2\sqrt{I}\cos(\theta_i)) \tag{2.7}$$

Here we introduce the $\alpha = \frac{\Delta Re(n)}{\Delta Im(n)}$ coefficient or Henry linewidth enhancement factor (n: refractive index). The total phase change is the sum of instantaneous phase changes in equation 2.5, and delayed phase change in equation 2.7. After a straightforward derivation as in [2], we can obtain the total phase change (phase error) variance as:

$$\left\langle \Delta\phi^2(t) \right\rangle = \frac{R(1+\alpha^2)t}{2I} \tag{2.8}$$

where R is the spontaneous emission rate. If we note the *coherent time* τ_c as $\frac{1}{\tau_c} = \frac{\left\langle \Delta\phi^2(t) \right\rangle}{2t}$ then the term $e^{(-\frac{1}{2}\left\langle \Delta\phi^2(t) \right\rangle)}$ in equation 2.3 becomes e^{-t/τ_c} which yields a Lorentzian shape of the power spectrum of the electric field (E-field). We can then achieve the FWHM linewidth of the PSD of the optical field as:

$$\Delta\nu = \frac{1}{\pi\tau_c} = \frac{\langle\Delta\phi^2(t)\rangle}{2\pi t} = \frac{R}{4\pi I}(1+\alpha^2) \tag{2.9}$$

The linewidth in equation 2.9 can be rewritten in terms of output optical power P_0 as [2]:

$$\Delta\nu = \frac{v_g^2\, h\nu\, g\, n_{sp}\, \alpha_m}{8\pi P_0}(1+\alpha^2) \tag{2.10}$$

where v_g is the group velocity, g is the gain, n_{sp} is the spontaneous emission factor, α_m is the facet loss, and $h\nu$ is the energy of the laser line.

2.1.2 Relaxation oscillation in semiconductor lasers

In the preceding subsection, in evaluating the linewidth of the E-field PSD we made use of an assumption that the intensity-change-induced phase change occurring after the relaxation oscillations have died away, i.e. we only observe the low frequency components of the intensity fluctuation. In this section, we will pay attention to the delayed phase change due to the high frequency components of the intensity fluctuation, i.e. we will investigate the relaxation oscillation phenomenon that follows right after a spontaneous emission event. To do so, the delayed phase change in equation 2.7 would need to be re-written as a time dependent function as in [5] (ignoring the constant phase shift component):

$$\Delta\phi_i'' = -\frac{\alpha\cos(\theta_i)}{\sqrt{I}}f(t) \tag{2.11}$$

It has been proven in [5] that the new time dependent function $f(t)$ will take the form:

$$f(t) = 1 - e^{-\Gamma t}\frac{\cos(\Omega t-\delta)}{\cos(\delta)} \tag{2.12}$$

where Ω is the angular frequency and Γ is the damping rate of the relaxation oscillations, the coefficient δ is defined as:

$$\cos(\delta) = \frac{\Omega}{\sqrt{\Omega^2+\Gamma^2}} \tag{2.13}$$

Figure 2.3 depicts the function $f(t)$ which reflects the damped relaxation oscillation phenomenon as discussed. Following the derivation in [5], we re-obtain the total phase change variance:

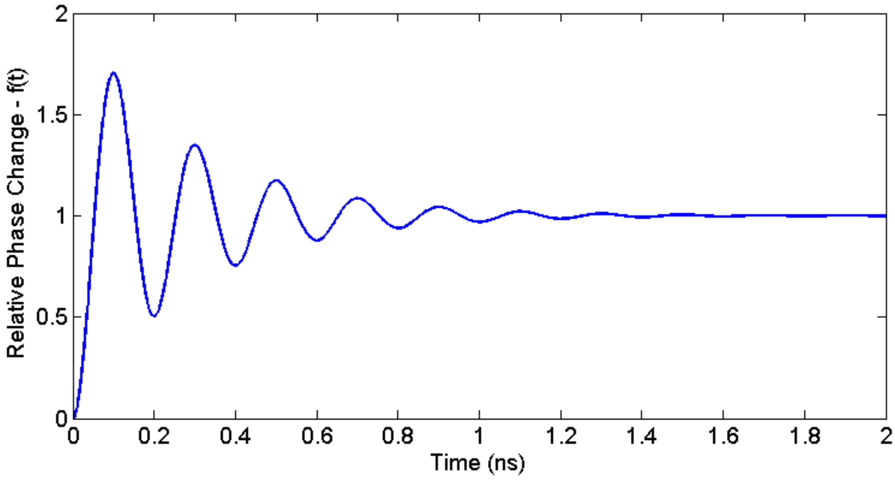

Figure 2.3: Function $f(t)$ accounts for the intensity relaxation oscillation after a spontaneous emission event [5]. $\Gamma = 3.5 \times 10^9 (s^{-1})$, $\Omega = 2\pi \times 5 \times 10^9 (rad/s)$

$$\langle \Delta\phi^2(t) \rangle = \frac{R}{2I} \left\{ (1+\alpha^2)t - \alpha^2 \frac{e^{-\Gamma t}\cos(\Omega t - 3\delta) - cos(3\delta)}{2\Gamma\cos(\delta)} \right\} \tag{2.14}$$

As in equation 2.14, the first term on the right hand side (RHS) is identical to the RHS of the equation 2.8 which yields the Lorentzian spectral shape of the E-field while the second term introduces an oscillation in phase change variance which gives rise to the subsidiary peaks in the power spectrum separated by Ω. Numerical examples of phase change variance and output optical spectrum of a semiconductor laser accounting for Schawlow-Townes-Henry (STH) phase noise with relaxation oscillations have been illustrated in Fig. 2.4

Another widely-used measure to evaluate the phase noise property of an oscillator is the power spectral density of the instantaneous frequency deviation or *FM-noise* (Frequency Modulation noise). The relationship of $S_f(f)$ with phase change variance derived above is given as [6, 7]:

$$\langle \Delta\phi^2(t) \rangle = 4 \int_0^\infty S_f(f) \frac{\sin^2(\pi f t)}{f^2} df \tag{2.15}$$

From [6] the FM-noise spectrum of semiconductor lasers accounting for STH phase noise with relaxation oscillations will take the form as in equation 2.16, where f_r is the relaxation oscillation frequency and Γ is the damping factor mentioned above. A calculated FM-noise spectrum of the phase noise associated with Fig. 2.4 is shown in Fig. 2.5.

$$S_f(f) = \frac{\nu_{STH}}{\pi} \left[1 + \frac{\alpha^2 f_r^4}{(f_r^2 - f^2)^2 + (\Gamma f / 2\pi)^2} \right] \tag{2.16}$$

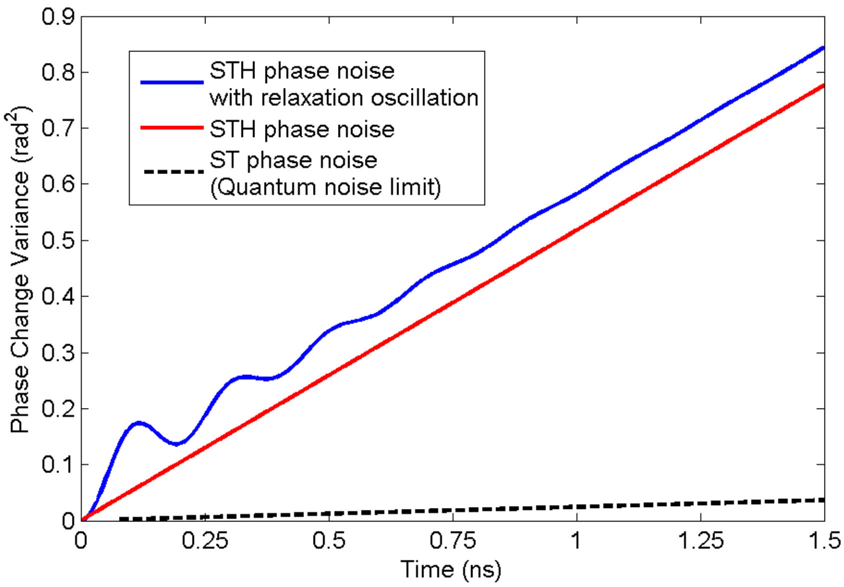

(a) Phase Change Variance

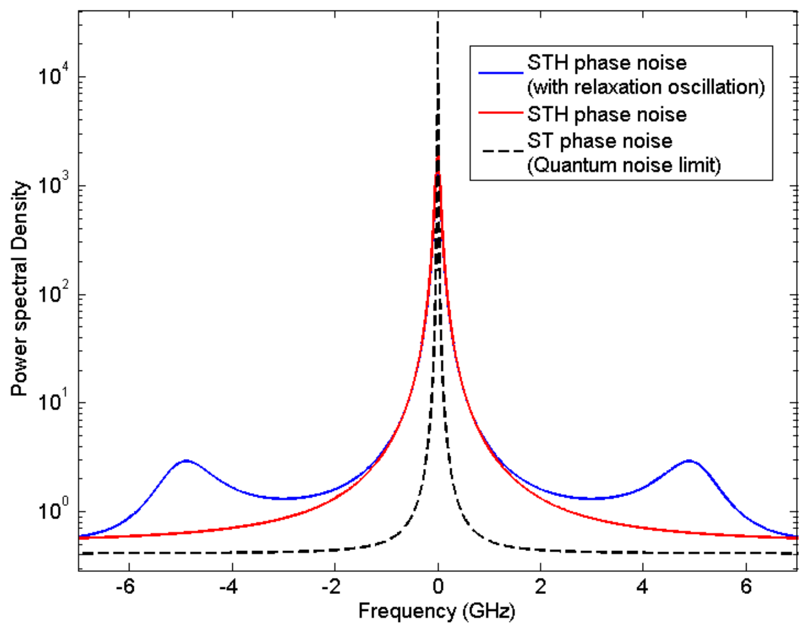

(b) Optical Power Spectral Density

Figure 2.4: Semiconductor laser phase noise accounting for Schawlow-Townes-Henry linewidth with relaxation oscillation. $\Gamma = 3.5 \times 10^9 (s^{-1})$, $\Omega = 2\pi \times 5 \times 10^9 (rad/s)$, $I = 3.1 \times 10^4$, $\alpha = 4.5$, $R = 1.51 \times 10^{12} (s^{-1})$

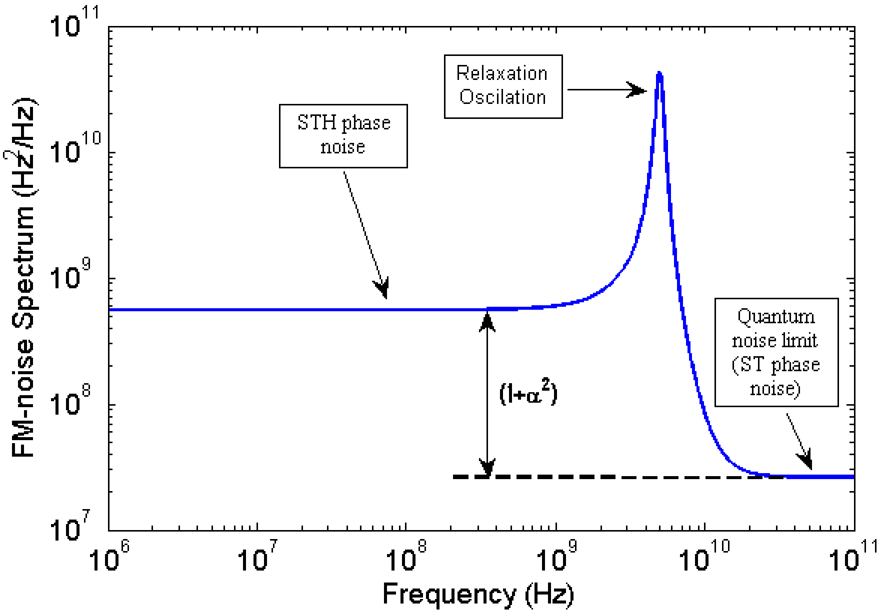

Figure 2.5: FM-noise spectrum of semiconductor laser accounting for STH phase noise with relaxation oscillation.

2.1.3 Flicker noise

Beside the STH phase noise, as an oscillator, the semiconductor lasers also suffer from the ubiquitous flicker noise (or $1/f$ noise). The $1/f$ noise originates from the environmental factors that alter the underlying lasing frequency. This low frequency noise noticeably enhances the total laser phase noise that in turn increases the total phase change variance as well as broadening the PSD of the optical field [7, 8, 9]. In contrast with the STH phase noise derived in equation 2.10, the $1/f$ noise is power independent (because it does not arise from the coherent addition of the spontaneous emission to the laser field) and results in a residual linewidth even at very high output optical power [8]. The FM-noise spectrum in equation 2.16 could be modified to account for the low frequency flicker noise as [7]:

$$S_f(f) = \frac{K_1}{f} + \frac{\nu_{STH}}{\pi}\left[1 + \frac{\alpha^2 f_r^4}{(f_r^2 - f^2)^2 + (\Gamma f/2\pi)^2}\right] \tag{2.17}$$

where the coefficient K_1 defines the level of $1/f$ noise contribution in the total phase noise of the semiconductor laser. A numerical example of the FM-noise spectrum is shown in Fig. 2.6a where the coefficient $K_1 = 2 \times 10^{12}(Hz^2)$ and the STH phase noise were kept similar to Fig. 2.5. The obvious effect of phase change variance enhancement could be confirmed as in Fig. 2.6b where the observation time is sufficiently large.

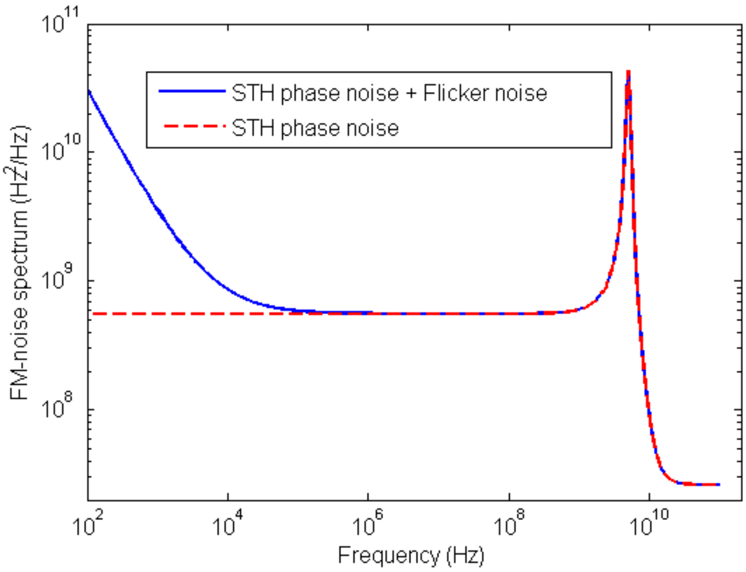

(a) FM-noise spectrum includes: STH phase noise with relaxation oscillation and flicker noise

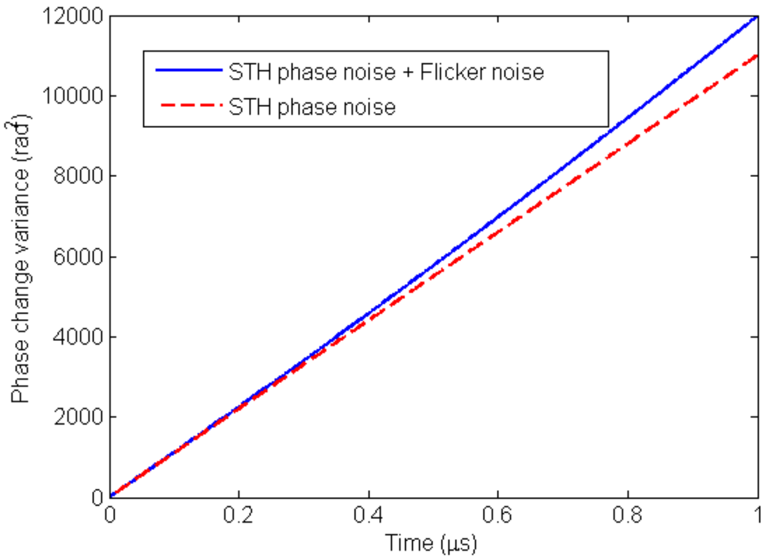

(b) Phase change variance over sufficient observation time

Figure 2.6: The low frequency flicker noise in semiconductor lasers

2.2 Phase noise in multi-section monolithic tunable lasers

In the preceding section, we have reviewed the phase noise processes in a semiconductor laser with one single active section. As mentioned in the previous chapter, the main concern of this work are monolithic multi-sections tunable lasers, especially the DBR-style lasers employing grating tuning mechanisms. These types of lasers consist of passive sections to perform wavelength tuning that subsequently generate additional phase noise components to the phase noise processes presented in section 2.1.

In this section, we describe the entire FM-noise spectrum of monolithic tunable lasers by employing simple analytical models for the dynamic response for each of the phase noise generating mechanisms. Based on an example of experimental FM-noise measurements, we perform a complete analysis of the FM-noise spectrum identifying the following contributions: the traditional Schawlow-Townes-Henry phase noise including the resonance-enhanced FM noise [5]; excess FM noise at low frequencies (also termed $1/f^{\alpha}$ noise); and a filtered FM noise contribution arising from stochastic carrier generation and recombination in the passive tuning sections. The latter is a feature of DBR-style lasers because unlike the carrier density in the gain section, the carrier density in the passive tuning sections is not clamped. The spectral profile of this contribution to the FM-noise spectrum correlates well with the FM-dynamics of the passive sections [9, 10]. We extend the analysis to the 4-section sampled-grating DBR lasers. The performance of coherent systems can be predicted by knowledge of the phase error variance (phase change variance). Accurate and predictable knowledge of the entire FM-noise spectrum would be invaluable for the development of any laser phase noise tracking or suppression techniques for coherent optical systems [7].

We now analyze the FM noise of the Sample-Grating Distributed Bragg Reflector laser. A schematic of the SG-DBR laser is given in the inset of Fig. 2.7 indicating the gain region and the three passive tuning sections. The principle of operation of the SG-DBR laser, and other types of DBR-style tunable lasers, is given in [9]. The SG-DBR laser consists of four separate sections: (1) the Gain section providing optical amplification; coarse wavelength tuning is achieved with two sampled DBR grating sections at the (2) Back section and (3) Front section ; fine wavelength tuning is provided by (4) a short passive Phase waveguide section. The output wavelength can be changed by varying the carrier densities (via the injection current) in each of the tuning sections. The Front and Back sections act as two passive optical mirrors with slightly different power reflection spectra,

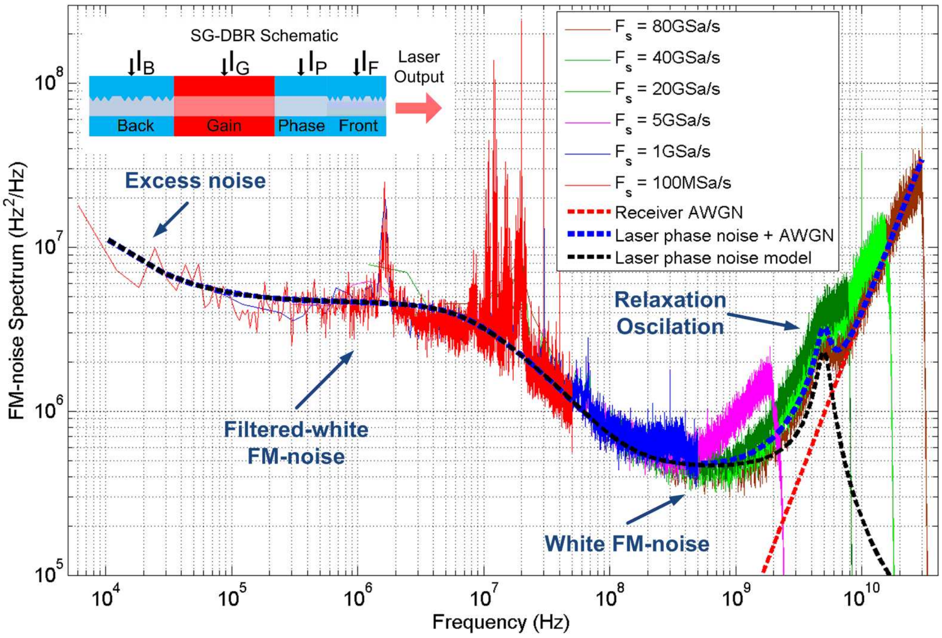

Figure 2.7: Measured FM-noise spectrum of an SG-DBR laser. The pieces from the different sampling rates are shown. The insert is a schematic of the 4-section SG-DBR laser.

exploiting Vernier tuning [9], to select the lasing mode. The fine wavelength tuning function of the selected lasing mode is performed by electrically tuning the short passive Phase section.

We begin by observing the measured FM-noise spectrum of the SG-DBR laser. Here we employ the delayed-self homodyne (DSH) method with a coherent receiver and real-time sampling described in [7]. The phase noise characterization methods will be extensively presented in the next chapter. The sampling rate is adjusted from 100 MSa/s to 80 GSa/s to accurately construct the entire FM-noise spectrum from 6 kHz to 10 GHz. Figure 2.7 shows an example measured FM-noise spectrum of an SG-DBR laser with the various FM noise contributions indicated. It can be seen that the typical STH FM-noise (STH phase noise) can be inferred from 500 MHz out to 10 GHz, with the minimum value of $4.5 \times 10^5 Hz^2/Hz$ corresponding to the laser intrinsic linewidth (full width half-maximum when measuring the spectrum of the laser electric field using the DSH technique, and assuming only white FM-noise) and a relaxation oscillation peak at around 5 GHz. There is additional low frequency noise below 400 MHz including the *filtered FM noise* and the excess FM noise (below 200 kHz). The rising edge towards high frequencies (dash-red curve) is an artifact of the measurement technique due to differentiated additive white Gaussian noise (AWGN) from the receiver. It should be noted that the AWGN is present in all receivers and thus indispensable when analyzing any coherent system.

We begin our analysis by deriving the spectral response of the FM-noise contribution due to stochastic carrier generation in the passive sections. The spectral shape of the filtered FM noise from 200 kHz to 400 MHz displays a lowpass response and we will show that this is directly related to the dynamics of the carrier density in the passive sections. The carrier density rate equation in the passive sections [9, 10] is given by:

$$\frac{dN(t)}{dt} = \frac{I(t)}{qV} - \left[a_N N(t) + b_N N^2(t) + c_N N^3(t)\right] + F_N(t) \tag{2.18}$$

where $N(t)$ is the carrier density and $I(t)$ is the injected current; a_N, b_N and c_N are non-radiative, bimolecular radiative and Auger recombination coefficients, respectively. $F_N(t)$ is a generalized Langevin force term accounting for stochastic carrier recombination and generation in the passive sections. The random current fluctuation on the tuning section can be modeled as $I(t) = I_0 + \Delta I(t)$. I_0 is the average current and its small fluctuation, $\Delta I(t)$, is taken to possess white Gaussian statistics. Both F_N and ΔI induce fluctuations in carrier density about a quiescent value N_0, which is the steady-state carrier density under injection current I_0. N_0 and I_0 are related by:

$$\frac{I_0}{qV} - a_N N_0 - 2b_N N_0^2 - 3c_N N_0^3 = 0 \tag{2.19}$$

We make the valid assumption that the magnitude of $\Delta N(t) \ll N_0$, allowing us to linearize equation 2.18 by retaining terms that are first-order in ΔN and normalizing with respect to N_0 to yield $\Delta n(t) = \Delta N(t)/N_0$ as follows:

$$\frac{d\Delta n(t)}{dt} = \frac{\Delta I(t)}{qVN_0} - \Delta n(t)(a_N + 2b_N N_0 + 3c_N N_0^2) + \frac{F_N(t)}{N_0} \tag{2.20}$$

Combining $\Delta I(t)/qVN_0$ and $F_N(t)/N_0$ into a single Langevin force term $F_{\Delta I,N}$, noting that $\beta = a_N + 2b_N N_0 + 3c_N N_0^2$, taking the Fourier transform of equation 2.20, and re-arranging we obtain

$$\frac{\Delta\tilde{n}(\omega)}{\tilde{F}_{\Delta I,N}(\omega)} = \frac{1}{\beta + i\omega} \tag{2.21}$$

which describes a first-order lowpass filter whose 3 dB bandwidth is β. The normalized carrier density fluctuation $\Delta\tilde{n}(\omega)$ in the tuning section leads to the fluctuation in the effective refractive index which in turn induces variations in the laser emission frequency $\Delta f(\omega)$ as the carrier dynamics are on longer timescales (tens of nanoseconds) than a few laser cavity round-trip times (tens of picoseconds). As $\tilde{F}_{\Delta I,N}(\omega)$ is assumed to possess a uniform spectrum induced from

Gaussian noise, the shape of the spectral content of $\Delta f(\omega)$ will be proportional to the form of the lowpass filter given by the right hand side of equation 2.21. In other words, the FM-noise contribution from the passive section is proportional to:

$$S_f(\omega) = \frac{1}{b^2 + \omega^2} \tag{2.22}$$

where $b = \beta = a_N + 2b_N N_0 + 3c_N N_0^2$ is the cut-off angular frequency of $S_f(\omega)$. The simple expression in 2.21 agrees well with the FM-noise spectrum derived in [9]. We now can estimate the cut-off frequency of the lowpass model $S_f(\omega)$ for the filtered FM noise induced from the tuning section. For example, given the phase section structure of the SG-DBR laser in [11] with: length $=$ 80 μm, width $=$ 3 μm, waveguide thickness $=$ 0.35 μm, the typical value for recombination coefficients: $a_N = 0.5 \times 10^8 (s^{-1})$, $b_N = 1 \times 10^{-16} (m^3 s^{-1})$ and $c_N = 1.3 \times 10^{-41} (m^6 s^{-1})$, a phase section current of 8mA will yield a cut-off frequency, $f_{cut-off}$, of 95.6 MHz. Figure 2.8 shows that the cutoff frequency increases exponentially when reducing the section length. In the particular case of SG-DBR lasers, the phase section is much shorter than the grating sections (Front and Back), which explains why the excess noise mostly comes from the phase section as observed in [12]. For the case of multiple tuning sections in SG-DBR lasers, the entire filtered FM noise will be the summation from all the passive sections [9].

In summary, for semiconductor lasers the entire FM-noise spectrum can be described as:

$$S_f(f) = \frac{\nu_{STH}}{\pi} \left[1 + \frac{\alpha^2 f_r^4}{(f_r^2 - f^2)^2 + (\Gamma f / 2\pi)^2} \right] + S_0 \left(\frac{f_1}{f} + \frac{f_2^2}{f^2} \right) + \sum_{k=1}^{3} \frac{a_k^2}{b_k^2 + (2\pi f)^2} \tag{2.23}$$

The first term represents the complete STH phase noise including relaxation oscillation presented in equation 2.16, the second is the excess FM-noise and the third is the filtered FM-noise from the passive tuning sections and can be omitted for lasers without passive tuning sections. The FM-noise spectral shape of the STH phase noise is determined by the carrier density relaxation oscillation in the aftermath of a random spontaneous recombination event and represents the complete treatment of the line-broadening of semiconductor lasers due to spontaneous emission as discussed in previous sections. The relaxation oscillation shapes the FM-noise spectrum above 1 GHz; we illustrate this using representative values of $f_r = 5GHz$ and $\Gamma = 9 \times 10^9 s^{-1}$. The second term in equation 2.23

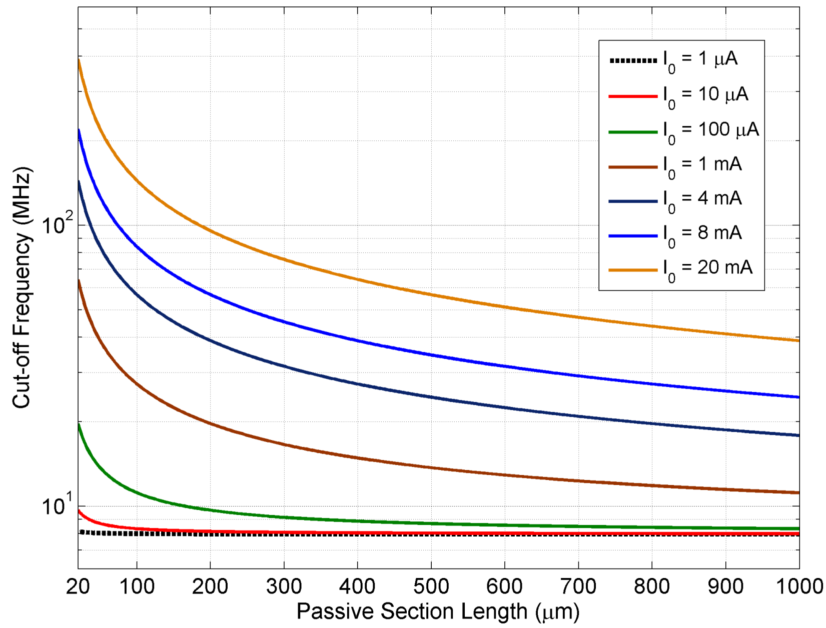

Figure 2.8: The dependency on section length of cut-off frequency of filtered FM noise from passive section of a monolithic tunable laser.

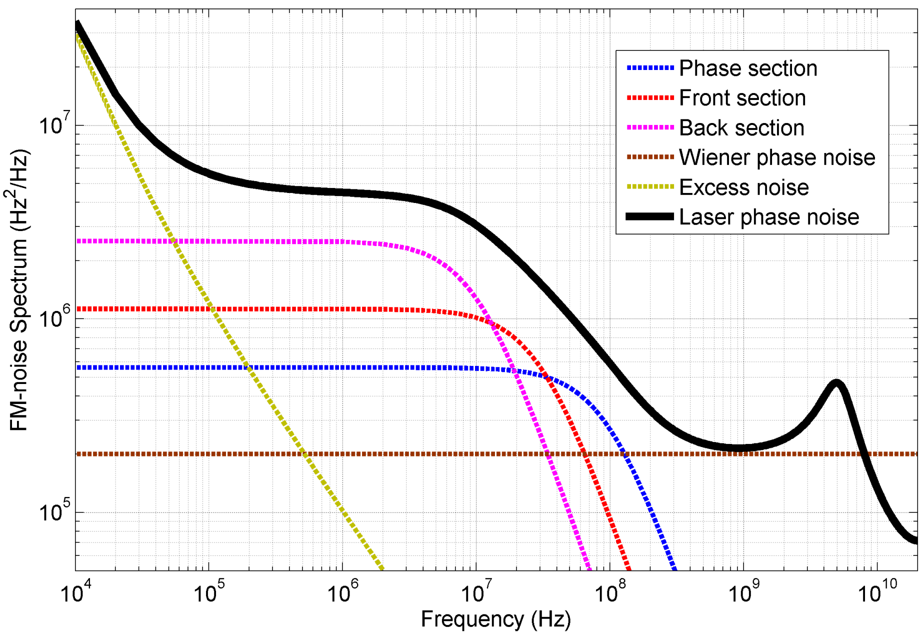

Figure 2.9: Calculations using the analytical models showing the breakdown of the FM-noise spectrum of an SG-DBR laser.

accounts for the excess FM noise [7] with f_1 and f_2 being the break frequencies of flicker noise (briefly discussed in the preceding section, where $K_1 = S_0 f_1$) and frequency random-walk noise, respectively. Especially, in SG-DBR laser, these two types of FM-noise have significant contributions in the total phase noise. We will discuss in more details these two important $1/f^\alpha$ noise processes in the next chapter. To our knowledge, the origin of the $1/f^\alpha$ noise processes is unclear. It would be complicated to theoretically relate the flicker noise and frequency random-walk noise to laser physics in this work. Figure 2.9 shows example calculations from the analytic FM-noise models for an SG-DBR laser. The STH phase noise follows a Wiener process or phase random-walk process (noted as *Wiener phase noise* and has a value of $S_0 = 2 \times 10^5 Hz^2/Hz$) sets the baseline FM-noise floor. We incorporate the lowpass model for the passive sections with coefficients: $b_1 = 2\pi \times 95.6 \times 10^6 (rad/s)$, $b_2 = 2\pi \times 30 \times 10^6 (rad/s)$, $b_3 = 2\pi \times 10 \times 10^6 (rad/s)$, $a_1 = 4.5 \times 10^{11} (Hz\sqrt{Hz})$, $a_2 = 2 \times 10^{11} (Hz\sqrt{Hz})$, $a_3 = 1 \times 10^{11} (Hz\sqrt{Hz})$ and the excess noise with the coefficients: $f_1 = 500kHz$, $f_2 = 100kHz$.

2.3 Summary

In this chapter, the theory of phase noise in the semiconductor laser has been reviewed. Beside the quantum noise limit, in semiconductor lasers, the additional coupling between the intensity fluctuation and phase fluctuation after the spontaneous emission events will also broaden the laser linewidth. The important Henry linewidth enhancement factor and relaxation oscillations in semiconductor lasers have been re-derived. In addition, the semiconductor lasers also exhibit the flicker noise ($1/f$ noise) as for other kinds of oscillators. Finally, the monolithic tunable lasers with passive tuning sections employing grating tuning mechanism demonstrate more additional phase noise processes including: random-walk frequency ($1/f^2$ noise) and filtered FM-noise.

Subsequently, to measure the phase noise of semiconductor lasers, we would need some efficient and highly accurate phase noise characterization methods. The next chapter will investigate the proposed phase noise measurement methods. The measurement results on phase noise of different type of lasers, especially the SG-DBR laser, will also be extensively analysed.

Bibliography

[1] A. L. Schawlow, C.H. Townes, "Infrared and optical maser," Physical Review, vol. 112, pp. 1940-1949, 1958.

[2] C.H. Henry, "Theory of the linewidth of semiconductors lasers," IEEE Journal of Quantum Electronics, vol. QE-18, pp. 259 - 264, 1982.

[3] W.T. Tsang, "Semiconductors and Semimetals," Academic Press Inc., vol. 22, Part B, Chapter 3, 1985.

[4] C.H. Henry, "Phase noise in semiconductor lasers," IEEE/OSA Journal of Lightwave Technology, vol. LT-4 , no. 3, pp. 298 - 311, 1986.

[5] C.H. Henry, "Theory of the phase noise and power spectrum of a single mode injection laser," IEEE Journal of Quantum Electronics, vol. QE-19, pp. 1391 - 1397, 1983.

[6] M. Osinski, J. Buus, "Linewidth broadening factor in semiconductor lasers - an overview," IEEE Journal of Quantum Electronics, vol. QE-23, pp. 9 - 28, 1987.

[7] Tam N. Huynh, Lim Nguyen, Liam Barry, "Phase Noise Characterization of SG-DBR Lasers using Phase Modulation Detection Method With Delayed Self-Heterodyne Measurement," IEEE/OSA Journal of Lightwave Technology, vol. 31, pp. 1300-1308, 2013.

[8] K. Kikuchi, "Effect of 1/f-type FM noise on semiconductor-laser linewidth residual in high-power limit," IEEE Journal of Quantum Electronics , vol. 25, pp. 563–570, 1989.

[9] J. Buus, M.C. Amann, D.J. Blumenthal, "Tunable laser diodes and related optical sources," New Jersey: Wiley Interscience, 2005.

[10] Tam N. Huynh, S. Ó Dúill, L. Nguyen, L.A. Rusch, Liam P. Barry, "A simple analytical model for low frequency FM noise of monolithic tunable lasers ," OSA Applied Optics, to be published, 2014.

[11] M.L. Masanovic, "Wavelength-agile photonic integrated circuits for all-optical wavelength conversion," PhD Thesis, University of California Santa Barbara, 2004.

[12] T.N. Huynh, F. Smyth, L. Nguyen, L.P. Barry, "Effects of phase noise of monolithic tunable laser on coherent communication systems," OSA Optics Express, vol. 20, pp. B244–B249, 2012.

Chapter 3

Laser Phase Noise Characterization Techniques

As discussed in the previous chapters, advanced optical modulation formats which offer high spectral efficiency are being increasingly developed for Dense Wavelength Division Multiplexing systems [1, 2]. Various modulation schemes such as Quadrature Phase Shift Keying [2] and Quadrature Amplitude Modulation [1, 2] with digital coherent receivers have attracted attention recently as potential candidates for next generation optical networks. In coherent optical communications the phase noise of semiconductor lasers has been identified as a crucial characteristic that affects the system performance [3, 4]. This has led to extensive measurement efforts to determine the phase noise characteristics of lasers for transmitters and local oscillators in these systems [5, 6, 7, 8].

In this chapter, we extensively investigate the phase noise in semiconductor lasers. The analytical basis of the phase noise measurement methods including a novel Delayed Self-Heterodyne using Phase Modulation Detection (DSH-PM) technique, and the conventional Delayed Self-Homodyne using coherent detection technique, will be firstly derived in section 3.1. Section 3.2 will explain the experimental setups to perform these phase noise characterization methods. Employing the proposed DSH-PM method, the phase noise measurement results of different types of semiconductor lasers will be extensively analysed in section 3.3. Finally, section 3.4 will conclude the chapter.

3.1 Laser phase noise characterization methods

Among the various measurement techniques for phase noise characterization, the Delayed Self-Heterodyne method has been widely employed to determine the laser linewidth from the full-width half-maximum of the electrical spectrum of the modulating carrier frequency [7, 8]. However, as it only measures the 3-dB linewidth, conventional self-heterodyne measurements can not fully characterize the laser phase noise [5, 7]. This conventional method fails to distinguish the individual contributions of different phase noise processes. In modern coherent optical communications systems, where the phase of the optical field is used to carry information, the need for detailed understanding of the different phase noise processes in semiconductor lasers becomes important. Recently, we proposed a novel technique for phase noise measurements using the Delayed Self-Heterodyne method with Phase Modulation detection [9]. The proposed technique can determine the differential phase coherently, thus allowing a more complete characterization of the phase noise for different lasers. In this section, we review the analytical model for the proposed method and compare it with the conventional Delayed Self-Homodyne method employing coherent receiver.

3.1.1 Analytical Model for Delayed Self-Heterodyne method using Phase-Modulation detection

In this sub-section, we review the theoretical basis of the Phase Modulation (PM) detection for the Delayed-Self Heterodyne method as shown by the block diagram in Fig. 3.1a. The main idea of the proposed measurement method is as follows. The light from the semiconductor laser will be split into two paths, one path will be sufficiently delayed (to de-correlate between the two E-fields), while the other path will be modulated by an optical phase modulator. By looking at both the first and the second harmonics of the detected signal after the two optical paths are recombined, we can coherently recover the full-field information of the differential electric field combined from the two paths.

The electric field of the optical output from a single-mode laser can be expressed in complex notation as:

$$E(t) = \sqrt{P_0 + \Delta P(t)} \times e^{j[\omega_0 t + \phi_n(t)]} \tag{3.1}$$

where $P_0 + \Delta P(t)$ is the optical output power, ω_0 is the angular optical frequency and $\phi_n(t)$ is the laser phase noise. The incident E-field on the photodetector can be written in terms of the delayed and phase-modulated signals:

$$\begin{aligned} E_i(t) &= \frac{1}{2}\left[\gamma E(t-T) - E(t) \times e^{j[b\sin(\omega_c t + \phi_c)]}\right] \\ &= \frac{1}{2}E(t)\left[\gamma e^{-j[\omega_0 T + \phi_n(t) - \phi_n(t-T)]} - e^{j[b\sin(\omega_c t + \phi_c)]}\right] \end{aligned} \tag{3.2}$$

Here γ is the splitting ratio between the two arms, T is the delay of the fiber spool, b is the PM index, and ω_c, ϕ_c are the modulating carrier frequency and phase of the driving signal at the phase modulator input, respectively. The negligible intensity fluctuation of a single-mode laser operating well above threshold is assumed to be unchanged over the delay time so that $\Delta P(t-T) \approx \Delta P(t)$. The output electrical current from the photo-detector having responsivity R is proportional to the intensity which is itself determined by the slowly varying envelope of the incident field (or the lowpass component of the crossing term):

$$\begin{aligned} i_{pd}(t) &= \mathcal{R} \times E_i(t)E_i^*(t) \\ &= \frac{\gamma\mathcal{R}\left[P_0 + \Delta P(t)\right]}{2} \times \\ &\quad \left[\frac{(1+\gamma^2)}{2\gamma} - \cos\left[\omega_0 T + \phi_n(t) - \phi_n(t-T) + b\sin(\omega_c t + \phi_c)\right]\right] \end{aligned} \tag{3.3}$$

Ignoring the DC term (which can be cancelled by means of a DC-Block or balanced photo-detectors) and expanding the second term in equation 3.3 with $\Delta\phi_n(t) = \phi_n(t) - \phi_n(t-T)$:

$$\begin{aligned} i_{pd}(t) &= -\frac{\gamma\mathcal{R}\left[P_0 + \Delta P(t)\right]}{2}\cos\left[\omega_0 T + \Delta\phi_n(t)\right]\cos\left[b\sin(\omega_c t + \phi_c)\right] \\ &\quad + \frac{\gamma\mathcal{R}\left[P_0 + \Delta P(t)\right]}{2}\sin\left[\omega_0 T + \Delta\phi_n(t)\right]\sin\left[b\sin(\omega_c t + \phi_c)\right] \end{aligned} \tag{3.4}$$

Recall the Bessel coefficient expansions:

$$\begin{aligned} \cos\left[b\sin(\omega_c t + \phi_c)\right] &= \mathcal{J}_0(b) + 2\sum_{k-even}^{\infty}\mathcal{J}_k(b)\cos\left[k(\omega_c t + \phi_c)\right] \\ \sin\left[b\sin(\omega_c t + \phi_c)\right] &= 2\sum_{k-odd}^{\infty}\mathcal{J}_k(b)\sin\left[k(\omega_c t + \phi_c)\right] \end{aligned} \tag{3.5}$$

where $\mathcal{J}_k(b)$ is the Bessel function of the first kind with integer order k. The in-phase component $I(t) = \cos\left[\Delta\phi_n(t) + \omega_0 T\right]$ and quadrature component $Q(t) = \sin\left[\Delta\phi_n(t) + \omega_0 T\right]$ of the differential phase noise $\Delta\phi_n(t)$ (plus a constant phase offset $\omega_0 T$) can then be found at even and odd harmonics of the photo-detector electrical signal in equation 3.4. In particular at the first and second harmonics they are given by:

$$i_{pd}^{(1^{st})}(t) = \mathcal{J}_1(b)\gamma\mathcal{R}\left[P_0 + \Delta P(t)\right] Q(t) \sin(\omega_c t + \phi_c)$$

$$i_{pd}^{(2^{nd})}(t) = -\mathcal{J}_2(b)\gamma\mathcal{R}\left[P_0 + \Delta P(t)\right] I(t) \cos\left[2(\omega_c t + \phi_c)\right] \tag{3.6}$$

Notice that the in-phase component can also be found from the base-band term as:

$$i_{pd}^{(bb)}(t) = -\frac{1}{2}\mathcal{J}_0(b)\gamma\mathcal{R}\left[P_0 + \Delta P(t)\right] I(t) \tag{3.7}$$

Assuming that the intensity noise $\Delta P(t)$ is negligible, equations 3.6 show that $i_{pd}(t)$ can be coherently demodulated to recover the differential phase noise$\Delta\phi_n(t)$. In off-line DSP, the captured data of $i_{pd}(t)$ are demodulated by $-\cos\left[2(\omega_c t + \phi_c)\right]$ and $\sin(\omega_c t + \phi_c)$. A simple carrier phase recovery algorithm estimates ϕ_c prior to demodulation. The phase recovery was implemented by sweeping the carrier phase from 0 to 2π and selecting ϕ_c so that it maximizes the root-mean-square (rms) value of the demodulated signal. The low-noise and stable microwave signal generator in our experiment obviates the need to track ϕ_c over the sampling period. Notice that the modulation index b should be adjusted so that $\mathcal{J}_1(b) = \mathcal{J}_2(b)$, or $b \approx 2.63$, for balanced I/Q outputs.

The phase noise analysis evaluates (i) E-field power spectral density (PSD), (ii) phase-error variance, and (iii) FM-noise spectrum [5]. Due to the nature of the self-heterodyne method, these measures will be twice the actual values of the laser linewidth. Thus, for example, the estimated 3-dB FWHM linewidth, of the laser is one-half of the 3-dB FWHM bandwidth of the one-sided PSD measured at the first or second harmonic of the modulating carrier. The phase-error variance over a time interval τ can be determined from the measured phase noise as:

$$\begin{aligned}
\sigma^2_{\Delta\phi}(\tau) &= \left\langle \left[\Delta\phi_n(t) - \Delta\phi_n(t-\tau)\right]^2 \right\rangle \\
&= \left\langle \left\{\left[\phi_n(t) - \phi_n(t-T)\right] - \left[\phi_n(t-\tau) - \phi_n(t-\tau-T)\right]\right\}^2 \right\rangle \\
&= \left\langle \left\{\left[\phi_n(t) - \phi_n(t-\tau)\right] - \left[\phi_n(t-T) - \phi_n(t-T-\tau)\right]\right\}^2 \right\rangle
\end{aligned}$$

$$\Rightarrow \sigma^2_{\Delta\phi}(\tau) = 2\left\langle \left[\phi_n(t) - \phi_n(t-\tau)\right]^2 \right\rangle = 2\sigma^2_{\phi}(\tau) \tag{3.8}$$

for $\tau \ll T$, and sufficiently large T so that $\phi_n(t)$ and $\phi_n(t-T)$ are statistically uncorrelated. The phase-error variance of the laser, $\sigma^2_\phi(\tau) = \langle(\phi_n(t) - \phi_n(t-\tau))^2\rangle$ is thus one-half of the differential phase-error variance, $\sigma^2_{\Delta\phi}(\tau)$, determined from

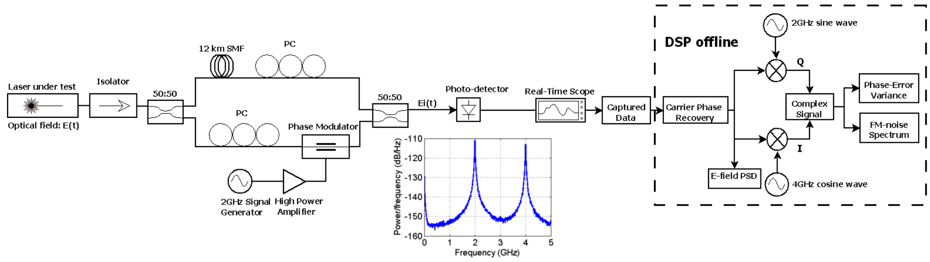

(a) Self-Heterodyne PM detection method

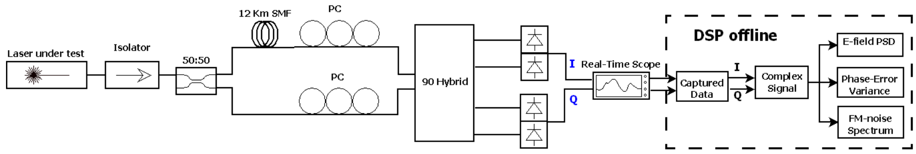

(b) Self-Homodyne optical coherent receiver method

Figure 3.1: Experimental setups for self-heterodyne PM detection method and self-homodyne optical coherent receiver method

the self-heterodyne (or self-homodyne) measurements. If the laser phase noise was ideally described by a random walk process, the phase-error variance as determined from equation 3.8 would increase linearly with τ and the slope from a linear fit to the measurements will be given as $2\pi(2\Delta\nu)$. The FM-noise spectrum is defined as the PSD of the instantaneous frequency which can be obtained by differentiating the phase noise. The estimated 3-dB linewidths from the FM-noise spectra could be determined from the white noise region, S_0, of the measurements: $\Delta\nu = \pi(S_0/2)$ [6].

3.1.2 Analytical Model for Delayed Self-Homodyne method with optical coherent receiver

In order to evaluate the PM detection technique, we have also carried out delayed self-homodyne measurements with an optical 90^o hybrid as illustrated in Fig. 3.1b and Fig. 3.2. The fundamental functions of the optical 90^o hybrid can be found in, for example, reference [2]. The basic idea of this measurement method is that: the light from the semiconductor laser will be split into two paths and one path will be sufficiently delayed as in the previous DSH-PM method; however the other path will not be modulated and the two de-correlated E-fields will directly enter the optical 90^o hybrid; finally the full-field information of the differential electric field will be recovered from received baseband signal.

The E-fields at the inputs to the 90^o hybrid in Fig. 3.2 are:

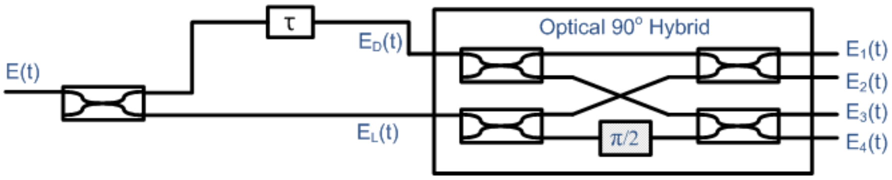

Figure 3.2: Delayed self-homodyne method for phase noise characterization with optical 90^o hybrid

$$\begin{bmatrix} E_D(t) \\ E_L(t) \end{bmatrix} = \frac{1}{\sqrt{2}} \begin{bmatrix} \gamma E(t) \times e^{-j[\omega_0 T + \phi_n(t) - \phi_n(t-T)]} \\ jE(t) \end{bmatrix} \tag{3.9}$$

where $E_D(t)$ and $E_L(t)$ denote the E-field of delayed arm and through arm, respectively. The E-field transfer matrix of the 90^o hybrid [2] can be expressed as:

$$\begin{bmatrix} E_1(t) \\ E_2(t) \\ E_3(t) \\ E_4(t) \end{bmatrix} = \frac{1}{2} \begin{bmatrix} 1 & 1 \\ 1 & -1 \\ 1 & -j \\ 1 & j \end{bmatrix} \begin{bmatrix} E_D(t) \\ E_L(t) \end{bmatrix} \tag{3.10}$$

where $E_{1-4}(t)$ are the incident E-fields to the four photodiodes. The output electrical currents from the two upper photo-detectors are:

$$\begin{aligned} I_1(t) &= \frac{\gamma \mathcal{R}[P_0 + \Delta P(t)]}{4} \left\{ \frac{(1+\gamma^2)}{2\gamma} + \cos\left[\omega_0 T + \Delta\phi_n(t) + \frac{\pi}{2}\right] \right\} \\ I_2(t) &= \frac{\gamma \mathcal{R}[P_0 + \Delta P(t)]}{4} \left\{ \frac{(1+\gamma^2)}{2\gamma} - \cos\left[\omega_0 T + \Delta\phi_n(t) + \frac{\pi}{2}\right] \right\} \end{aligned} \tag{3.11}$$

The output current on the upper balanced photo-detector can then be expressed as:

$$I_Q(t) = I_2(t) - I_1(t) = \frac{\gamma \mathcal{R}[P_0 + \Delta P(t)]}{2} \sin\left[\omega_0 T + \Delta\phi_n(t)\right] \tag{3.12}$$

The output current on the lower balanced photo-detector can be determined in a similar fashion to yield:

$$I_I(t) = I_3(t) - I_4(t) = \frac{\gamma \mathcal{R}[P_0 + \Delta P(t)]}{2} \cos\left[\omega_0 T + \Delta\phi_n(t)\right] \tag{3.13}$$

Thus, the in-phase and quadrature components of the differential phase noise $\Delta\phi_n(t)$ can be obtained with self-homodyne method as shown by equations 3.12 and 3.13. The phase noise analysis is then carried out for the captured I/Q data to determine the E-field PSD, phase-error variance and FM-noise spectrum as described previously.

3.2 Experiment setup for phase noise measurements

The initial experimental setup for phase noise measurements with the DSH-PM technique is shown in Fig. 3.1a, in which the laser under test was optically isolated and then split into two arms by a coupler. The delayed arm was a 12 km SMF fiber spool which is equivalent to a delay, T, $\approx 60\mu s$. The other arm went through a phase modulator driven by a 2 GHz signal generator. The light from the delayed and phase modulated arms were recombined via a second coupler. An 11 GHz photo-detector with an integrated transimpedance amplifier (TIA) detects the incident light from the coupler output. An Agilent real-time scope captured the TIA output signal at 20 GSa/s for 200K samples that were then fed into a computer for post-processing as shown in the DSP-offline block in Fig. 3.1a. The signal generator output was amplified to 19 dBm to provide sufficient drive (PM index b) to the modulator in order to achieve equal powers at the first and second harmonics on an RF spectrum analyzer, as indicated by the inset in Fig. 3.1a.

Figure 3.1b shows the experimental setup for the delayed self-homodyne phase noise measurement. The delayed arm employs the same 12 km fiber and the two arms are now fed into a 90^o hybrid. The optical outputs of the hybrid were detected by a pair of 30 GHz balanced receivers with integrated TIAs. The real-time oscilloscope captured I and Q output signals from the balanced receivers for post-processing. In both methods, the lasers under test were biased well above their respective threshold currents.

To fully characterize the phase noise of semiconductor lasers, we simultaneously use three measures: the power spectral density of the electric field, the phase error variance $\sigma_\phi^2(\tau)$ where τ is the delay time interval, and the FM-noise spectrum as discussed in the previous chapter. The relationship between the three phase noise measures can be summarized in Fig. 3.3 and table 3.1 [5].

3.3 Phase noise measurement results for semiconductor lasers

Employing the measurement experiment setup presented in the previous section, we carried out extensive phase noise characterizations of different kinds of semiconductor lasers. In this section, we report experimental results of phase noise analysis for: distributed feedback lasers (DFB), external cavity lasers (ECL), and

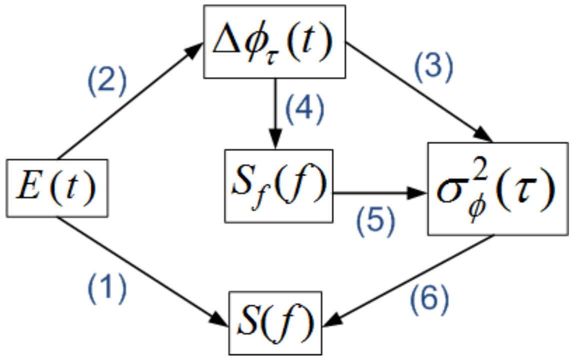

Figure 3.3: Relations between the complex E-field $E(t)$, the phase error (phase difference) $\Delta\phi_\tau(t)$, the field spectrum $S(f)$, the FM-noise spectrum $S_f(f)$, and the phase-error variance $\sigma_\phi^2(\tau)$ [5].

Equation number	Equation
(1)	$S(f) = \langle \lvert F[E(t)] \rvert^2 \rangle$
(2)	$\Delta\phi_\tau(t) = \phi(t) - \phi(t-\tau)$
(3)	$\sigma_\phi^2(\tau) = \langle \Delta\phi_\tau^2(t) \rangle$
(4)	$S_{\Delta\phi_\tau}(f) = 4\left[\frac{\sin(\pi f \tau)}{f}\right]^2 S_f(f)$
(5)	$\sigma_\phi^2(\tau) = 4\int_0^\infty \left[\frac{\sin(\pi f \tau)}{f}\right]^2 S_f(f) df$
(6)	$S(f) = F\left[\exp(-\frac{\sigma_\phi^2(\tau)}{2})\right]$

Table 3.1: Equations for Fig. 3.3, $F[*]$ represents the Fourier transform, and $\langle * \rangle$ is the ensemble average [5].

especially, the four-section SG-DBR laser. The measurement results of the conventional DFB laser from the two phase noise characterization methods are also used to evaluate the accuracy of the proposed DSH-PM method. The feasibility of these lasers in coherent optical communications applications will also be discussed.

3.3.1 Phase noise measurements of Distributed Feedback lasers

Figure 3.4 shows the results of the DFB laser phase noise analysis using the DSH-PM and the self-homodyne methods. For each method, the results were obtained by analyzing the PSD of the received E-field, phase-error variance and FM-noise spectrum. For the PM detection method, the one-sided PSD of the E-field at the first harmonic (2 GHz) in Fig. 3.4a yields an estimated 3-dB linewidth of 6.5 MHz. Figure 3.4c plots the measured phase-error variance over a 50 ns time interval to determine a linearly fitted linewidth $\Delta\nu$ of 6.7 MHz. This estimate is consistent with the result from the PSD and demonstrates the random walk in phase characteristics of DFB lasers. The FM-noise spectrum is plotted in Fig. 3.4e showing the white FM noise characteristics which correspond to a random-walk phase fluctuation with a 6.4 MHz linewidth, $\Delta\nu$. The high frequency response is due to low-pass filtering the spurious harmonics of the PM carrier frequency at 2, 4, 6 and 8 GHz using a low pass filter with a 3dB frequency of 900 MHz. The PM frequency could be increased should higher frequency characterization be desired.

The estimated linewidths $\Delta\nu$ using the coherent receiver from Fig. 3.4b, Fig. 3.4d and Fig. 3.4f were 6 MHz, 5.9 MHz, 5.7 MHz, respectively. The FWHM 3dB linewidth was estimated from the single-sided PSD of the received E-field in Fig. 3.4b by measuring the spectral width at 10 dB down, and then dividing the measured value by 3. The estimated linewidths $\Delta\nu$ from the phase-error variance and FM-noise spectrum in Fig. 3.4d and Fig. 3.4f were calculated in a similar manner with the PM detection method. The above results of the DFB laser phase noise measurement show good agreement between the 3-dB linewidth estimates from the E-field PSD, phase-error variance and FM-noise spectrum for the DFB laser. The self-heterodyne method with PM detection and the self-homodyne method with optical coherent receiver results are within about 15% of one another and experimentally validate the proposed method.

In contrast to the advantages of a simple, cost effective measurement setup, the proposed self-heterodyne method with PM detection has some limitations

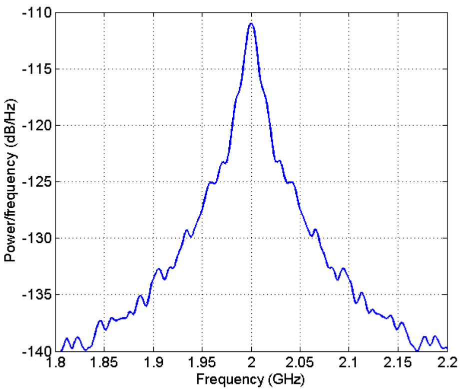

(a) PSD of E-field

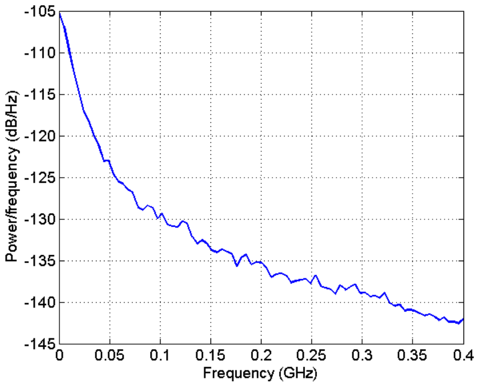

(b) PSD of E-field

(c) Phase-error variance

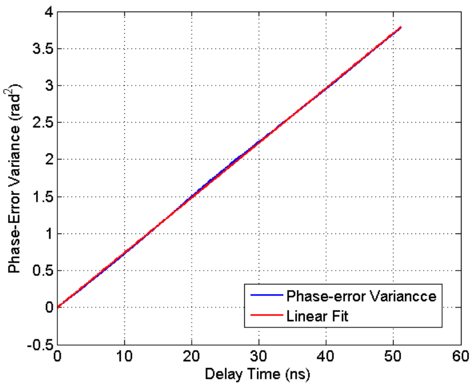

(d) Phase-error variance

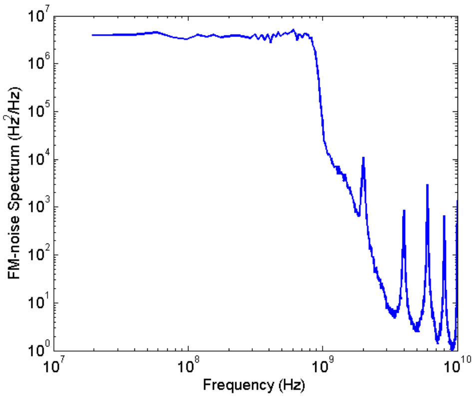

(e) FM-noise spectrum

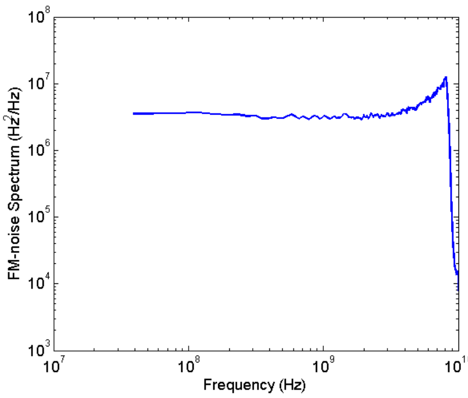

(f) FM-noise spectrum

Figure 3.4: Phase noise measurement for standard DFB laser with Self-Heterodyne using PM detection methods (a,c,e) and Self-Homodyne method (d,b,f)

in terms of the requirement for higher electrical bandwidth receiver and sampling rate of the scope, compared with the conventional delayed self-homodyne method, to observe the same frequency range. Recently, with the development in photonic integration, the cost and complexity of the fully coherent receiver has been reduced significantly. The conventional delayed self-homodyne method has manifested itself as a favorite characterization method with improved accuracy compared with the delayed self-heterodyne method with PM detection.

Besides the white-FM noise, the DFB lasers also experience the low frequency flicker noise as discussed in the previous chapter. Figure 3.5a shows the FM noise spectra of the DFB laser from the DSH-PM method and from the self-homodyne method at 20 GSa/s sampling rate. The FM-noise PSDs that have been plotted in Fig. 3.5a are in good agreement with each other and correspond to an intrinsic linewidth of 6 MHz from the white noise region $S_0 = (\Delta\nu/\pi) = 6 \times 10^6/\pi[Hz^2/Hz]$, and to very low frequency flicker noise with $K_1 = 1.5 \times 10^{11}[Hz^2]$ or $f_1 = K_1/S_0 = 78.5KHz$. The measured phase-error variances from the two methods are in good agreement with each other and also with the analytical models as in Fig. 3.5b over the 50 ns delay interval. The analytical models will be derived in details in the subsection 3.3.3.1. We also performed numerical integration of FM-noise PSD to achieve the phase error variance as in Table 3.1 (with the lower and upper frequency limits of the measurement: $f_L = 1KHz$ and $f_U = 10GHz$) using Gaussian quadrature method to validate the analytical results in Fig. 3.5b. The phase noise analysis for the DFB laser confirms that the white FM noise yields linear phase-error variance as determined by the intrinsic linewidth over short delay intervals that are less than 50 ns. The variance deviates from linearity [5] due to the flicker noise and has moderate quadratic dependency when observed over a longer delay interval. The flicker noise of the DFB laser thus would only affect the performance of low baud-rate systems.

3.3.2 Phase noise measurements of External Cavity lasers

In contrast with DFB lasers, the ECL has additional random-walk frequency fluctuation [7, 9]. This low-frequency noise behavior could be observed in Fig. 3.6 with the DSH-PM method at the reduced sampling rate of 20 MSa/s. The phase variance in Fig. 3.6c deviates significantly from linearity over the $50\mu s$ delay interval. A polynomial fit to the variance in Fig. 3.6c yields the asymptotic slope at zero delay that corresponds to $\Delta\nu \approx 130kHz$. The FM-noise spectrum in Fig. 3.6d shows $1/f^2$ noise below 6 kHz that corresponds to a random walk in frequency, in addition to the dashed line approximation to the white FM noise that corresponds to $\Delta\nu \approx 168kHz$.

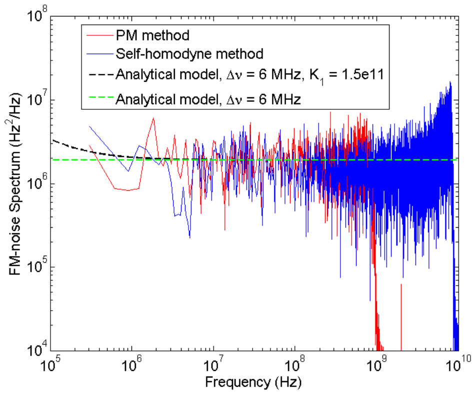

(a) FM spectrum of DFB laser

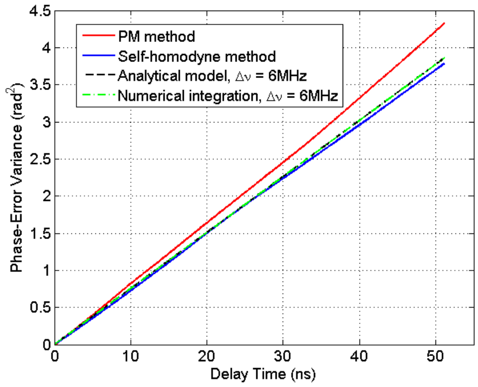

(b) Phase-error variance of DFB laser

Figure 3.5: Analytical and measured FM spectrum and phase-error variance of DFB laser from the DSH-PM method and Self-Homodyne method.

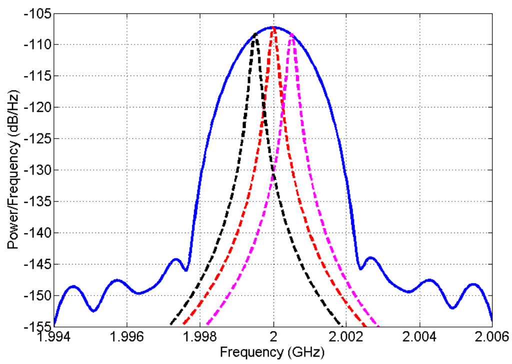

(a) PSD at modulating frequency 2 GHz

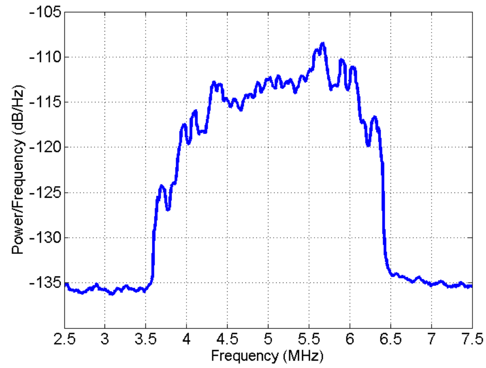

(b) PSD at modulating frequency 5 MHz

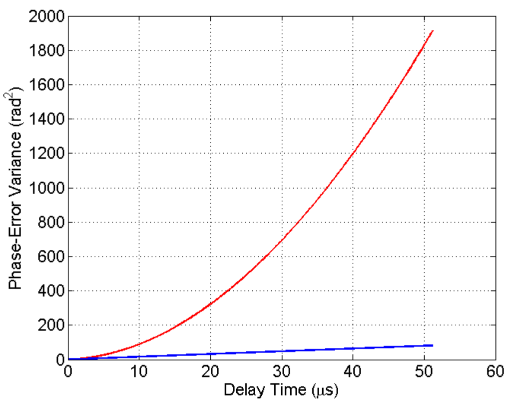

(c) Phase-error variance

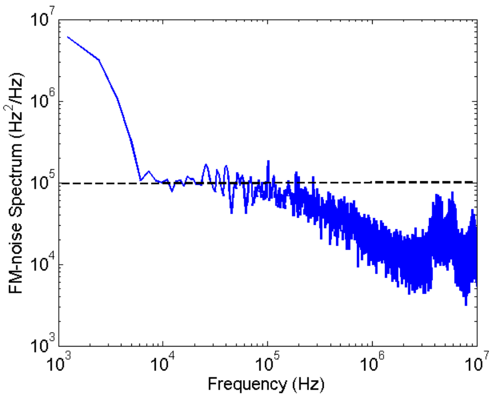

(d) FM-noise spectrum

Figure 3.6: Phase noise measurement for the HP ECL laser

In comparison the 3-dB linewidth estimate from the PSD was nearly twice as large at 350 kHz due to random-walk fluctuation of the optical carrier, as shown by the PSD in Fig. 3.6a, and by the broadening of the averaged electrical spectrum in Fig. 3.6b. The PSDs in dash line presented in Fig. 3.6a were examples of random-walk moving Lorentzian spectral with $\Delta\nu \approx 168kHz$. Similar measurements with the coherent receiver have yielded linewidth estimates of 150 kHz, 155 kHz and 300 kHz that have been determined in the same manner from the phase-error variance, FM-noise spectrum and E-field PSD. In conclusion, the E-field PSD of an ECL overestimates the linewidths that have been determined from the phase-error variance and FM-noise spectrum because the phase noise deviates from the ideal random walk model.

3.3.3 Phase noise measurements of multi-section monolithic tunable lasers

As discussed in the previous chapter, the SG-DBR monolithic tunable laser exhibits additional filtered FM-noise, flicker noise ($1/f$ noise) and random-walk frequency noise ($1/f^2$ noise). Especially, from the experimental observation, the contribution of $1/f$ noise and $1/f^2$ noise to the total phase noise in the SG-DBR laser is significantly important . In this subsection, before analyzing the phase noise characterization results of the SG-DBR laser, we firstly derive the analytical model for phase error variance ($\sigma_\phi^2(\tau)$) from the FM-noise spectrum including white-FM noise, the flicker noise and random-walk frequency noise [10]. This model is useful for the discussion on the measurement results in the next subsection. The phase-error variance is also the widely used measure to evaluate the ultimate BER performance of the coherent communications systems [4].

3.3.3.1 Analytical expression for phase-error variance

The phase noise processes of a semiconductor laser may consist of white FM-noise, flicker noise and random-walk noise so that the FM noise spectrum of the laser can expressed as follows [7, 10]:

$$S_f(f) = S_0 + \frac{K_1}{f} + \frac{K_2}{f^2} = S_0\left[1 + \frac{f_1}{f} + \left(\frac{f_2}{f}\right)^2\right] \tag{3.14}$$

where $f_1 = K_1/S_0$, $f_2 = \sqrt{K_2/S_0}$. Here $S_f(f)$ is the FM noise PSD, S_0 is the uniform PSD of the white FM noise, f_1 and f_2 are the corner or break frequencies of the excess flicker $1/f$ noise, and random-walk $1/f^2$ FM noise, respectively. The measured phase-error variance of the laser can be re-expressed as:

$$\sigma_\phi^2(\tau) = 4\int_{f_L}^{f_U} S_f(f)\frac{\sin^2(\pi f\tau)}{f^2}df \tag{3.15}$$

where f_L and f_U are the lower and upper frequency limits of the measurement system. Replacing $S_f(f)$ with equation 3.14 and substituting $x = \pi f\tau$, equation 3.15 can be rewritten as:

$$\sigma_\phi^2(\tau) = 4\pi S_0\tau\left[\int_{x_L}^{x_U}\frac{\sin^2 x}{x^2}dx + x_1\int_{x_L}^{x_U}\frac{\sin^2 x}{x^3}dx + x_2^2\int_{x_L}^{x_U}\frac{\sin^2 x}{x^4}dx\right] \tag{3.16}$$

The analytical formula for the phase-error variance can be obtained by performing the respective integrations of the white, flicker and random-walk FM noise terms in equation 3.16. The first integral corresponds to white FM noise and can be integrated by parts to yield:

$$I_1 = \int_{x_L}^{x_U}\frac{\sin^2 x}{x^2}dx = -\frac{\sin^2 x}{x}\bigg|_{x_L}^{x_U} + \int_{x_L}^{x_U}\frac{\sin 2x}{x}dx \tag{3.17}$$

or:

$$I_1 = -\frac{\sin^2 x}{x}\bigg|_{x_L}^{x_U} + \int_{y_L}^{y_U}\frac{\sin y}{y}dy \tag{3.18}$$

where $y = 2x$. As x_L approaches zero and x_U goes to infinity, the first term in equation 3.17 vanishes and the second term can be expressed as the *sine integral* function $Si(.)$, $Si(x) = \int_0^x \frac{\sin t}{t}dt$, which converges to $\pi/2$ so that:

$$I_1 \approx \frac{\pi}{2} \tag{3.19}$$

The second integral in equation 3.16 corresponds to flicker FM noise and can be integrated by parts twice as follows.

$$I_2 = \int_{x_L}^{x_U}\frac{\sin^2 x}{x^3}dx = -\frac{\sin^2 x}{2x^2}\bigg|_{x_L}^{x_U} + \int_{x_L}^{x_U}\frac{\sin 2x}{2x^2}dx \tag{3.20}$$

or:

$$I_2 = -\frac{\sin^2 x}{2x^2}\bigg|_{x_L}^{x_U} - \frac{\sin 2x}{2x}\bigg|_{x_L}^{x_U} + \int_{y_L}^{y_U}\frac{\cos y}{y}dy \tag{3.21}$$

As x_L approaches zero and x_U goes to infinity, the first term converges to 1/2 and the second term converges to 1. The third term in equation 3.21 can be written in terms of a *cosine integral* function $Ci(.)$. So the phase-error variance of the flicker noise is given by:

$$I_2 = 1.5 + Ci(2\pi f_U \tau) - Ci(2\pi f_L \tau) \tag{3.22}$$

The third integral in equation 3.16 corresponds to the random-walk FM noise and can be integrated by parts repeatedly as follows.

$$I_3 = \int_{x_L}^{x_U} \frac{\sin^2 x}{x^4} dx = -\frac{\sin^2 x}{3x^3}\bigg|_{x_L}^{x_U} + \int_{x_L}^{x_U} \frac{\sin 2x}{3x^3} dx$$

$$I_3 = -\frac{\sin^2 x}{3x^3}\bigg|_{x_L}^{x_U} - \frac{\sin 2x}{6x^2}\bigg|_{x_L}^{x_U} - \frac{\cos 2x}{3x}\bigg|_{x_L}^{x_U} - \frac{2}{3}\int_{x_L}^{x_U} \frac{\sin 2x}{x} dx \tag{3.23}$$

When x_L approaches zero and x_U goes to infinity, the first term approaches $1/3x_L$, the second term approaches $1/3x_L$, and the third term also approaches $1/3x_L$. The last term is again the *sine integral* which converges to $(2/3)(\pi/2) = \pi/3$.

$$I_3 = \frac{3}{3x_L} - \frac{2\pi}{6} = \frac{1}{\pi f_L \tau} - \frac{\pi}{3} \tag{3.24}$$

Together equations 3.19, 3.22 and 3.24 yield the expression below for the phase-error variance:

$$\sigma_\phi^2(\tau) = 4\pi S_0 \tau \left[\frac{\pi}{2} + (\pi f_1 \tau)\left[1.5 + Ci(2\pi f_U \tau) - Ci(2\pi f_L \tau)\right] + (\pi f_2 \tau)^2 \left[\frac{1}{\pi f_L \tau} - \frac{\pi}{3}\right]\right] \tag{3.25}$$

Finally, with $S_0 = \Delta\nu/\pi$, the formula for the phase-error variance is as below:

$$\sigma_\phi^2(\tau) = 2\pi\Delta\nu\tau \left[1 + (2 f_1 \tau)\left[1.5 + Ci(2\pi f_U \tau) - Ci(2\pi f_L \tau)\right] + \left(\frac{f_2}{f_L}\right)(2 f_2 \tau) - \frac{2}{3}(\pi f_2 \tau)^2\right] \tag{3.26}$$

From equation 3.26, we can observe that the white FM, or Wiener, noise process would yield perfectly linear phase-error variance: $\sigma_\phi^2(\tau) = 2\pi\Delta\nu\tau$ for $f_1 = f_2 = 0$. The flicker FM noise would yield quadratic phase-error variance due to the second term that involves $(f_1\tau)$. In low-noise oscillators the corner frequency for random-walk noise, f_2, would normally occur well below flicker noise: $f_2 \ll f_1$. That is, flicker noise is more dominant and the effects of random-walk FM noise (the last two terms) could be safely ignored. For example, flicker noise is prevalent in DFB lasers where the (moderately quadratic) deviation from linear phase-error variance has been observed [5, 15]. However, in the next subsection, we will show that this is not the case with SG-DBR lasers where random-walk FM noise has been found to be prevalent [11]. Random-walk excess noise that is dominating, i.e., $f_2 \gg f_1$, would yield strongly quadratic phase-error variance due to the third term in equation 3.26 that includes $(f_2\tau)$. Notice in this case that there is also a comparatively weak cubic dependency due to the last component, $(f_2\tau)^2$, that would be significant over a longer interval such that $\pi f_2 \tau > 1$.

We conclude from equation 3.26 that the excess flicker and random-walk FM noise will not affect low baud rate systems if the symbol duration T is sufficiently short such that

$$(2f_1T)\left[1.5 + Ci(2\pi f_U T) - Ci(2\pi f_L T)\right] + \left(\frac{f_2}{f_L}\right)(2f_2T) - \frac{2}{3}(\pi f_2 T)^2] \ll 1$$

It is clear from equations 3.16 and 3.26 that $\sigma_\phi^2(\tau)$ does not converge if $f_L = 0$ with excess noise. It stands to reason that in practice $f_L > 0$ for finite measurements of the phase-error variance since the duration of the observations and measurements is necessarily finite, and an estimate of f_L can be determined from the finite model for $\sigma_\phi^2(\tau)$. This also suggests that the low frequency limit of a digital coherent receiver could affect the system performance in the presence of excess laser phase noise.

3.3.3.2 Experimental results

We employed a four-section (gain, front, back and phase sections) tunable laser that can be quasi-continuously tuned over the C-band. The phase noise of the SG-DBR laser has been reported to consist of (i) white FM-noise from around 1 GHz to less than 6 GHz, (ii) low frequency excess noise at below a few hundreds MHz and (iii) high-frequency relaxation oscillation at approximately 6 GHz [11, 12, 13]. We have performed the measurements with the PM detection technique to characterize the phase noise of the SG-DBR laser so that the performance of coherent optical communication systems employing these tunable lasers could be determined. We note that the relaxation oscillation could also be observed with the PM detection method by increasing the modulating carrier, which is 2 GHz in this work, beyond the relaxation frequency.

Figure 3.7 shows the results of the phase noise analysis for the SG-DBR laser when biasing the gain section only (at 100 mA), with the tuning sections terminated. The PSD of the E-field at the first harmonic shows an estimated linewidth of 5.5 MHz in Fig. 3.7a, while the phase-error variance and the FM-noise spectrum in Figs. 3.7c and 3.7e deviate from the ideal white FM noise model. The FM-noise spectrum in Fig. 3.7e has not only a white noise region that corresponds to a 300 kHz linewidth, but also excess $1/f$ noise below 200 MHz [11, 13].

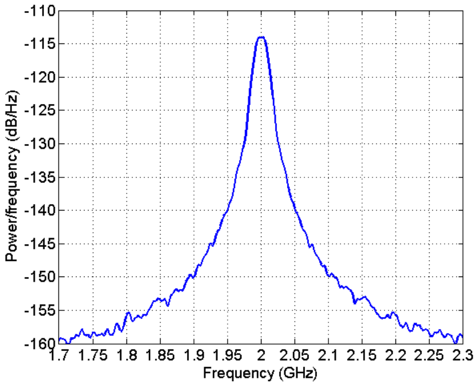

(a) PSD of E-field (Gain section only)

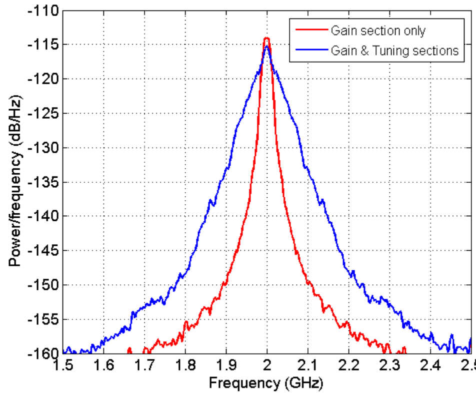

(b) PSD of E-field (comparison)

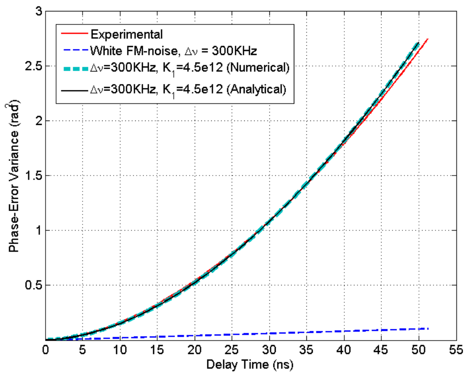

(c) Phase-error variance

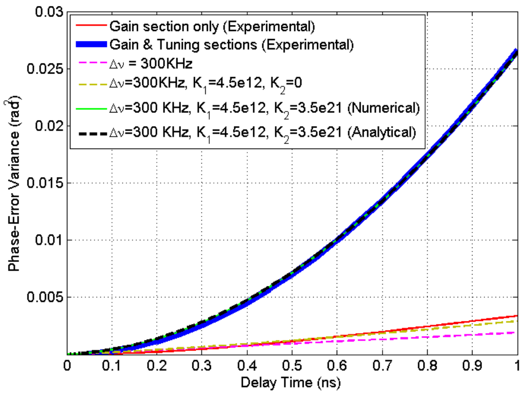

(d) Phase-error variance (Comparison)

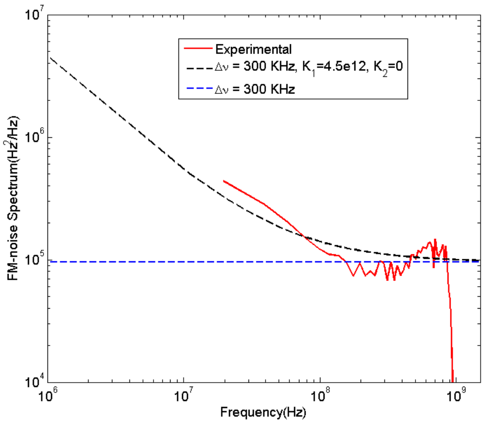

(e) FM-noise spectrum

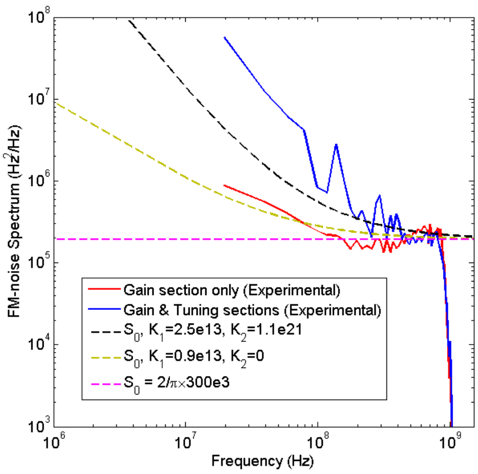

(f) FM-noise spectrum (Comparison)

Figure 3.7: Phase noise measurement of SGDBR laser

The phase-error variance is thus no longer linear as shown in Fig. 3.7c, where the slope at the origin has been approximated by the dashed line using the estimated 300 KHz linewidth from Fig. 3.7e.

The PSD that has been plotted in Fig. 3.7e yields an FM noise model with an intrinsic linewidth of 300 kHz from the white noise region, $S_0 = \Delta\nu/\pi = 3 \times 10^5/\pi[Hz^2/Hz]$, and the flicker noise with $K_1 = 4.5 \times 10^{12}[Hz^2]$ or $f_1 = K_1/S_0 = 47.1\,MHz$. Figure 3.7c plots the analytical phase-error variance determined by equation 3.26 from the FM noise model as well as the numerical integration result of equation 3.15 using Gaussian quadrature method. The results again show a strong agreement between the analytical model and the experiments as shown in Figs. 3.7c and 3.7e.

The excess noise also broadens the observed linewidth [14, 15, 16] of the E-field PSD, shown by Fig. 3.7a. The degree of linewidth broadening is largely determined by its break frequencies [16]. The FM-noise spectrum in Fig. 3.7e shows a break frequency near 50 MHz. As a result, the linewidth of the SG-DBR laser was significantly broadened from 300 KHz due to white FM noise (primarily from spontaneous emission in the active region) to 5.5 MHz due to the presence of excess noise. In terms of device structure, the SG-DBR laser differs from a DFB laser in that it has separate, passive tuning sections. Thus, besides the injection-recombination shot noise that results in excess laser noise [11, 18], the carrier density fluctuation in the tuning regions can have a large contribution on the noise levels [11, 17]. In addition to the excess noise from the current source that biases the tuning sections, as there is no stimulated emission and absorption in the passive regions, the refractive index of these sections will be determined by the fluctuations of the carrier density, while in the active region the excess noise is effectively suppressed thanks to the gain claiming mechanism [17].

Figure 3.7 also compares the phase noise characteristics of the SG-DBR laser when biasing the gain section only, and when simultaneously biasing the gain and tuning sections. The results demonstrated that the tuning regions can introduce significant random-walk FM noise. Figure 3.7b shows that the linewidth from the E-field PSD was further broadened from 5.5 MHz to 19.3 MHz when all sections were biased. The excess noise that causes the linewidth broadening can be observed with the FM-noise spectrum in Fig. 3.7f. The high frequency white FM-noise region was the same for both cases, corresponding to an intrinsic linewidth of about 300 kHz. When all sections were biased, the break frequency of the excess noise extended to about 400 MHz compared to less than 200 MHz when biasing the gain section only. The laser phase noise can be approximately described by the model in equation 3.14 with the white FM noise $S_0 = 3 \times 10^5/\pi[Hz^2/Hz]$, the flicker FM noise $K_1 = 4.5 \times 10^{12}[Hz^2]$ or $f_1 = 47.1MHz$, and the random-walk FM noise $K_2 = 3.5 \times 10^{21}[Hz^3]$ or $f_2 = \sqrt{K_2/S_0} = 191.5MHz$. Figure 3.7d plots the analytical phase-error variance determined by equation 3.26 from the FM noise model as well as the numerical integration result of equation 3.15 using Gaussian quadrature method. The results again show a strong agreement between the analytical model and the experiments as shown in Figs. 3.7d and 3.7f when biasing both gain and tuning sections of the laser. The effect of the random-walk noise can be observed in Fig. 3.7d where the phase-error variance, with all sections biased, deviates from linearity significantly. In particular, the phase-error variance at 1 ns time delay, which corresponds to the symbol time associated with 1 Gbaud line rate, has increased by nearly one order of magnitude compared to the values predicted either by the intrinsic linewidth or the flicker noise. The above analysis shows that the excess phase noise is significant and therefore potentially could degrade the bit-error rate (BER) performance of a coherent communication system. A previously reported DPSK system operating at 1.25 Gbaud experienced a BER floor of around 10^{-5} with an SG-DBR laser transmitter, when biasing all sections [19]. This can be explained from Fig. 3.7d where the phase-error variance at 0.8 ns was about 0.04 rad^2 which is the theoretical limit for DPSK at 10^{-9} BER [20]. The phase noise impact of SG-DBR lasers on duobinary and DQPSK modulated packets at 42.6 Gbit/s line rate has also been described in [21]. As optical coherent systems have been trending towards m-PSK and m-QAM modulation formats, the requirements on the laser phase noise have become even more stringent [2, 3, 4, 5]. In [4], the theoretical limits of the phase error-variance at 10^{-4} BER were derived for different modulation formats with coherent detection based on decision-aided maximum likelihood phase recovery. The authors reported that the limits were $\sigma_\phi^2 = 1.2 \times 10^{-2}$ and $\sigma_\phi^2 = 2.3 \times 10^{-3}$ for QPSK and 16-QAM, respectively. Such phase noise requirements can be effectively characterized by the PM detection method.

3.4 Summary

In this chapter, we have reviewed the two phase noise characterization methods: the proposed delayed self-heterodyne using PM detection techniques and the conventional delayed self-homodyne with optical coherent receiver. The analysis showed that the in-phase and quadrature components of the self-heterodyne signal can be demodulated at the first and second harmonics of the phase modulating carrier, enabling full recovery of the differential phase. In comparison, the delayed self-homodyne method recovers the differential phase via quadrature demodulation at the optical carrier. We then employed the PM–DSH technique to characterize the phase noise of different types of semiconductor lasers. The measurement results confirm that while the phase noise characteristic of the DFB laser is primarily determined by white FM noise with very low frequency flicker noise, the SG-DBR laser in addition has significant excess noise from the tuning sections that causes linewidth broadening due to flicker and random-walk FM noise. The analytical formula to determine the phase-error variance from the FM noise spectrum was derived and the results showed that the excess phase noise is significant and therefore potentially degrades the BER performance of a coherent communication system employing tunable laser transmitter such as SG-DBR devices. The experimental results also show that the contribution of the electrical noise from the power supplies to the passive sections of the SG-DBR laser is significant. That could be reduced through the use of the low noise current source or a battery source to reduce the excess FM-noise from the passive sections.

The requirements on the laser phase noise have become more stringent as coherent optical systems move towards ever higher order modulation formats to achieve better spectral efficiency and increased tolerance to fiber dispersion and non-linearity. Conventional delayed self-heterodyne measurements only determine the laser 3dB linewidth which is insufficient for evaluating the system performance. The PM detection method thus extends the capability of the Delayed-Self Heterodyne technique by coherently recovering the differential E-field of the laser, and provides an effective alternative to the self-homodyne method for optical coherent measurements. This allows for a more complete characterization of the laser phase noise, which in turn enables a more accurate prediction of system performance.

As discussed previously, the laser phase noise is essentially setting the lower bound for the BER performance in coherent optical communications systems where both phase and amplitude of the optical field are utilized to transmit information. The effects of different phase noise processes in semiconductor lasers, especially the SG-DBR laser, on the ultimate performance of the coherent communications systems will be extensively investigated in the next chapter. Based on that investigation, some novel techniques to overcome the impact of large laser phase noise in optical communications will subsequently be proposed and evaluated.

Bibliography

[1] A.H. Gnauck, P.J. Winzer, S. Chandrasekhar, X. Liu, B. Zhu, D.W. Peckham, "Spectrally Efficient Long-Haul WDM Transmission Using 224-Gb/s Polarization-Multiplexed 16-QAM," J. Lightw. Technol., vol. 29, pp. 373-377, 2011

[2] M. Nakazawa, K. Kikuchi, and T. Miyazaki, High spectral density optical communication technologies . Berlin: Springer-Verlag, 2010

[3] M. Seimetz, "Laser Linewidth Limitations for Optical Systems with High-order Modulation Employing Feed Forward Digital Carrier Phase Estimation," OFC 2008, pp. OtuM2

[4] S. Zang, P.Y. Kam, J. Chen, C. Yu, "Bit-error rate performance of coherent optical M-ary PSK/QAM using decision-aided maximum likelihood phase estimation," Optics Express , vol. 18, pp. 549–553, 2005

[5] K. Kikuchi, "Characterization of semiconductor-laser phase noise and estimation of bit-error rate performance with low-speed offline digital coherent receivers," Optics Express, vol. 20, pp. 5291-5302, 2012

[6] J. P. Tourrenc et. al., "Low-Frequency FM-Noise-Induced Lineshape: A Theoretical and Experimental Approach," J. Quantum Electron , vol. 41, pp. 549–553, 2005

[7] S. Camatel and V. Ferrero, "Narrow Linewidth CW Laser Phase Noise Characterization Methods for Coherent Transmission System Applications," J. Lightw. Technol. , vol. 26, pp. 3048–3054, 2008

[8] T. Okoshi, K. Kikuchi, A. Nakazama, "Novel Method for High Resolution Measurement of Laser Output Spectrum," Electron. Lett., vol. 16, p. 630, 1980

[9] Tam N. Huynh, Lim Nguyen, Liam Barry, "Delayed Self-Heterodyne Phase Noise Measurements with Coherent Phase Modulation Detection", Photon. Technol. Lett., vol. 24, pp. 249-251, 2012

[10] Tam N. Huynh, Lim Nguyen, Liam Barry, "Phase Noise Characterization of SG-DBR Lasers using Phase Modulation Detection Method With Delayed Self-Heterodyne Measurement," IEEE/OSA Journal of Lightwave Technology, vol. 31, pp. 1300-1308, 2013.

[11] S. Nakagawa et. al, "Phase noise of Widely-Tunable SGDBR laser," OFC 2003, pp. ThF2

[12] M.C. Larson, Y.A. Akulova, C.W. Coldren, T. Liljeberg, G.A. Fish, S. Nakagawa, A. Dahl, P. Kozodoy, D. Bingo, M. Bai, N. Ramdas, S. Penniman, T. Wipiejewski, L.A. Coldren, "High Performance widely-Tunable SG-DBR Lasers", Proc. SPIE 2003, vol. 4995, pp. 66-80

[13] S. Ristic, A. Bhardwaj, M.J. Rodwell, L.A. Coldren, L.A. Johansson, "An optical phase-locked loop photonic integrated circuit," J. Lightw. Technol. , vol. 28, pp. 526–538, 2010

[14] T. Okoshi and K. Kikuchi, Coherent optical fiber communications. Tokyo: Kluwer, 1988

[15] K. Kikuchi, "Effect of 1/f-type FM noise on semiconductor-laser linewidth residual in high-power limit," J. Quantum Electron , vol. 25, pp. 563–570, 1989

[16] M.J. O'Mahony and I. D. Henning, "Semiconductor laser linewidth broadening due to 1/f carrier noise," Electron. Lett., vol. 19, pp. 1000-1001, 1983

[17] M.C. Amann, R. Hakimi, B. Borchert, S. Illek, "Linewidth broadening by 1/f noise in wavelength-tunable laser diode", Appl. Phys. Lett, vol. 70, pp. 1512-1514, 1997

[18] M.C. Amann and R. Schimpe, "Excess linewidth broadening in wavelength-tunable laser diodes," Electron. Lett., vol. 26, pp. 279-280, 1990

[19] K. Shi, F. Smyth, P.M. Anadarajah, D. Reid, Y. Yu, L.P. Barry, "Linewidth of SG-DBR laser and its effect on DPSK transmission," Optics Communications, vol. 283, pp. 5040-5045, 2010

[20] K. Kikuchi, T. Okoshi, M. Nagamatsu, N. Henmi, "Degradation of bit-error rate in coherent optical communications," J. Lightw. Technol. , vol. 26, pp. 3048–3054, 2008

[21] A.K. Mishra, A.D. Ellis, L.P. Barry, "Time-resolved Q-factor measurement and its application in performance analysis of 42.6 Gbit/s packets generated by SGDBR lasers," J. Lightw. Technol., vol. 28, pp. 1144-1151, 2010

Chapter 4

Laser Phase Noise and Advanced Modulation Formats

In the preceding chapters, the sophisticated phase noise processes of the SG-DBR lasers have been examined. With the aim of deploying this type of monolithic tunable laser in an optical communications system with advanced modulation formats, in this chapter, we will extensively investigate the performance of these systems employing the SG-DBR laser. The complicated phase noise characteristics of the SG-DBR laser pose a significant impact on coherent systems with high order QAM modulation formats. The experimental results expose that: the white FM-noise basically defines the lower bound of the BER performance of a coherent communications system while the other additional FM-noise processes will lead to the unpredictable performance degradation. To overcome this issue, we propose novel methods that either employ advanced DSP in conventional coherent detection systems or new transmission schemes.

The chapter is structured as follows: in section 4.1, we experimentally examine the effects of phase noise of the SG-DBR lasers on a conventional coherent communications system employing high order QAM modulation formats. A new phase tracking algorithm utilizing a second-order decision-directed Phase-Locked Loop (DD-PLL) is proposed to solve the problem of the excess phase noise in SG-DBR lasers. The effects of phase noise of the SG-DBR lasers on Cycle Slips (CS) are also investigated in this section. In the following section, section 4.2, we propose a novel transmission scheme for QPSK employing a Phase Modulation detection technique to overcome the problem of the phase noise in SG-DBR lasers. In section 4.3, a novel Baudrate-Pilot-Aided transmission scheme with direct detection will be demonstrated for 16-QAM modulation format that effectively overcomes the problem of large phase/frequency noise in semiconductor lasers, especially the SG-DBR lasers. Finally, section 4.4 will summarize the chapter.

4.1 The effects of phase noise of monolithic tunable lasers in coherent detection systems

Multi-level modulation has been identified as one of the key technologies to address the capacity increase in Dense Wavelength Division Multiplexing optical networks [1]. Optical transmissions systems employing digital coherent receivers and advanced optical modulation formats which offer high spectral efficiency have thus become a critical enabling component. The phase noise characteristics of the lasers in these coherent systems can limit the bit-error rate performance, especially under higher-order quadrature amplitude modulation schemes from Quadrature Phase Shift Keying, to 16-QAM and to 64-QAM [1, 2]. The 3-dB linewidth from the delayed self-heterodyne measurement has typically been the metric for determining whether the laser will work in a specific coherent system with a certain baud rate and modulation format. However, the observed 3-dB linewidth, which is broadened due to *1/f* noise [3], has been shown to be an incomplete measure of the laser phase noise as discussed in the previous chapter [4, 5]. In this section, we firstly achieve the FM-noise spectrum of a Distributed Feedback laser and a Sampled-Grating Distributed Brag Reflector laser [6] using the Delayed Self-Heterodyne employing Phase Modulation detection technique [4]. We then experimentally evaluate the effects of the laser phase noise on the coherent communications systems employing 16-QAM at 5 Gbaud and QPSK operating at 10.7 Gbaud. Experimental results show that the system operation was significantly affected by the high $1/f^{\alpha}$ noise of the SG-DBR device. The results also confirmed that the white FM noise level largely defines the overall performance of coherent detection.

4.1.1 Basic concept of optical coherent detection

Current optical coherent communications systems (for commercial networks and for majority of current research) are basically deployed as an *intradyne detection* scheme based on the two key optical components: (1) the IQ modulator [7, 8] which consists of two nested single-drive-MZMs and a 90^o phase-shifter on one arm as in Fig. 4.1a; and (2) the optical 90^o hybrid accompanied by two balanced photo-detectors [7, 8] as in Fig. 4.1b. By utilizing these two components, both amplitude and phase of the optical complex field can be manipulated to carry information. The intradyne detection scheme is a coherent reception technique

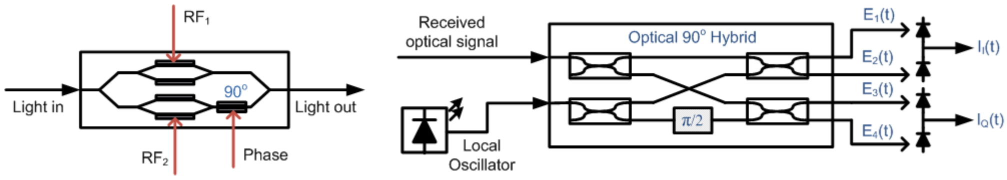

(a) (b)

Figure 4.1: Conceptual illustration of (a) IQ modulator for transmitter, and (b) optical 90^o hybrid for intradyne-receiver in current coherent optical communications systems.

introducing a small frequency offset (much smaller than the system baudrate) between the transmitter laser and the local oscillator. The references [7] and [8] explain in more detail the basic operational concepts of this coherent communications system. In this subsection we will concentrate on the effects of the laser phase noise which defines the lower bound of the BER performance of the fully optical coherent systems.

Following the notation in [9], ignoring the nonlinearity of the fiber link (launched power could be controlled to satisfy this assumption) and fiber dispersion, the received signal in optical coherent systems is contaminated by lasers phase noise and additive Gaussian noise and modeled as:

$$r(k) = c(k)e^{j\theta(k)} + n(k) \tag{4.1}$$

where $c(k)$ is defined as the transmitted symbol, $\theta(k)$ is the laser phase noise at sampling point and $n(k)$ presents the additive Gaussian noise with the variance $N_0/2 = \sigma_N^2$. At the receiver, a referable phase tracking technique could be employed to estimate the laser phase noise $\hat{\theta}(k)$. That leads to a phase error after the phase tracking $\phi(k) = \theta(k) - \hat{\theta}(k)$. We can numerically evaluate the BER $P_b(e)$ based on the probability density function (PDF) of $\phi(k)$ as:

$$P_b(e) = \int_{-\pi}^{\pi} P_b(e|\phi)p(\phi)d\phi \tag{4.2}$$

where $P_b(e|\phi)$ is the BER conditioned on a fixed value of phase error $\phi(k)$ and $p(\phi)$ is the PDF of the phase error.

Firstly, we find the expression for $P_b(e|\phi)$ in equation 4.2. The rigorous derivation of $P_b(e|\phi)$ for QPSK and 16-QAM can be found, for example, in [9]. Secondly, we would need the PDF $p(\phi)$ of the phase error. From the widely known references, the phase error after phase tracking could be well approximated by a zero mean Gaussian distribution [9] or a Tykhonov distribution [10]. For simplicity, we assume the phase error has the zero mean Gaussian distribution with the

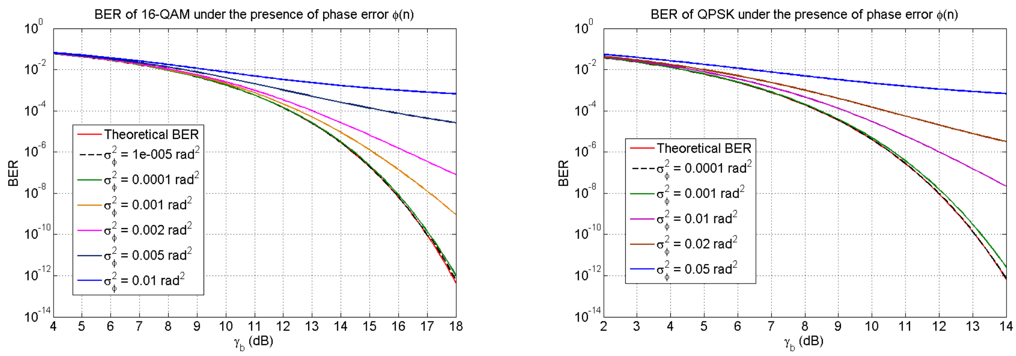

(a) 16-QAM modulation format

(b) QPSK modulation format

Figure 4.2: The effect of laser phase noise on the ultimate BER performance of QAM modulation formats in coherent optical communications.

variance σ_ϕ^2:

$$p(\phi) = \frac{1}{\sqrt{2\pi\sigma_\phi^2}} e^{-\frac{\phi}{2\sigma_\phi^2}} \tag{4.3}$$

Finally, the lower bound of BER performance due to laser phase noise for QPSK and 16-QAM can be found by evaluating equation 4.2 and achieving the same results as reported in [9]. Figure 4.2 depicts these numerical results where γ_b is the signal-noise-ratio per bit. The theoretical BER performances of QAM modulation formats on additive Gaussian noise channel (without phase noise) can be easily found in many communications textbooks [11]. Here we use them as the benchmark of the system for comparison.

According to the theoretical limits in Fig. 4.2, we can find that the requirement on laser phase noise for coherent optical communications is very stringent, especially when migrating to higher order QAM modulation formats. For example, the QPSK modulation format would requires a phase-error variance in order of $10^{-2}(rad^2)$ to achieve a reasonable theoretical performance, while the 16-QAM modulation format would need much lower phase-error variance σ_ϕ^2, around $10^{-3}(rad^2)$. The Gaussian phase error mainly defines the ultimate BER performance of the coherent systems. In the next few subsections, we will investigate how the sophisticated phase noise processes in SG-DBR lasers would affect the BER performance in such a system.

4.1.2 Experiment setup for the 16-QAM coherent system

The experimental setup is depicted in Fig. 4.3a. The transmitter employed two DFB lasers and one SG-DBR laser with different phase noise characteristics while the receiver local oscillator was a narrow linewidth external cavity laser. The 16-QAM driving signal was generated by an arbitrary waveform generator (AWG) whose outputs were followed by a pair of anti-aliased low-pass filters and amplified to drive the I & Q arms of a dual parallel Mach-Zehnder modulator. The four-level driving signals, shown in the upper inset of Fig. 4.3a, were optimized for the nonlinearity of the electrical amplifiers and the I/Q modulator. The variable optical attenuator (VOA) adjusts the received power into the low-noise EDFA that served as the pre-amplifier for the receiver front-end. The EDFA output was further amplified by a second EDFA, with the optical filters (2 nm bandwidth) reducing the ASE noise. The second VOA maintained an input optical power of -14 dBm into the 90^o optical hybrid. The lower inset of Fig. 4.3a shows the optical eye of the 16-QAM signal. The polarization of the received optical field was manually adjusted to match with the polarization of the LO optical field whose power was kept at $+3$ dBm.

A pair of balanced photo-detectors detected the output signals from the optical hybrid. An Agilent real-time scope captured the detector output signals at 40 GSa/s, and they were then fed into a computer for off-line DSP processing, as illustrated in Fig. 4.3b. The digital samples were firstly normalized by their rms values and the I/Q components were balanced. The non-data-aided frequency correction removed the frequency offset between the lasers [12] and a 20-symbols training sequence was employed to achieve symbol synchronization. Many algorithms have been developed for carrier phase recovery in digital coherent receiver including the least mean-squared (LMS) algorithm [13]. In this work, we developed a simple first order decision-directed Phase-Locked Loop (DD-PLL) as shown by the block diagram in Fig. 4.3c. The residual carrier phase, $\phi_e(n)$, of the n^{th} symbol was estimated by subtracting the phase of the detected symbol, $\phi_d(n)$, from the total phase $\phi(n)$ determined by removing from the received signal the estimated carrier phase, $\phi_{acc}(n)$, that has been accumulated from $\phi_e(n)$. The accumulation coefficient k_p adjusts the convergence speed of the algorithm. The performance of the first order DD-PLL was verified against the LMS algorithm and showed a slight improvement; primarily because the LMS algorithm is subjected to both amplitude and phase corrections. As a result, we employed the first order DD-PLL as the referenced scheme to evaluate the system performance with the DFB and SG-DBR lasers. Gray coding was also employed for symbol encoding and decoding.

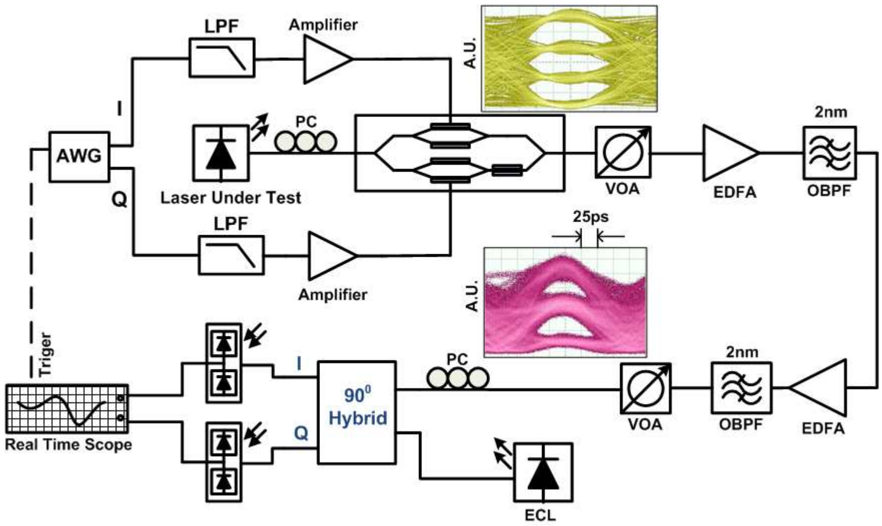

(a) Experimental setup

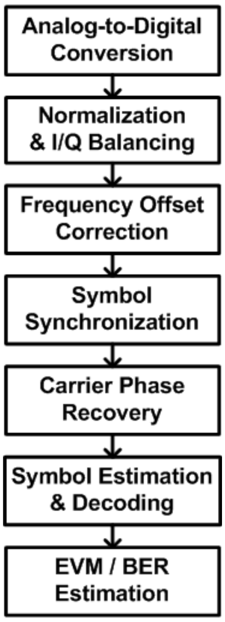

(b) DSP offline

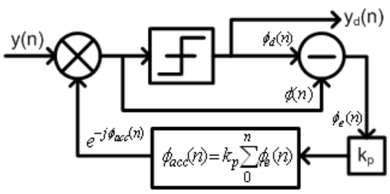

(c) First order decision-directed Phase Lock Loop

Figure 4.3: Experiment setup for coherent communication system employing 16-QAM modulation format at 5 Gbaud

4.1.3 System performance evaluation for 16-QAM modulation format

4.1.3.1 Phase Noise Characteristics

We firstly characterize the phase noise of the lasers using the DSH-PM method with a 12 km fiber delay line that has been previously described in chapter 3. As shown in Fig. 4.4, the measurement results for the two different DFB lasers demonstrate the purely random walk in phase, or white FM noise, characteristics [4, 5] at 300 kHz and 6 MHz linewidths. The SG-DBR laser operated under different bias conditions resulted in different phase noise characteristics. Fig. 4.4c shows that the SG-DBR laser has a high-frequency white FM-noise region above 200 MHz that corresponds to an intrinsic linewidth of 300 kHz. Below 200 MHz, the device exhibits excess *1/f* or flicker FM noise when only the gain section was biased, and $1/f^2$ or random-walk FM noise when the bias was applied to both gain and tuning sections. The excess noise increased the phase-error variances, as shown in Fig. 4.4b, in comparison with the 300 kHz DFB laser, and between the different bias conditions. The broadening of DSH linewidths of the SG-DBR laser to 5.5 MHz and 19.5 MHz due to the excess noise can be observed with the E-field power spectral densities in Fig. 4.4a . Again, the results demonstrate in particular that the SG-DBR laser has $1/f^2$ noise that can be attributed to biasing the passive sections; and therefore would benefit from the use of low-noise current sources.

4.1.3.2 Performance Evaluation

The performance of the 16-QAM coherent system in Fig. 4.3a was evaluated with the above DFB and SG-DBR lasers in the transmitter. We note for the tunable SG-DBR laser that in order to achieve operation on a specific ITU channel, it is normally necessary to bias all sections (gain and tuning) of the device. Fig. 4.5 displays the BER versus received power for the two DFB lasers. The plots verify that the BER improves slightly with the first order DD-PLL, and the system performance is limited by the phase noise of the DFB laser. The inset in Fig. 4.5 depicts the example symbol constellation for the 300 kHz DFB laser at -28 dBm received power ($k_p = 0.15$). The system performance was further analyzed with the time-resolved BER measurements as shown in Fig. 4.6. These measurements were performed by capturing the output signals from the balanced photo-detectors in data blocks of 2 μs long for offline processing. The BER for each of the 2 μs data blocks was then computed (received power at -20 dBm and $k_p = 0.2$). The time-resolved BER plots for the DFB devices again show that

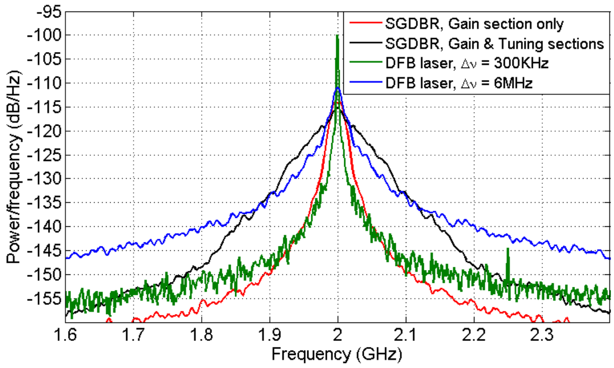

(a) PSD of E-field

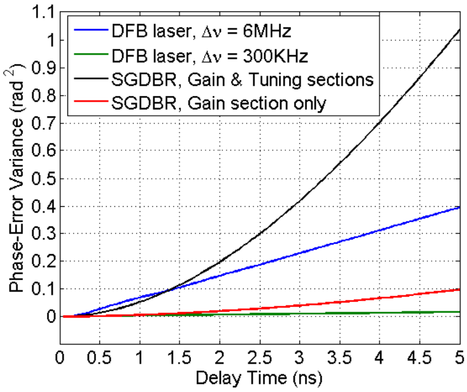

(b) Phase-error variance

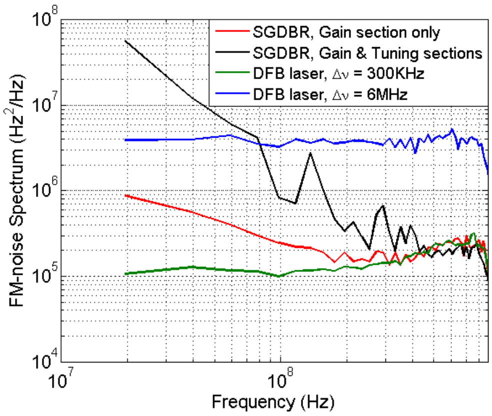

(c) FM noise spectrum

Figure 4.4: Phase noise characteristics of DFB lasers and SG-DBR laser

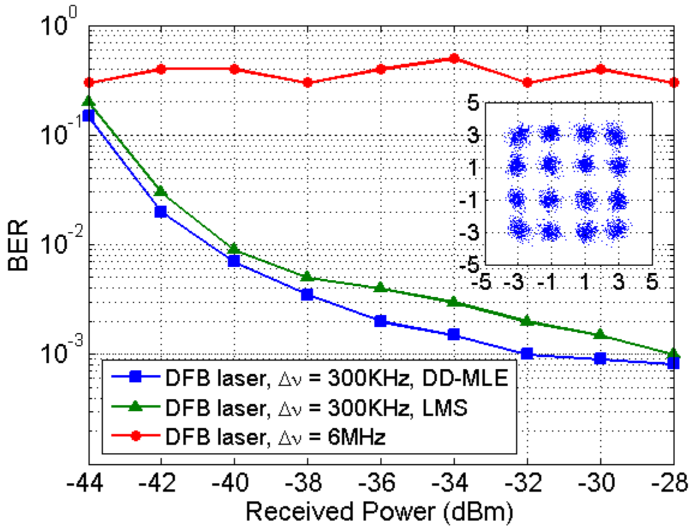

Figure 4.5: Performance of DFB lasers for 16-QAM system at 5 Gbaud

the laser with a 300 kHz linewidth could operate consistently at around 10^{-3} BER (the BER performance limitation is mainly constrained by the laser phase noise), whereas the laser with a 6 MHz linewidth should not be used for the 16-QAM transmitter at 5 Gbaud. The time-resolved BER plots in Fig. 4.6 for the SG-DBR laser show intermittent performance degradation when biasing the gain section only; and the degradation became more prevalent when both the gain and tuning sections were biased. The overall comparison of the results in Fig. 4.6 would suggest that the performance of the SG-DBR laser can achieve that of the narrow linewidth DFB laser. This is consistent with the previous observation that the SG-DBR laser has the intrinsic, white-FM linewidth that is similar to the narrow linewidth DFB laser at 300 kHz. The intermittent degradation worsened subject to the bias conditions, and is consistent with the increase in the phase-error variances in Fig. 4.4b, and in the low-frequency FM noises from $1/f$ to $1/f^2$ in Fig. 4.4c. The time-resolved BER plots also indicate that the SG-DBR laser performance remains largely bounded between the two DFB lasers, even though its DSH linewidth broadening exceeded both and was as much as 19.5 MHz.

Figure 4.7 further illustrates the example time-resolved measurements from Fig. 4.6 at points $t = 12\mu s$ and $18\mu s$ for the SG-DBR laser with only the gain section biased. Figures (4.7a, 4.7b) and (4.7c, 4.7d) display the symbol constellation and the error vector magnitude, respectively. In comparison to Figs. 4.7a and 4.7c, the noisy constellation of Fig. 4.7b corresponds to the sudden increase of the error vector magnitude in Fig. 4.7d from the loss of carrier phase tracking due to the $1/f^{\alpha}$ noise. The low-frequency excess FM noise of the semiconductor laser generally induces a slow fluctuation of the instantaneous

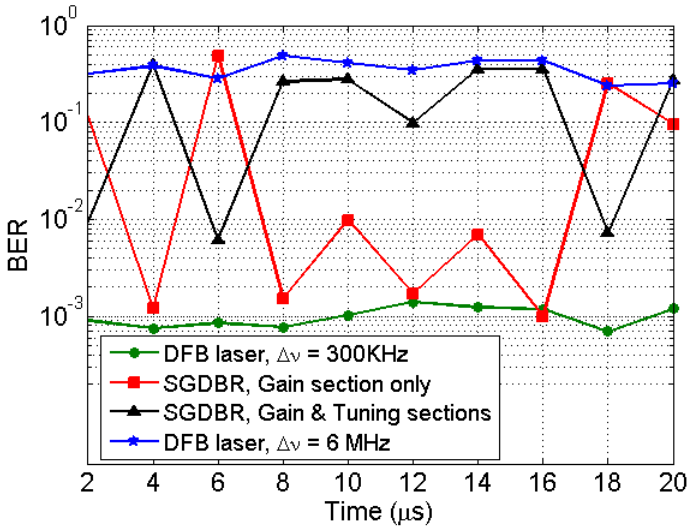

Figure 4.6: Time-resolved BER of 16-QAM system with $2-\mu s$ long data blocks

carrier frequency [5], and the effect of this random frequency drift for the SG-DBR laser can be observed by comparing the symbol constellations in Figs. 4.7a and 4.7b and note that the entire constellation has also been slightly rotated. To overcome the problems caused by the excess noise in these coherent systems, there are a couple of solutions: (i) use low noise current sources with low-pass filters to reduce the noise from the biasing circuits, and (ii) develop improved carrier phase recovery algorithms that would achieve better phase tracking under large excess phase noise. For example, instead of the first-order DD-PLL in this work, a second-order DD-PLL may be employed for tracking both the phase and frequency drifts, together with more frequent symbol re-timings along the data blocks. In the next subsection, we will investigate the tracking performance of a second order DD-PLL in overcoming the severe impact of the $1/f^{\alpha}$ noise in SG-DBR lasers.

To recap, in this section, we have examined the performance of an SG-DBR laser in a coherent optical communication system employing high order modulation formats. The performance is significantly reduced due to excess FM-noise. We confirmed that while the white FM-noise has been determined to largely define the overall system performance, the system operation could potentially be impaired by excess laser phase noise. The experimental results show the importance of distinguishing different phase noise processes of laser sources and developing the means to cope with excess noise of SG-DBR lasers in future WDM systems that employ high order modulation formats.

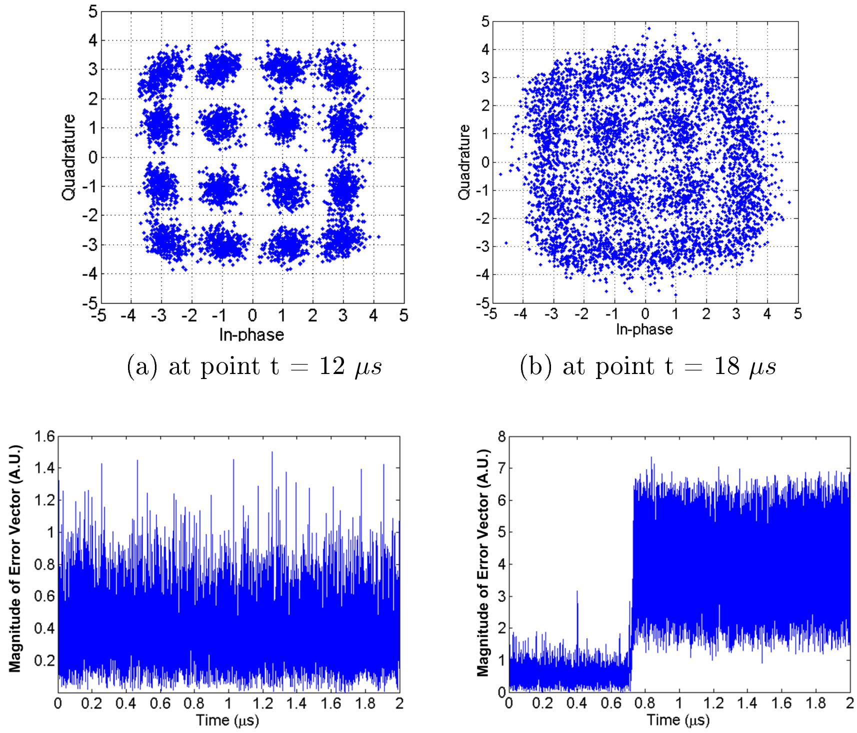

(a) at point t = 12 μs (b) at point t = 18 μs

(c) at point t = 12 μs (d) at point t = 18 μs

Figure 4.7: Constellations (a,b) and error vector magnitudes (c,d) at sample points from Fig. 4.6 for the SG-DBR laser with only gain section biased

4.1.4 Phase tracking with second order Phase-Locked Loop

As the results in the preceding subsection demonstrate, while the white-FM noise determines the ultimate performance of coherent systems, the excess noise in SG-DBR laser could significantly degrade the system performance for higher order QAM such as 16-QAM. The use of SG-DBR lasers in coherent communications systems would necessitate receiver Digital Signal Processing (DSP) to cope with such excess laser phase noise. In this subsection, we investigate a second order decision-directed Phase-Locked Loop scheme that tracks the white-FM noise and the excess noise of a SG-DBR laser. The performance of the proposed tracking scheme will be experimentally examined with 16-QAM at 16 Gbaud and compared with the current phase tracking techniques.

4.1.4.1 Experiment setup

The experiment in this section had been performed in Center of Optics, Photonics and Lasers, Laval University, Canada. Therefore the experiment setup has some changes compared with the experiment in Fig. 4.3. Figure 4.8 shows the experimental setup with the transmitter's SG-DBR laser operating under different

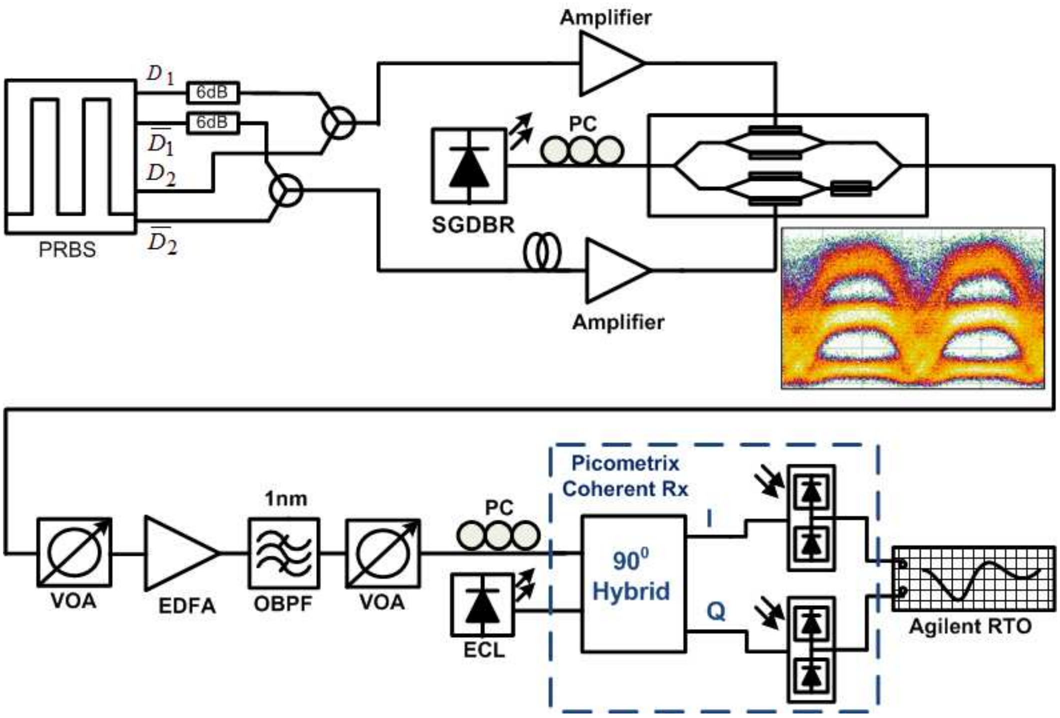

Figure 4.8: Experimental setup for 16-QAM at 16 Gbaud with SG-DBR laser at transmitter

biasing conditions resulting in different phase noise characteristics. The four-level driving signals for the I & Q channels of the 16-QAM signal were generated by combining the PRBS $2^7 - 1$ and PRBS $2^9 - 1$ bit-streams from the pattern generator. The Q channel was de-correlated from the I channel with a fixed delay line. The variable optical attenuator adjusts the received power into the EDFA so that the OSNR could be varied at the receiver front-end. The EDFA output was followed by an optical filter with a 1 nm bandwidth to reduce the ASE noise. The second VOA maintained an input optical power of +0 dBm into the Picometrix coherent receiver that employed a narrow linewidth external cavity laser for the local oscillator. The polarization of the received optical field was manually adjusted to match with the polarization of the LO optical field whose power was kept at +10 dBm. The inset in Fig. 4.8 shows an example of the received eye at the front end of the coherent receiver at 40 dB OSNR.

An Agilent real-time scope captured the detector output signals at 80 GSa/s, and they were then fed into a computer for off-line DSP processing. The data block length was 200K samples and five consecutive blocks were captured and processed which yields 10^6 samples for each BER calculation. Many algorithms have been developed for carrier phase recovery in digital coherent receivers including decision-aided maximum likelihood (DA-ML) phase estimation [14], blind phase search technique (BPS) [15], and first order decision-directed phase-locked loop

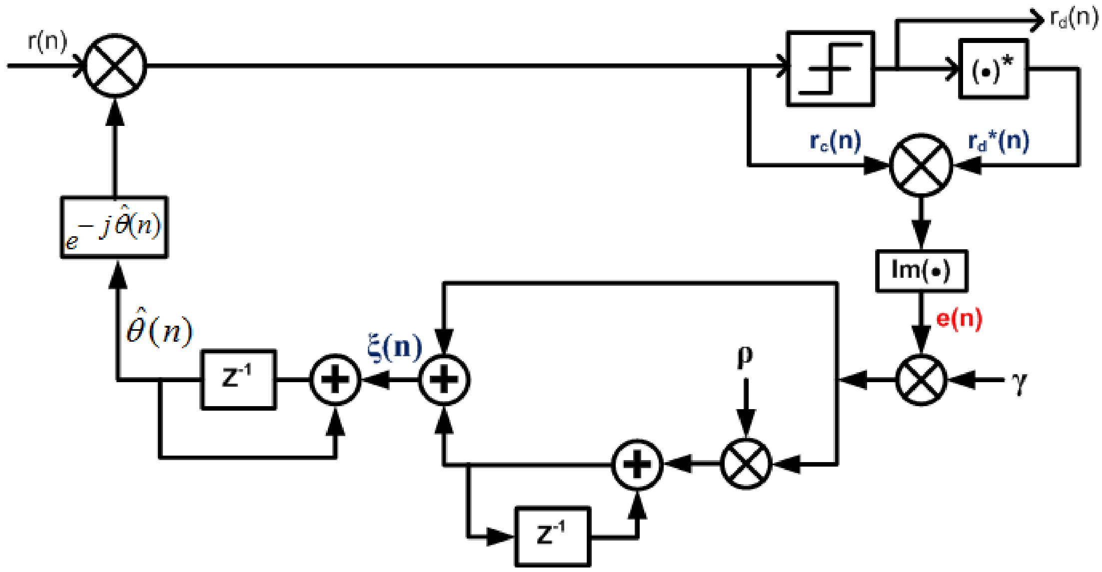

Figure 4.9: Second order decision-directed Phase-Locked Loop.

[16, 17]. However, in the particular case of a SG-DBR laser having the unique phase noise characteristics that include both white FM noise and very high excess frequency noise, there is a need for a tracking scheme that can be effective against these two different types of phase noise, as current carrier phase tracking schemes cannot handle them. In this subsection, we developed a second-order DD-PLL [17] to address this issue. Figure 4.9 shows the block diagram of the proposed carrier phase tracking scheme parameterized by γ and ρ with the recovered symbols decoded into bit streams for BER counting. The coefficient ρ controls the speed of convergence of the first loop which yields output $\xi(n)$ corresponding to the frequency fluctuation from the laser, while γ will be used to optimize the overall performance of the second order PLL. The two feedback coefficients were numerically optimized in offline DSP to maximize BER performance.

4.1.4.2 Performance evaluation

Again, we operate the SG-DBR laser at two different biasing points: biasing only the gain section at $I_{Gain} = 120mA$ yields the lowest phase noise at 1548.70 nm wavelength, and biasing four sections simultaneously with driving currents $I_{Front} = 1mA$, $I_{Gain} = 120mA$, $I_{Back} = 0.72mA$ and $I_{Phase} = 8.7mA$ yields much higher phase noise at an operating wavelength of 1553.66 nm. As discussed in previous sections, biasing the additional passive sections will significantly increase the excess $1/f^{\alpha}$ noise of the monolithic tunable lasers.

The SG-DBR laser with the phase noise characteristics determined from the above biasing points was incorporated into the coherent 16-QAM system oper-

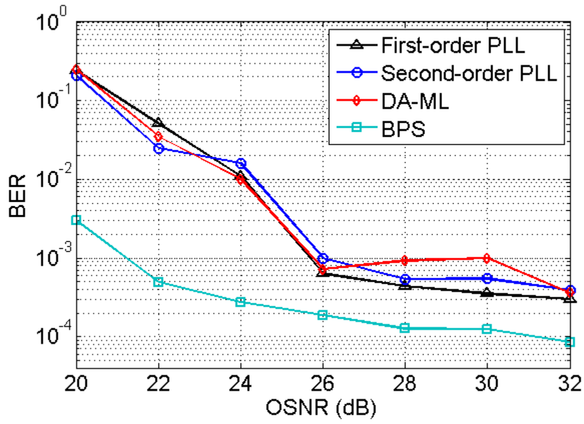

(a) Biasing gain section only

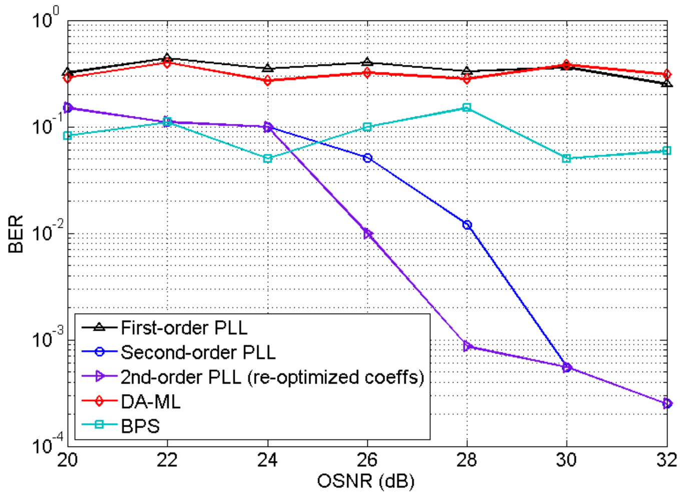

(b) Biasing all sections

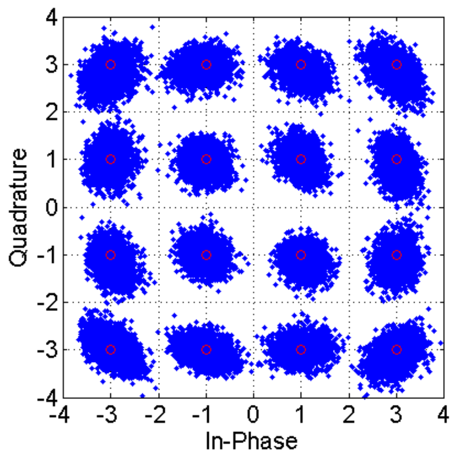

(c) Constellation at OSNR = 32dB

Figure 4.10: BER versus OSNR for 16-QAM at 16 Gbaud when biasing gain section only (a), biasing all sections (b), and example of recovered symbol constellation at $OSNR = 32dB$ using second-order PLL when biasing all sections simultaneously (c)

ating at 16 Gbaud line rate in Fig. 4.8. We investigated the effectiveness of the second-order DD-PLL scheme in tracking the excess phase/frequency noise and also compared the performance of the proposed scheme with the first-order PLL, DA-ML and BPS phase tracking algorithms. Figure 4.10a shows the BER performance when biasing the gain section only which yields the lowest phase noise for the SG-DBR laser. The results demonstrate that all of the phase tracking techniques were effective, with the BPS algorithm [15], when set at the optimized filter half-width N = 7 and B = 32 test phase angles, achieving the best performance. The DA-ML [14] (optimized block length L = 5), and first-order PLL [16] (optimized feedback coefficient $\mu = 0.03$) show a similar performance with about 4 dB penalty at 10^{-3} BER compared to BPS. The proposed second-order PLL with optimized feedback coefficients $\gamma = 0.025$ and $\rho = 0.05$ yields the same performance as first-order PLL and DA-ML in this case. The error floors of all tracking schemes were mainly defined by the white-FM noise of the SG-DBR laser which is much higher than that of the ECL as the LO [16].

Figure 4.10b compares the BER performance of the tracking schemes when all the sections were biased, resulting in the large excess $1/f^{\alpha}$ noise. The BER plots demonstrate clearly the robustness of the second-order PLL scheme as it continued to be effective in the presence of both white-FM noise and large excess noise, while the other well-known phase tracking schemes failed. We can observe from Fig. 4.10b that only the proposed scheme was able to reach the FEC level of 10^{-3} BER at less than 30 dB OSNR when the coefficients γ and ρ were kept at previous values (biasing gain section only), and an improved BER performance with smaller penalties can be achieved when the feedback coefficients were re-optimized (to minimize the BER) at OSNR of 26 dB and 28 dB. Fig. 4.10c depicts the example recovered symbol constellation at OSNR = 32 dB. Even though the second-order PLL has about 2 dB in performance penalty when comparing the results in Fig. 4.10a and Fig. 4.10b, we conclude that only the proposed scheme has the ability to overcome the effect of the complicated and large excess phase noise that has been observed in coherent systems employing monolithic tunable lasers. We also note that as the feedback coefficients of the PLL can be re-adjusted for better performance, in practice a training sequence could be transmitted to optimize the feedback coefficients of the second-order PLL at each operation condition.

In summary, we have examined the performance of a second-order DD-PLL phase tracking technique in a coherent receiver when a tunable SG-DBR laser was used for transmission. The proposed scheme demonstrated its robustness in tracking white-FM noise and large excess noise for 16-QAM at 16 Gbaud.

The experimental results present the ability to employ monolithic tunable lasers for higher order modulation formats with coherent systems. This is achieved by exploiting advanced digital signal processing at the receiver side to mitigate the need for complex devices with low phase noise.

4.1.5 Effect on cycle slips in QPSK modulation format

Even though QPSK modulation format provides higher tolerance for the excess bit errors caused by the excess frequency noise of SG-DBR laser [16], this low frequency noise will potentially increase the cycle slip probability (CSP) of the phase tracking algorithm. The use of SG-DBR lasers in coherent communications systems therefore necessitates a detailed investigation of cycle slip (CS) enhancement due to this $1/f^{\alpha}$ noise. In this subsection, we experimentally evaluate the BER and CSP performance of SG-DBR lasers with two widely used phase tracking techniques employing both feedback and feed-forward schemes. The experiments with 10.7 Gbaud QPSK have been carried out to investigate the effects of low frequency FM-noise in SG-DBR lasers on the CSP. A new phase tracking - CS detection/correction technique is also proposed to reduce the computational complexity which would enable practical pilot-aided CS detection/correction for high-speed optical coherent communications.

4.1.5.1 Experiment setup

Essentially, the experiment set up is similar with the setup in previous sections except for some slight changes described here. Figure 4.11 shows the experimental setup with the transmitter's SG-DBR laser operating under different biasing conditions resulting in different phase noise characteristics. A narrow linewidth DFB laser was also employed at the transmitter for comparison. Figure 4.12a depicts the FM-noise spectrum of the DFB laser and the SG-DBR laser again at different operating points which will be deployed for the system experiments. The driving signals for the I & Q channels of the QPSK signal were generated by the PRBS bit streams from the pattern generator. The Q channel was de-correlated from the I channel with a fixed delay line. The second EDFA-optical filter-VOA stage of the pre-amplified receiver maintained an input optical power of -3 dBm into the coherent receiver that employed an external cavity laser for the local oscillator. The polarization of the received optical field was manually adjusted to match with the polarization of the LO optical field whose power was kept at +10 dBm.

A real-time scope captured the detector output signals at 50 GSa/s, and

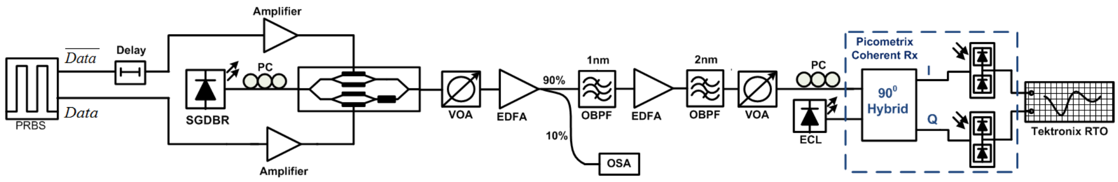

Figure 4.11: Experimental setup for QPSK at 10.7 Gbaud with SG-DBR laser at transmitter

they were then fed into a computer for off-line DSP processing, as illustrated in Fig. 4.12b. The data trunk was 2.5M samples and four consecutive trunks were captured and processed which yields more than 2×10^6 symbols for BER and CSP estimation. The digital samples were firstly normalized by their root-mean-square values and the I/Q components were balanced. The received signal was then re-timed and re-sampled to the symbol stream for frequency offset compensation. In this section, we investigate the performance of two widely employed carrier phase tracking methods: a feedback scheme with first-order decision-directed PLL as in the previous section, and a feed-forward scheme with the Viterbi & Viterbi algorithm (V&V) [19, 20, 21]. That was followed by the CS detection/correction as presented in Fig. 4.12b. Differential decoding could be performed at this stage instead of CS correction to compare with the pilot-assisted CS correction schemes. The recovered symbols were subsequently decoded for BER calculation.

4.1.5.2 Cycle slip detection/correction

The CS in QPSK modulation format caused by the phase tracking algorithms leads to catastrophic errors due to the ambiguity in the symbol quadrant. By using periodical pilot symbols, we can detect the CS event and subsequently correct for that error in the estimated phase. The received data is processed in blocks of symbols with 3% pilot symbols. As illustrated in Fig. 4.12b, with the aid of pilot symbols, the symbols block which contained a CS event will be detected. To further identify the exact position of the symbol where the CS event happened within that block, we employ one of the two approaches described below (note that either PLL or V&V algorithm can be used as the phase tracking technique prior to CS detection/correction).

In the first approach of CS detection (CS1) adopted from [19], we deploy additional backward phase tracking within the block that contains the CS, then the minimum point of phase difference between the forward and backward phase estimates will present the position of the CS symbol. This approach poses a high computational requirement due to the additional backward phase searching, especially in the case of SG-DBR lasers where the very high $1/f^{\alpha}$ noise would

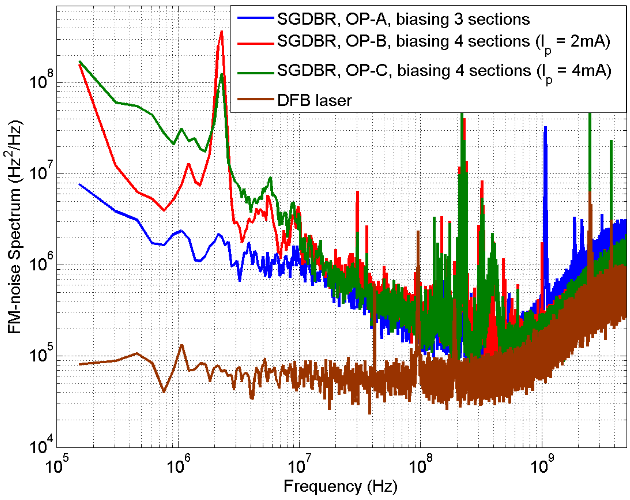

(a)

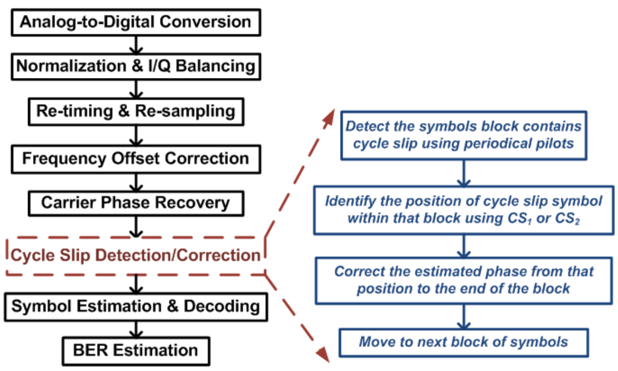

(b)

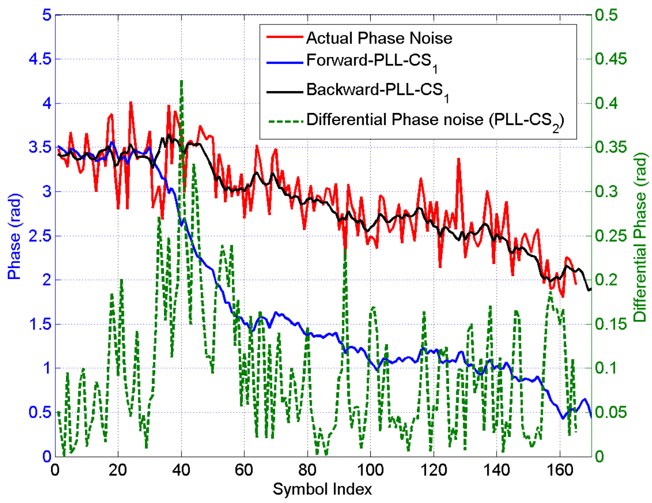

(c)

Figure 4.12: (a) FM-noise spectrum of DFB laser and SGDBR laser at different operating conditions, (b) DSP-offline at receiver. (c) Example of experimental phase estimation using different CS detection/correction methods.

result in increasing CSP after phase tracking. We also propose a second approach for CS detection (CS2) to significantly speed up the processing. In this approach the carrier phase estimate $\theta_e(n)$ from the phase tracking algorithms within the block will be delayed by τ_n, and subtracted from the original estimate to find the *absolute differential phase estimate* $\delta\theta_e(n) = |\theta_e(n) - \theta_e(n - \tau_n)|$. The position of the CS symbol will then coincide with the maximum of the absolute differential phase estimate. By only employing delay and subtract operations on the estimated phase, this CS2 technique significantly reduces the computational complexity compared with the CS1 technique (by avoiding backward phase searching) while achieving similar performance.

An example of phase noise estimation from the experimental results in Fig. 4.12c clearly illustrates the two CS detection approaches. In the CS1 method, the forward phase estimate (using PLL in this example) is represented by the blue solid curve. The CS causes the phase estimate to deviate from the actual phase noise (red curve) by $-\pi/2$. The minimum difference of this forward phase estimate with the backward phase estimate (black curve) presents the position of the CS symbol as discussed in [19]. With the CS2 approach, the green dashed curve depicts the absolute differential phase estimate. The position of the maximum of this curve corresponds to the position of the CS symbol which yields the same result with the CS1 approach. After the CS symbol is identified, the phase estimate from that position to the end of the symbols block will be corrected according to the phase estimate deviation.

Figure 4.13a shows the comparison of the different phase noise tracking schemes in combination with different CS detection approaches, using the experimental setup presented in Fig. 4.11. The BER (left axis) and CSP (right axis) at an OSNR = 8dB have been plotted versus the appropriate control parameters of the phase tracking techniques such as convergence coefficient - μ of PLL (bottom axis), or the length of the moving average filter of V&V algorithm [19, 20, 21] (top axis). These parameters need to be optimized for different levels of laser phase noise, especially white-FM noise. In fig. 4.13a, an SG-DBR laser with all 4 sections biased was employed at the transmitter. The optimum BER (employing the appropriate control parameters) of PLL-CS1, PLL-CS2, and V&V-CS2 are shown in blue, brown, and black colours respectively, and are all similar (about 10^{-3}). While the minimum CSP of V&V-CS2 and PLL-CS1 (or CS2) in purple and red colours are also similar (2×10^{-6}). The results show that, for QPSK with SG-DBR transmitter, PLL or V&V algorithms in combination with one of the two CS correction methods would yield similar performance in terms of BER and CSP.

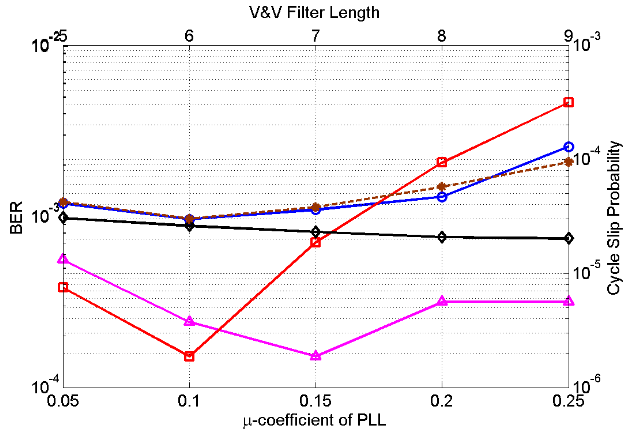

(a)

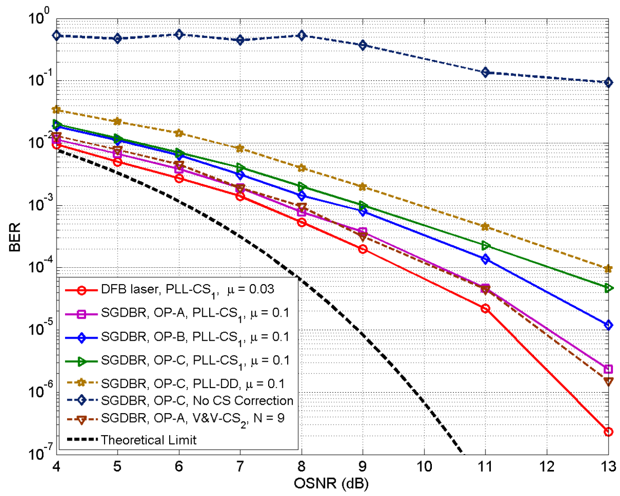

(b)

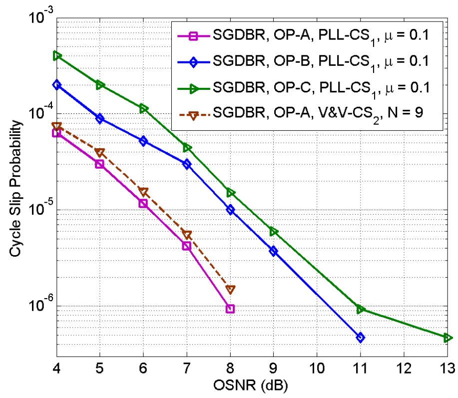

(c)

Figure 4.13: (a) Performance of different phase tracking – cycle slip correction schemes versus their control parameters (OSNR = 8dB): BER of V&V–CS2 (black), BER of PLL–CS1 (blue), BER of PLL–CS2 (dash-brown); and CSP of V&V–CS2 (purple), CSP of PLL–CS1 (exactly coincide with CSP of PLL-CS2, in red color); (b) BER versus OSNR and (c) CSP performance of SGDBR in 10.7 Gbaud QPSK system.

4.1.5.3 Cycle slip probability evaluation

To investigate the CS effect with a SG-DBR laser, we bias the laser at different conditions. The Gain section current was kept constant at $I_{Gain} = 100mA$ throughout the work. For the operating point A (OP-A, $\lambda = 1559.065nm$), we additionally bias the two tuning sections: $I_{Front} = 10mA$, $I_{Back} = 5mA(I_{Phase}$: OFF). We then further increase the low frequency noise of the laser within this supermode by subsequently increasing the injected current to the phase section such that $I_{Phase} = 2mA$ (operating point B, OP-B, $\lambda = 1558.961nm$), and then $I_{Phase} = 4mA$ (operating point C, OP-C, $\lambda = 1559.174nm$). The three operating points demonstrate similar levels of white-FM noise as shown in Fig. 4.12a while the $1/f^{\alpha}$ noise was significantly increased when the total injected current into the passive section was increased as mentioned in previous sections.

We then employ the SG-DBR laser and the narrow linewidth DFB laser ($\lambda = 1558.984nm$) at the transmitter of the 10.7 Gbaud QPSK system presented in Fig. 4.11 to evaluate the BER and CSP performance. The measured performance versus OSNR of the SG-DBR laser and DFB laser are shown in Fig. 4.13b and 4.13c. The figures confirm the equivalence in performance of PLL-CS1 and V&V-CS2 as discussed above. The BER performance of the SG-DBR laser in Fig. 4.13b is slightly degraded when the low frequency noise is enhanced at operating points OP-B and OP-C. Figure 4.13c clearly shows that low frequency noise considerably increases the CSP in coherent systems employing SG-DBR lasers (no CS has been found for the DFB laser case). A penalty of 2 dB OSNR in term of cycle slip probability can be observed in Fig. 4.13c between biasing 3 sections (OP-A) and 4 sections (OP-B, OP-C) of the SG-DBR laser. In Fig. 4.13b, we also turn off CS correction, or perform differential decoding (PLL-DD) instead of CS correction using pilot symbols for comparison. An OSNR penalty of about 1 dB, at a BER of 10^{-4}, is incurred due to the nature of error duplication in the differential decoding scheme [19]. Also with no CS correction or differential decoding, the system could not operate at this very high level of phase/frequency noise as illustrated in Fig. 4.13b. The experimental results in Fig. 4.13 show that the $1/f^{\alpha}$ noise in monolithic tunable lasers would yield an increase in CSP of the well-known phase tracking algorithms and in turn requires an efficient CS detection/correction technique to cope with this issue.

To recap, in this subsection, we have examined the cycle slip effects of a SG-DBR laser in a 10.7 Gbaud QPSK transmission system with well-known phase noise tracking algorithms. A new CS detection/correction method has also been developed with reduced complexity over conventional techniques. The additional low frequency noise of the tunable laser caused by carrier dynamics in the passive sections leads to an increase in CSP after carrier phase tracking. This will in turn require either hardware implementation to reduce the low frequency noise of the SG-DBR laser, or efficient DSP at the receiver to improve the system performance.

4.2 A novel coherent Self-Heterodyne receiver based on phase modulation detection

In fully coherent optical communications, the state-of-the-art optical coherent receiver employs a 90^o hybrid front end and a local oscillator laser for intradyne demodulation as discussed previously [7, 8]. The integration of the optical 90^o hybrid remains a technical challenge and the laser phase noise requirements on the LO can be difficult to achieve especially with high line rates. Differential modulation techniques such as DQPSK that employs self-homodyne direct detection using delay line interferometers (DLIs) [22, 23] could potentially reduce the requirements on the laser linewidth. However, the DLI approach would require significantly more complex hardware implementation to migrate to higher order modulation formats such as differential m-PSK and differential m-QAM. The authors in [24] also reported a realization of direct-detection multilevel transmission for 16-QAM incorporating with phase pre-integration and advanced digital signal processing.

In this section, we propose a novel coherent receiver scheme based on the phase modulation (PM) detection method [25] that can recover the differential E-field from the harmonics of the modulating carrier without a LO. In previous chapter, we employed PM detection method for characterizing the laser phase noise [4]. Similar approaches to harmonic demodulations have been employed in near-field scanning optical microscopy [26] and Fourier-domain optical coherence tomography [27], but to our knowledge this is the first demonstration in coherent optical communications. We demonstrate experimentally a self-coherent DQPSK system operating at 10 Gb/s by implementing a PM detection method at the receiver. The performance of the proposed technique is compared with other widely employed DQPSK receiver structures through simulations and experimental results. The proposed receiver configuration provides a cost effective solution for the front-end of optical coherent receivers, and has the potential of migrating to higher order modulation formats without significant additional complexity.

4.2.1 Analytical model

In the following we develop the analytical model for the proposed receiver scheme in Fig. 4.14a. The E-field of the modulated optical output from an IQ modulator can be expressed in complex notation (for brevity we have omitted the laser phase and intensity noises) as

$$E(t) = \sqrt{P}a(t)e^{j\phi(t)}e^{j\omega_0 t} \tag{4.4}$$

where ω_0 is the angular optical frequency, P is the optical output power of the laser, and $\phi(t)$ and $a(t)$ respectively are the symbol phase modulation and the normalized symbol amplitude modulation. $a(t)$ is constant for PSK modulation format. The upper arm of the interferometer in Fig. 4.14a has a one-symbol delay and the lower arm is phase modulated by a sine wave. The incident E-field falling on the photo-detector can be written as

$$E_i(t) = \frac{1}{2}\left[E(t-T_s) - E(t) \times e^{j[b\sin(\omega_c t + \phi_c)]}\right] \tag{4.5}$$

where T_s is the symbol duration. The input signal to the phase modulator is $b\sin(\omega_c t + \phi_c)$, where b is the PM index, ω_c and ϕ_c are the angular frequency and phase of the modulating carrier, respectively. The output current of the photo-detector with responsivity $\mathcal{R}$ is proportional to the intensity of the slowly varying envelope of the incident field (or the lowpass component of the crossing term):

$$\begin{aligned} i(t) &= \mathcal{R} \times E_i(t)E_i^*(t) \\ &= \frac{1}{4} \times \mathcal{R}\{a^2(t) + a^2(t-T_s) \\ &\quad -2a(t)a(t-T_s)\cos\left[\omega_0 T_s + \phi(t) - \phi(t-T_s) + b\sin(\omega_c t + \phi_c)\right]\} \end{aligned} \tag{4.6}$$

Ignoring the first two terms in equation 4.6 (which are constant for PSK and can be canceled using balanced photo-detectors, or a single photo-detector with a DC-block) and expanding the third term:

$$\begin{aligned} i(t) &= -\frac{1}{2} \times \mathcal{R}Pa(t)a(t-T_s)\cos\left[\omega_0 T_s + \phi(t) - \phi(t-T_s) + b\sin(\omega_c t + \phi_c)\right] \\ i(t) &= -\frac{\mathcal{R}P}{2}a(t)a(t-T_s) \times \{\cos\left[\omega_0 T_s + \phi(t) - \phi(t-T_s)\right]\cos\left[b\sin(\omega_c t + \phi_c)\right] \\ &\quad - \sin\left[\omega_0 T_s + \phi(t) - \phi(t-T_s)\right]\sin\left[b\sin(\omega_c t + \phi_c)\right]\} \end{aligned} \tag{4.7}$$

Using the Bessel coefficient expansions in the same manner with previous section, it is clear from equation 4.7 that the I and Q components of the complex differential optical modulation envelope, $a(t)a(t-T_s)e^{j[\phi(t)-\phi(t-T_s)]}$, can be found at the even and odd harmonics of $i(t)$. For bandwidth efficient demodulation,

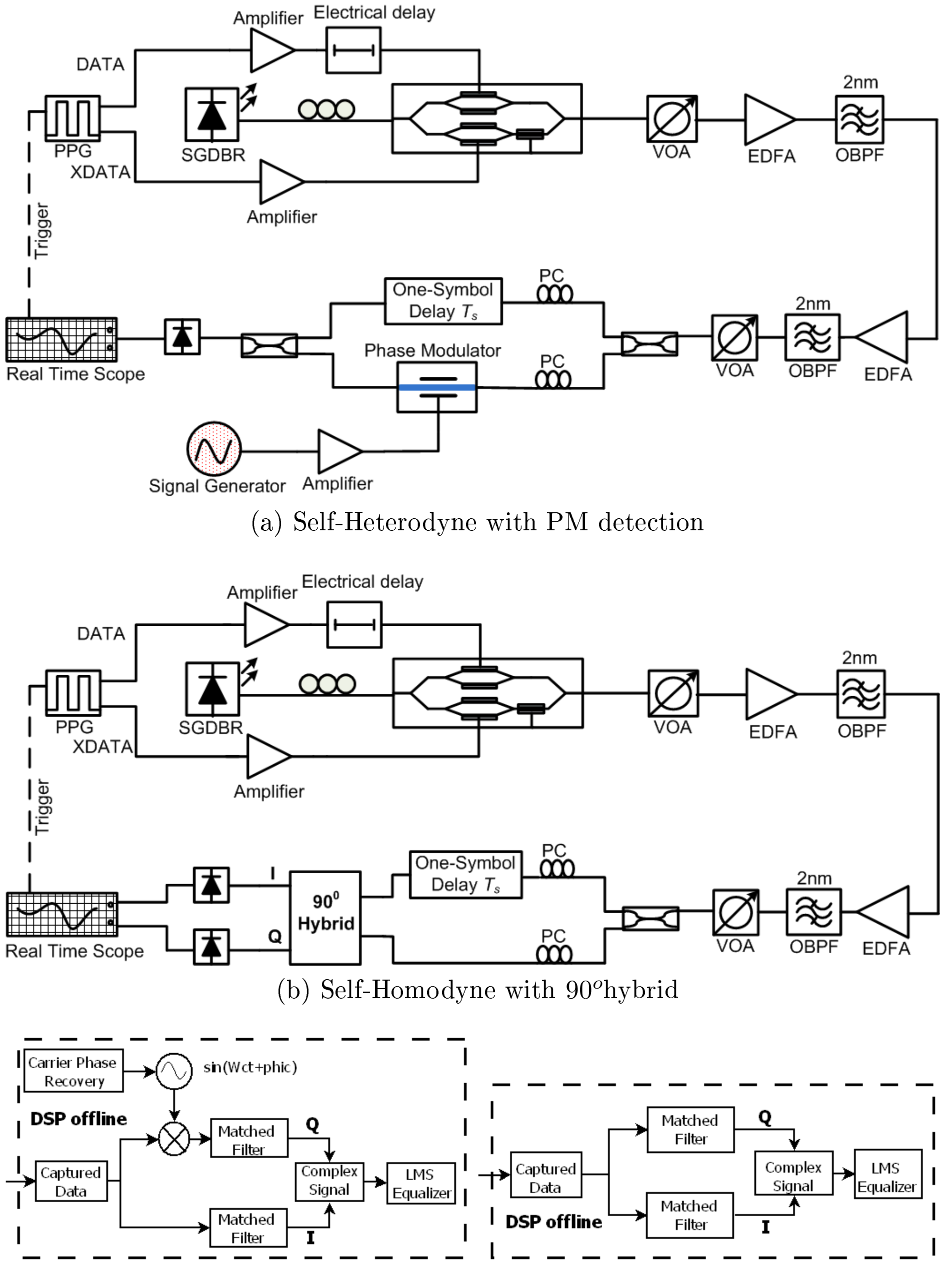

(a) Self-Heterodyne with PM detection

(b) Self-Homodyne with 90^ohybrid

(c) DSP for PM detection technique

(d) DSP for Self-Homodyne technique

Figure 4.14: Experiment setup for proposed differential self-coherent systems

we use specifically the baseband and the first harmonic for the I&Q components. The output current of the photo-detector in term of baseband and first harmonic could be expressed:

$$i(t) = \frac{1}{2}\mathcal{R}P\left[-\mathcal{J}_0(b)I(t) + 2\mathcal{J}_1(b)Q(t)\sin(\omega_c t + \phi_c)\right] \tag{4.8}$$

Where $I(t) = a(t)a(t-T_s)\cos\left[\phi(t) - \phi(t-T_s) + \omega_0 T_s\right]$ and $Q(t) = a(t)a(t-T_s)\sin\left[\phi(t) - \phi(t-T_s) + \omega_0 T_s\right]$. Figure 4.14c shows the block diagram of the off-line DSP for the captured photo-detector current. A simple carrier phase recovery algorithm for ϕ_c was applied prior to demodulation. The least mean-square (LMS) algorithm compensates for the differential drift in the interferometer arms due to the random fluctuation, for example, in temperature. For balanced I/Q outputs the PM index b is adjusted so that $\mathcal{J}_0(b) = 2\mathcal{J}_1(b) \approx 0.81$, or $b \approx 0.90$, as verified on the electrical spectrum analyzer.

4.2.2 Experimental setup

Figure 4.14a shows the experimental setup for a back-to-back 5 Gbaud DQPSK link using coherent PM detection method. The transmitter employed an SG-DBR laser that has a linewidth of 5 MHz at 1547.6 nm when biasing only the gain section at 100 mA. The I & Q arms of a dual parallel Mach-Zehnder modulator (biased close to the null points) was driven at 5 Gb/s by the complementary PRBS outputs of an Anritsu pulsed pattern generator which were de-correlated by 59 bits using an electrical delay. The received power of the DQPSK signal was monitored after the first variable optical attenuator. The first low noise EDFA served as the pre-amplifier for the receiver front-end. The output signal was further amplified by a second EDFA. Each EDFA was followed by 2 nm optical filters to reduce the ASE noise, and the second VOA adjusted the optical power falling on the photo-detector.

The one-symbol delay in one arm of the interferometer was set to $T_s = 200ps$ at 5 Gbauds. The EOspace phase modulator in the other arm was driven by a 5 GHz sinusoidal signal generator. The signal generator output was amplified to provide sufficient drive (modulation index b) to the phase modulator in order to achieve balanced power at baseband and the first harmonic as observed on an RF spectrum analyzer. The light from the delayed and phase modulated arms were recombined via a coupler whose output was detected by an 11 GHz photo-detector with an integrated trans-impedance amplifier. An Agilent real-time scope captured the output signal at 40 GSamples/s that was then fed into a computer for off-line DSP processing as illustrated in Fig. 4.14c. Matched filtering was applied

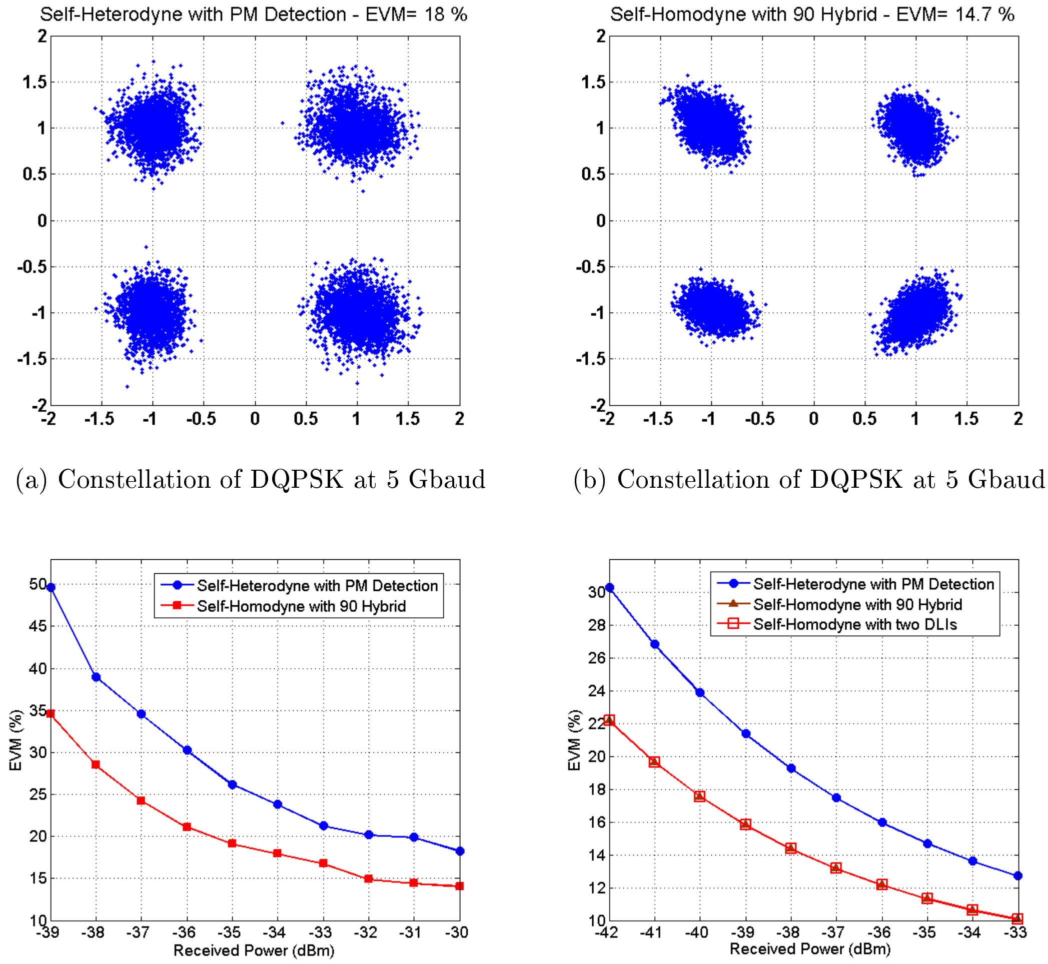

(a) Constellation of DQPSK at 5 Gbaud (b) Constellation of DQPSK at 5 Gbaud

(c) Experimental sensitivity (d) Simulated sensitivity

Figure 4.15: Simulation and experimental results for proposed Differential Self-Coherent scheme with DQPSK at 5 Gbaud

to the baseband I-component and the demodulated Q-component.

In order to evaluate the PM detection technique, we also implemented a self-homodyne, optical coherent receiver [8] as shown in Fig. 4.14b. The offline DSP for Self-Homodyne was also shown in Fig. 4.14d. The two arms of the delay interferometer were now fed into an optical 90^o hybrid whose output light was detected by a pair of 43 Gb/s photo-detectors with integrated TIAs. The I and Q output signals from the photo-detectors were also captured by the Agilent real-time scope at 40 GSamples/s for post-processing.

4.2.3 Simulation & Experimental results

The first VOA in the experimental setup adjusted the back-to-back optical power in order to compare the receiver sensitivity of the PM detection method with the self-homodyne optical receiver. We also performed simulations of both experimental systems in Fig. 4.14, and of a direct detection DQPSK receiver with two DLIs [22, 23], using VPIphotonics software. The results were compared in terms of the error vector magnitudes (EVM).

Figures 4.15a and 4.15b show the example experimental symbol constellations for DQPSK (5Gbaud) at -30 dBm for the self-heterodyne receiver with PM detection and the self-homodyne receiver with 90^o hybrid, respectively. The experimental results show that the recovered DQPSK symbols have an EVM of 18% with PM detection and 14.7% with the 90^o hybrid. Figure 4.15c compares the receiver sensitivity of the two methods. The plots show that PM detection has a power penalty that is about 3 dB at 21% EVM in comparison with standard coherent receiver. The simulation results in Fig. 4.15d are in general agreement with the experimental results and confirmed the sensitivity reduction between PM detection method and self-homodyne receivers. This is only a conceptual simulation with the general models for photo-detector and ASE noise (or Gaussian noise) from EDFAs. The simulation did not use the precise value of the parameters of the components using in the experiment, or account for all types of noise in the experiments. That leads to the discrepancy in the absolute values in Fig. 4.15c (experiments) and Fig. 4.15d (simulation).

The 3dB penalty of PM detection method was primarily caused by the additional ASE beat noise from the EDFAs due to heterodyne demodulation. As in Fig. 4.16, the accumulated number of noise photons after the EDFAs chain was $m(G-1)n_{sp}$ (where n_{sp} is the spontaneous emission factor, m is the number of EDFAs, and G is the amplifier gain) which is much greater than the number of photons from shot-noise (1 photon) [7]. It is clear that the Carrier-to-Noise Ratio γ_s after EDFAs chain was largely defined based on ASE noise (the shot-noise-limit is negligible in such a system [7])

$$\gamma_s = \frac{GN_s}{m(G-1)n_{sp}} \approx \frac{N_s}{mn_{sp}} \tag{4.9}$$

Where N_s is the number of photons per symbol. For self-homodyne, the bandwidth of the received signal was equal to the Baudrate (5GHz) while the bandwidth for Self-Heterodyne with PM detection was twice (10GHz if we used baseband and first harmonic for I&Q) as in Fig. 4.17. Consequently, the in-band ASE noise of self-heterodyne with PM detection was double the in-band ASE noise of self-homodyne. That leads to the 3dB penalty in Receiver Sensitivity of Self-Heterodyne with PM detection comparing with Self-homodyne method.

Although there is a 3dB penalty associated with heterodyne demodulation under ASE-limited condition, the coherent PM detection receiver offers not only the

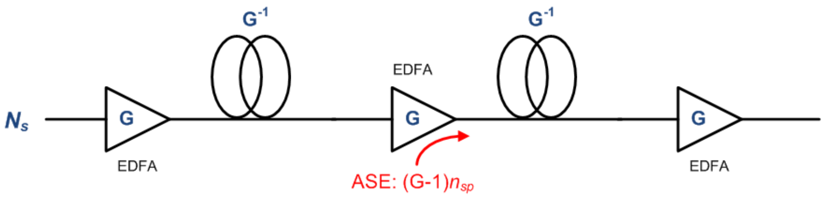

Figure 4.16: Illustration of accumulated ASE in EDFAs chain

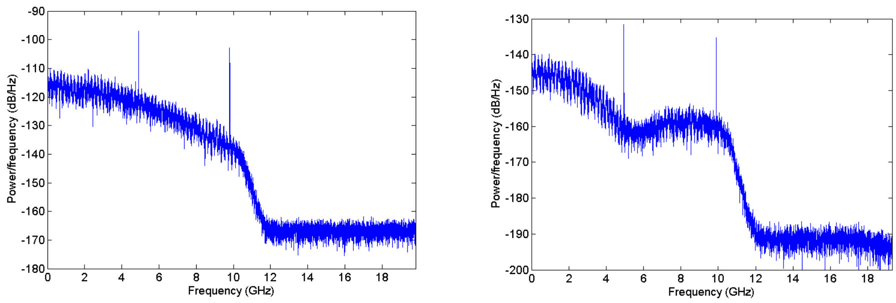

(a) PM Detection method

(b) Self-Homodyne method

Figure 4.17: Examples of Power Spectral Density of received E-field

potential for a low-cost integrated solution but can also significantly simplify the front end of optical coherent receivers. Moreover, this receiver configuration could be feasibly migrated towards higher order modulation formats such as differential m-PSK and differential m-QAM without additional hardware implementation requirements.

The PM detection scheme can be employed in a new coherent receiver as illustrated by the block diagram in Fig. 4.18. The phase-modulated optical local oscillator is combined with the received optical field via the 3 dB coupler. The I and Q components are recovered from the balanced detector output at baseband and demodulated at the carrier frequency, respectively, through matched filters. This configuration provides a trade-off between homodyne detection that uses a 90^o hybrid and two balanced detectors, and heterodyne detection that uses a 3 dB coupler and one balanced detector plus I/Q demodulations at the intermediate frequency [28]. The PM detection receiver thus offers the potential for an integrated solution [29] to homodyne detection and for simplifying the front-end of coherent optical receivers.

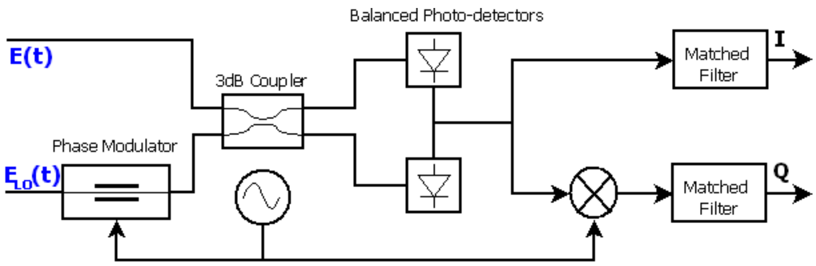

Figure 4.18: The proposed configuration for PM detection coherent receiver

4.3 A novel Baudrate-Pilot-Aided Quadrature Amplitude Modulation transmission scheme

Pilot-aided transmission has been shown to be an efficient method to solve laser phase noise issues [30, 31]. In contrast with the fully optical coherent receiver configuration, a direct detection receiver offers simpler hardware implementation and only requires a single photo-diode (PD) integrated with a trans-impedance amplifier . However the conventional direct detection system can only support amplitude modulation formats as it is unable to fully recover the complex optical field. In this section, we propose a novel pilot-aided transmission scheme with direct detection. With the aid of a pilot-tone added before transmitting data over the optical fiber channel, the scheme is able to cancel the laser phase noise and recover data encoded on the complex optical field (both phase and amplitude), while taking advantage of the simple direct detection receiver. We set the pilot tone frequency at the baudrate and used matched filtering to recover the high-order QAM symbols in the presence of very high levels of laser phase noise. Through analytical model and experimental results, we demonstrate a pilot-aided transmission system that employs different types of lasers, including the SG-DBR laser, and direct detection for 16-QAM at 2.5 Gbaud. We will firstly review the theoretical basis and numerical simulation for the proposed baudrate-pilot-aided transmission scheme. The experimental results will then validate the proposed transmission scheme.

4.3.1 Basic concept

The basic concept of Baudrate-Pilot-Aided QAM transmission involves transmitting a pilot tone that is coherent with the optical carrier in order to provide a phase reference at the receiver. Figure 4.19 illustrates the conceptual spectral representation of the proposed transmission scheme. An optical pilot tone that has identical phase properties with the optical carrier will be added to the QAM modulated data before transmission as in Fig. 4.19a. The generation of the pilot

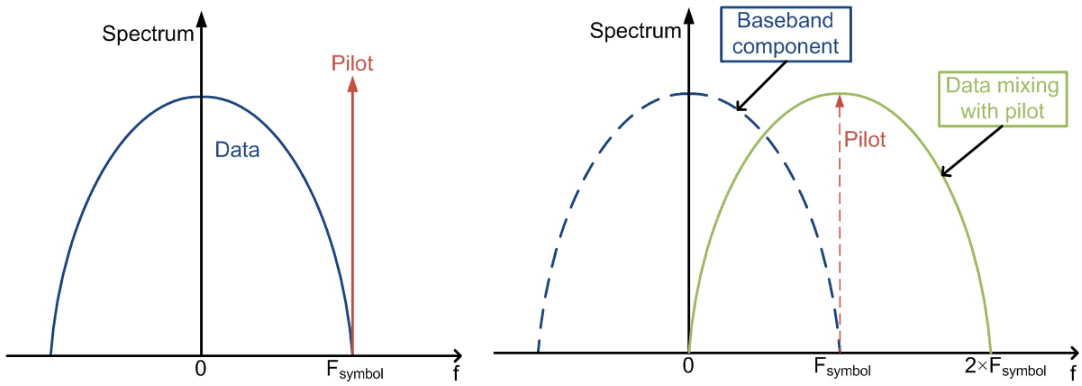

(a) Spectrum of transmitted signal

(b) Spectrum of received signal.

Figure 4.19: Basic concept of Baudrate-Pilot-Aided transmission scheme.

tone can be performed: (i) digitally by a high speed DAC, (ii) optically by means of optical comb generation, (iii) electrically by an oscillator or extracted from system clock of the transmitter.

At the receiver, direct detection of the optically coherent data signal and pilot tone would then cancel the phase/frequency noise of the transmitter laser. The analytical model which will be presented latter explains this interesting characteristics of the proposed scheme. Figure 4.19b depicts the conceptual spectrum of the received signal after a square law detector - the photodiode. The desired data will be "sitting" on the pilot tone due to the mixing term between the pilot and the data on the optical carrier. Intuitively, the pilot tone should be placed far enough from the optical carrier with a "guard band" so that this cross term will not interfere with the base band component shown in Fig. 4.19b. This approach will cost some unused optical bandwidth for the guard band. For spectral efficiency, we propose that the pilot tone frequency is set to coincide with the baudrate, thus eliminating the guard band by placing the tone at the edge of the main lobe of the symbol spectrum. In this case, the optical spectrum of the desired data will significantly overlap the baseband spectral component as in Fig. 4.19b. However, these two terms are orthogonal because the pilot frequency is commensurate with the system baudrate. Consequently, the transmitted data can be recovered by means of matched filters. The analytical model in this section will explain this concept in more detail.

4.3.1.1 Analytical model

The complex baseband signal with pilot tone can be modeled as (for brevity, we firstly ignore additive Gaussian noise)

$$s(t) = A(t)e^{j[\phi(t)+\theta(t)]} + Ce^{j[\omega_p t+\theta(t)]} \tag{4.10}$$

where $A(t)$ and $\phi(t)$ are the symbol amplitude and phase, C and $\omega_p(t)$ are the amplitude and frequency of the pilot tone. The optically coherent symbol and pilot are subjected to the same laser phase noise $\theta(t)$ of the optical carrier. The square-law output signal from the photodiode is given by (assume a detector responsivity of 1 A/W):

$$r_{pd}(t) = s(t)s^*(t) = [A^2(t) + C^2] + CA(t)e^{j[\omega_p t-\phi(t)]} + CA(t)e^{j[-\omega_p t+\phi(t)]} \tag{4.11}$$

Equation 4.11 clearly shows the phase noise cancellation after detection thanks to the presence of the pilot tone. The complex QAM symbol, $A(t)e^{\phi(t)}$, can be demodulated by mixing the direct-detected signal $r_{pd}(t)$ with the complex pilot tone $e^{j\omega_p(t)}$ to yield:

$$r_b(t) = r_{pd}(t)e^{j\omega_p t} = CA(t)e^{j\phi(t)} + [A^2(t) + C^2]e^{j\omega_p t} + CA(t)e^{j[2\omega_p t-\phi(t)]} \tag{4.12}$$

The base-band QAM symbol could then be recovered from $r_b(t)$ by means of matched filtering with the pilot tone frequency chosen to be commensurate with the baudrate, i.e., $f_p = 1/T$, where T is the symbol duration:

$$\begin{aligned} r_m(mT) &= \frac{1}{T}\int_{(m-1)T}^{mT} r_b(t)dt = \frac{1}{T}\int_{(m-1)T}^{mT} CA(t)e^{-j\phi(t)}dt \\ &+\frac{1}{T}\int_{(m-1)T}^{mT} [A^2(t) + C^2]e^{j\frac{2\pi t}{T}}dt \\ &+\frac{1}{T}\int_{(m-1)T}^{mT} CA(t)e^{-j\phi(t)}e^{j\frac{4\pi t}{T}}dt \end{aligned} \tag{4.13}$$

The second and third terms in the above expression integrate to zero since the period of the pilot tone and the symbol duration are commensurate. The matched filter thus recovers the complex QAM symbols at the output samples: $r_m(m) = CA(m)e^{-j\phi(m)}$, $(m-1)T < t < mT$.

4.3.1.2 Additive Gaussian noise analysis

In the following, the effect of noise is incorporated into the baseband signal model in equation 4.10 as $s(t)+n(t)$, where $n(t)$ is the complex additive white Gaussian noise (AWGN). Assuming the laser phase noise $\theta(t)$ is constant over the symbol duration T, the noise contribution after matched filtering is given by:

$$\begin{aligned} n_{pd}(t) &= \left[A(t)e^{j(\phi(t)+\theta(t))} + Ce^{j[\omega_p t+\theta(t)]}\right] \times n^*(t) \\ &+ \left[A(t)e^{-j(\phi(t)+\theta(t))} + Ce^{-j[\omega_p t+\theta(t)]}\right] \times n(t) + n(t) \times n^*(t) \end{aligned} \tag{4.14}$$

$$\begin{aligned} n_b(t) &= n_{pd}(t)e^{j\omega_p(t)} = Cn(t)e^{-j\theta(t)} + \\ &+ \left[n^2(t) + 2A(t)Re\{n^*(t)e^{j[\phi(t)+\theta(t)]}\}\right] e^{j\omega_p t} \\ &+ Cn^*(t)e^{j\theta(t)}e^{j2\omega_p(t)} \end{aligned} \tag{4.15}$$

and:

$$n_m(mT) = \frac{1}{T}\int_{(m-1)T}^{mT} n_b(t)dt = \frac{1}{T}\int_{(m-1)T}^{mT} [n_0(t) + n_1(t) + n_2(t)]dt \tag{4.16}$$

The expressions for $n_{pd}(t)$, $n_b(t)$ and $n_m(mT)$ correspond to the noise components of the photo-detector output, the demodulated signal, and the matched filter signal, respectively. $n_m(mT)$ consists of the noise terms at baseband $n_0(t)$, first harmonic $n_1(t)$ and second harmonic $n_2(t)$. The amplitudes of the transmitted symbols and the pilot both contribute to a slight enhancement of the noise level at the receiver. In practice semiconductor lasers have relative intensity noise (RIN) as well that also affects the noise terms in equation 4.16.

4.3.1.3 Simulation

Baseband simulation has been carried out to validate the theoretical analysis and to verify the immunity of the proposed scheme to the laser phase noise. The simulated laser phase noise includes white-FM noise, relaxation oscillation and excess $1/f^\alpha$ noise [18]. We deploy a 16-QAM system at 2.5 Gbaud with a 2.5 GHz pilot tone. The simulations also accounted for the nonlinearity of the optical IQ modulator. Figure 4.20a depicts the simulated FM-noise spectrum with a white-FM noise level of $S_0 = 1.6$ MHz (the flat portion in the FM-noise spectrum) corresponding to an intrinsic linewidth of 5 MHz, a relaxation oscillation at 8 GHz and a high level of excess noise below 100 MHz. The received symbol constellations with and without the laser phase noise in Figs. 4.20b and 4.20c, respectively, are identical, demonstrating that the scheme is immune to the laser phase noise. The outer symbols show the effects of amplitude enhancement to

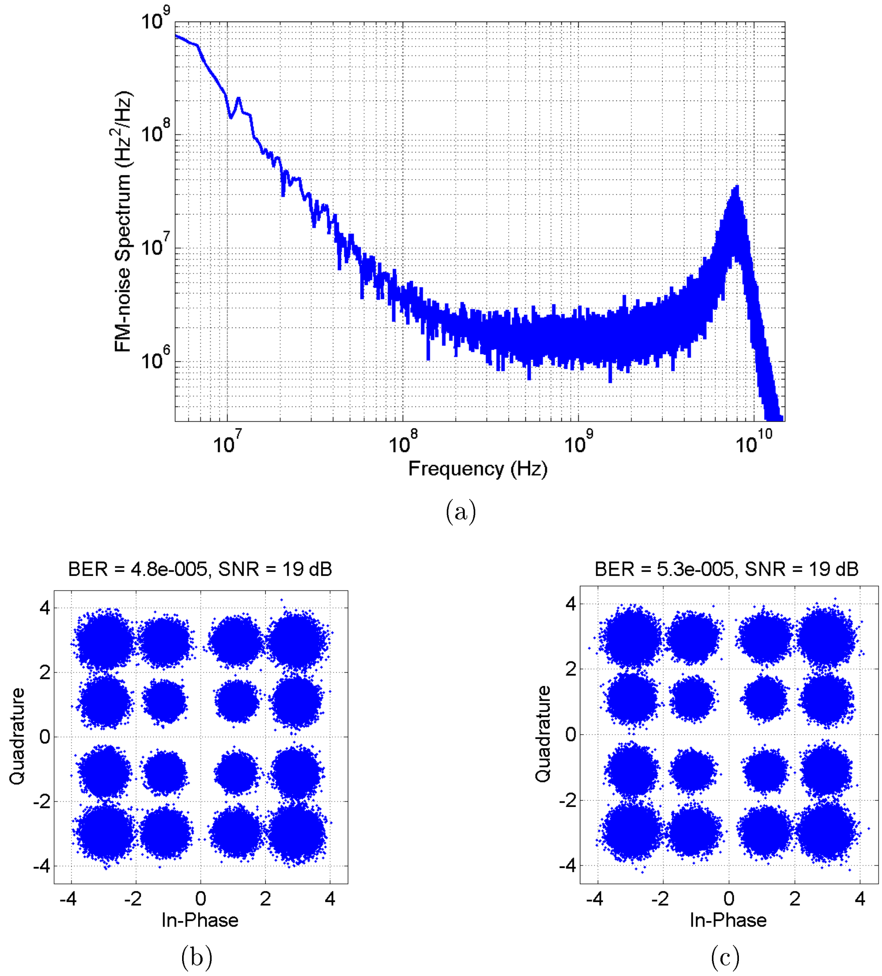

Figure 4.20: (a) FM-noise spectrum of simulated laser phase noise; received symbol constellations (b) without and (c) with laser phase noise.

AWGN as expected from equation 4.16.

The pilot-to-signal power ratio (PSR) is an important factor that would effectively affect the system performance [30]. In the simulation, we evaluate the impact of the PSR and determine its optimum value for the experiments later. Figure 4.21 illustrates the effect of PSR on the BER as well as the received SNR. The optimum range for PSR varies from -2 dB to 4 dB for BER $< 10^{-4}$ and less than 1 dB of SNR degradation.

4.3.2 Experiment Setup

We now evaluate the performance of the high order QAM baudrate-pilot-aided systems when employing different type of lasers at the transmitter. Figure 4.22a shows the experimental setup for a back-to-back pilot-aided system. In the static scenario, the transmitter employed an external cavity laser, a distributed feedback laser or an SG-DBR laser to evaluate the immunity of the proposed scheme to

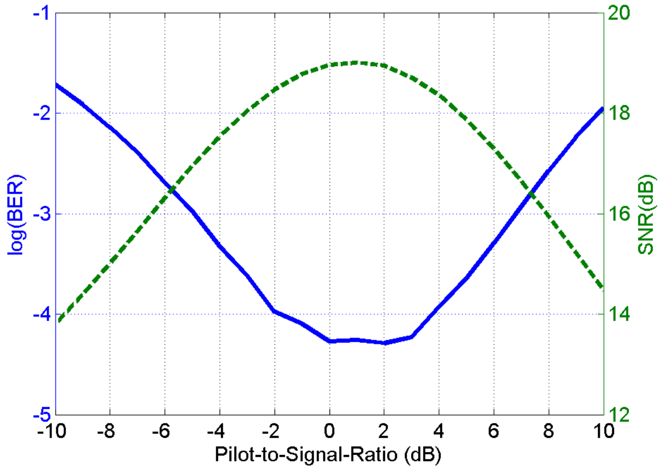

Figure 4.21: The impact of pilot-to-signal power ratio for 16-QAM at 2.5 Gbaud (solid curve: BER performance, dash curve: SNR).

different phase noise characteristics. The 2.5 Gbaud quadrature symbols with a complex sinusoidal pilot tone at 2.5 GHz were generated in Matlab at 4 samples per symbol as illustrated in Fig. 4.23a and loaded onto an arbitrary waveform generator operating at 10 Gsamples/s. The AWG outputs were amplified to drive the IQ modulator that was biased close to the null points. The driving signals were carefully optimized to cope with the nonlinearity of the electrical amplifiers and the optical modulator. The optical output power from the modulator was adjusted by the first variable optical attenuator for the receiver input power. The receiver consisted of two EDFA's and two optical bandpass filters (OBPF) having Gaussian profiles, with a second VOA maintaining an input optical power at 2 dBm into a 10 GHz photo-detector that has an integrated TIA. Figure 4.23b shows the optical spectrum of the transmitted signal. The harmonics of the pilot tone are largely due to the nonlinearity of the modulator.

A real-time scope captured the output signal of the photo-detector at a sampling rate of 25 Gsamples/s. The sampled signals were then fed into a computer for off-line digital signal processing as illustrated in Fig. 4.23b. The clock recovery was firstly performed with the aid of training symbols. The captured signal was then demodulated by multiplying with a complex sinusoid at 2.5 GHz, followed by matched filtering for symbol recovery. The recovered symbols were normalized and compensated for a constant phase offset prior to data demodulation. The BER counting was then carried out on the demodulated bit streams, with 10^5 bits counted for each BER value.

In contrast to the receiver simplicity in Fig. 4.23b, a fully coherent optical receiver would require a front-end of a 90-degree hybrid with a laser LO and balanced photo-detectors. The back-end DSP must perform complex algorithms for carrier frequency and phase recovery in addition to cycle slips correction that depend on the QAM modulation formats and the laser phase noise characteristics. Moreover, the receiver structure in Fig. 4.23b opens the possibility of upgrading widely deployed direct detection systems with the proposed low complexity scheme that enables the use of advanced modulation format transmission.

4.3.3 System performance evaluation

As mentioned above, we evaluate the scheme with lasers having different phase noise characteristics: (1) a 50 KHz linewidth ECL at 1547 nm, (2) a 10 MHz linewidth DFB laser at 1540 nm, and (3) an SG-DBR tunable laser with a white FM noise level corresponding to a 300 KHz linewidth. Again, biasing the passive tuning sections of the SG-DBR laser resulted in large excess $1/f^{\alpha}$ noise that has been shown to significantly degrade the performance of coherent systems, specifically at low baud rates as in previous sections. Figure 4.24 shows the example recovered symbol constellations that differ only slightly for the three different lasers with the baudrate-pilot-aided scheme. The symbols are slightly elliptical due to nonlinearity from the electrical driving amplifiers and the IQ optical modulator which also exhibits non-perfect orthogonality that could not be completely compensated by the receiver DSP. The BER at -20 dBm sensitivity is well below the FEC limit of 3.8×10^{-3} and is within a factor of two for all three lasers. In contrast, a coherent system employing 16-QAM would require very narrow linewidth lasers such as the ECL for 2.5 Gbaud.

Figure 4.25 compares the back-to-back BER performance of the pilot-aided scheme for the three different lasers. The plots show similar performance for all three lasers despite their different phase noise characteristics. The operating wavelength of the tunable SG-DBR laser varied from $\lambda = 1547.9nm$ when the gain section was biased at $I_{Gain} = 120mA$, to $\lambda = 1541.8nm$ when both gain and back sections were biased, and $\lambda = 1551.5nm$ when biasing all four sections, yielding increasing levels of excess FM noise. The performance difference between the lasers is attributed to the disparity in the demodulated noise enhancement that depends on the output power of the lasers, their RIN noise, and receiver noise as discussed previously. The experimental results confirm that the proposed baudrate-pilot-aided scheme is highly immune to the laser phase noise.

To recap, a baudrate-pilot-aided transmission with direct detection scheme for high-order QAM formats has been proposed and demonstrated through analytical modelling and experimental results. The low complexity receiver is highly immune to the laser phase noise. The proposed scheme was demonstrated for a 16-QAM system operating at 2.5 Gbaud and employing an SG-DBR laser with

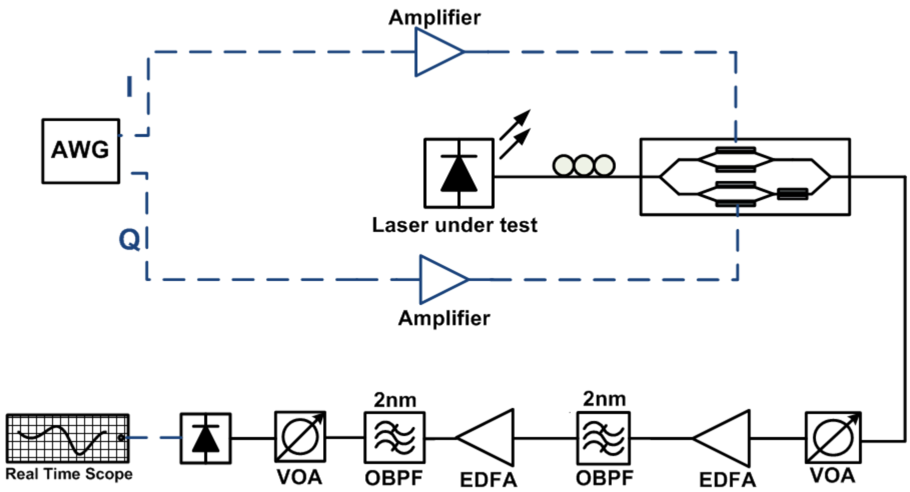

(a)

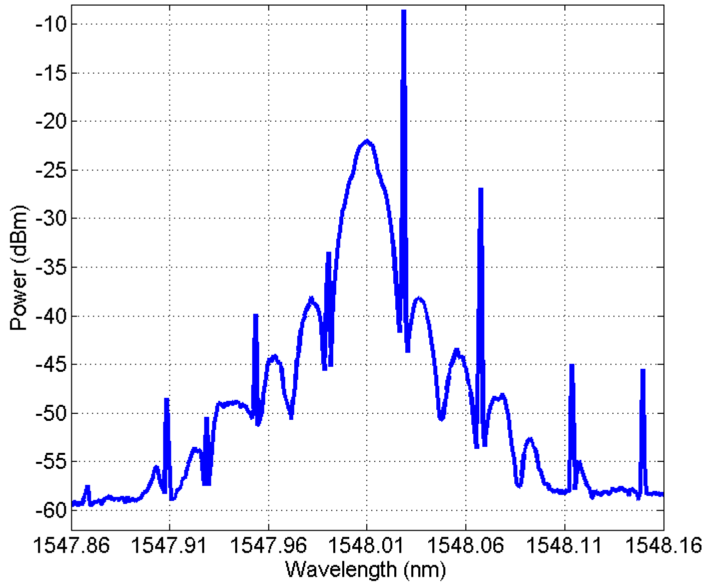

(b)

Figure 4.22: (a) Experiment setup for baudrate-piloted-aided scheme for 16-QAM at 2.5 Gbaud; (b) Optical spectrum of transmitted signal (optical resolution bandwidth: 0.16pm).

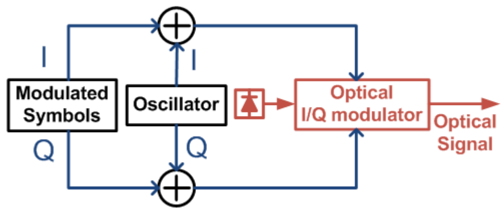

(a)

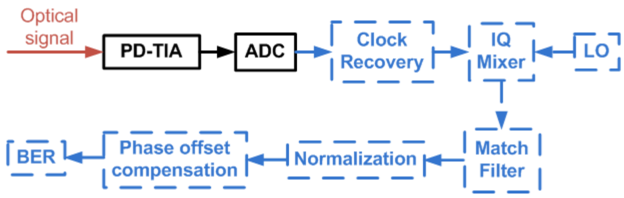

(b)

Figure 4.23: Transceiver structure of baudrate-pilot-aided scheme for QAM: (a) Transmitter structure; (b) Receiver structure including signal processing (in dash line), PD: photodiode, TIA: trans-impedance amplifier, LO: local oscillator.

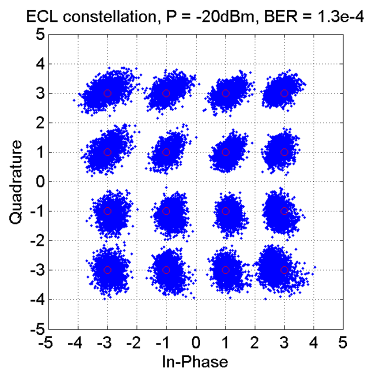

(a)

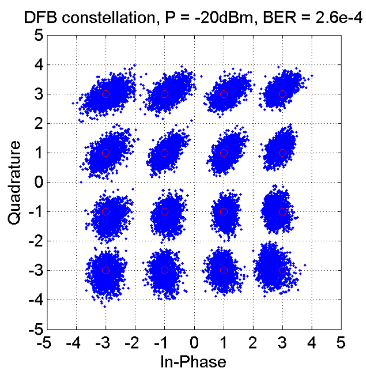

(b)

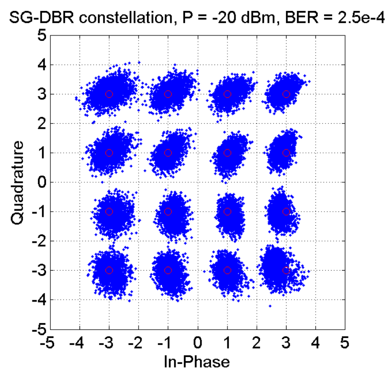

(c)

Figure 4.24: Received constellations of pilot-aided 16-QAM at 2.5 Gbaud in static scenario with three different lasers: (a) ECL ($\Delta\nu = 50KHz$), (b) DFB laser ($\Delta\nu = 10MHz$), (c) SG-DBR laser biasing 4 sections.

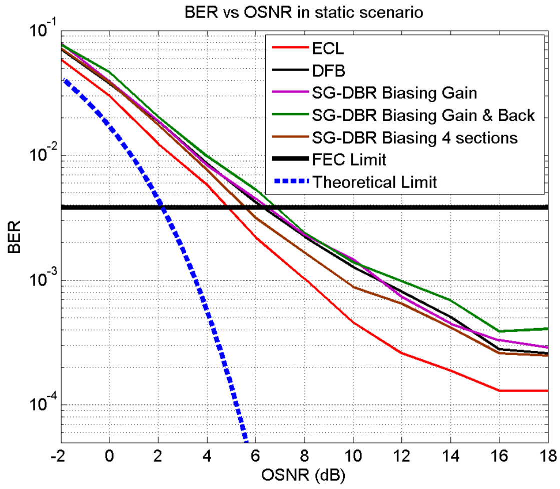

Figure 4.25: BER of 16-QAM baudrate-pilot-aided systems at 2.5 Gbaud utilizing the three different types of lasers.

large excess phase noise.

4.4 Summary

In this chapter, we have extensively examined the significant impacts of the complicated phase noise processes of the SG-DBR lasers in a coherent optical communication system employing high order modulation formats. We confirmed that while the white FM-noise has been determined to largely define the lower bound of BER performance, the system operation could potentially be impaired by the excess laser phase noise. We have then examined the robustness of a second-order DD-PLL phase tracking technique in a coherent system employing 16-QAM modulation format at 16 Gbaud to overcome this issue. The experimental results present the ability to employ monolithic tunable lasers for high order QAM modulation formats with coherent systems. The cycle slip effects of a SG-DBR laser in a 10.7 Gbaud QPSK transmission system with well-known phase noise tracking algorithms is also investigated. A new CS detection/correction method has then been developed to solve this problem.

Subsequently, we proposed and demonstrated a coherent self-heterodyne receiver based on PM detection for DQPSK modulation to effectively overcome the phase noise issue of the SG-DBR lasers. The new coherent PM detection receiver not only offers the potential for a low-cost integrated solution but can also significantly simplify the front end of optical coherent receivers with the feasibility of migrating toward higher order modulation formats. A baudrate-pilot-aided transmission with direct detection scheme for high-order QAM formats has also been proposed. The low complexity receiver is highly immune to the laser phase noise. The proposed scheme was demonstrated for a 16-QAM system operating at 2.5 Gbaud and employing an SG-DBR laser transmitter. Besides the above advantages, the baudrate-pilot-aided transmission scheme has its own drawbacks. These include wasting additional optical power in the pilot tone and having higher requirement on the SNR of the received signal. These disadvantages would also need to be taken into account when designing a communications link with the proposed method.

As the optical communications networks moving towards advanced modulation formats and fast re-configurable networks, the next chapter will be dedicated to investigating the use of the SG-DBR lasers in a fast-switching optical packet network employing the above advanced modulation formats. The performance degradation of such a system during and after a wavelength-switching event of a SG-DBR laser transmitter will be intensively investigated.

Bibliography

[1] M. Nakazawa, "Extremely Advanced Transmission with 3M Technologies (Multilevel Modulation, Multi-core & Multi-mode)," OFC- 2012, pp. OTu1D.1, 2012.

[2] A.H. Gnauck et. al, "Generation and Transmission of 21.4-Gbaud PDM 64-QAM Using a Novel High-Power DAC Driving a Single I/Q Modulator," J. Lightw. Technol., vol. 30, pp. 532-536, 2012.

[3] L.B. Mercer, "1/f Frequency Noise Effects on Self-Heterodyne Linewidth Measurements," J. Lightw. Technol., vol. 9, pp. 485-493, 1991.

[4] T.N. Huynh, L. Nguyen, L. Barry, "Delayed Self-Heterodyne Phase Noise Measurements with Coherent Phase Modulation Detection", Photon. Technol. Lett., vol. 24, pp. 249-251, 2012.

[5] K. Kikuchi, "Characterization of semiconductor-laser phase noise and estimation of bit-error rate performance with low-speed offline digital coherent receivers," Optics Express, vol. 20, pp. 5291- 5302, 2012.

[6] M.C. Larson, Y.A. Akulova, C.W. Coldren, T. Liljeberg, G.A. Fish, S. Nakagawa, A. Dahl, P. Kozodoy, D. Bingo, M. Bai, N. Ramdas, S. Penniman, T. Wipiejewski, L.A. Coldren, "High Performance widely-Tunable SG-DBR Lasers", Proc. SPIE 2003, vol. 4995, pp. 66-80, 2003.

[7] M. Nakazawa, K. Kikuchi, and T. Miyazaki, High Spectral Density Optical Communication Technology, Springer, 2010.

[8] Matthias Seimetz, High-order Modulation for Optical Fiber Transmission, Springer, 2009.

[9] S. Zhang, P.Y. Kam, J. Chen, C. Yu, "Bit-error rate performance of coherent optical M-ary PSK/QAM using decision-aided maximum likelihood phase estimation," Opt. Express 18, 12088-12103, 2010.

[10] G. J. Foschini, R. D. Gitlin, and S. B. Weinstein, "On the selection of a two-dimensional signal constellation in the presence of phase jitter and Gaussian noise," Bell Syst. Tech. J., vol. 52, pp. 927–965, Jul./Aug. 1973.

[11] J. G. Proakis, Digital Communications, McGraw-Hill, 1995.

[12] T. Nakagawa, M. Matsui, T. Kobayashi, K. Ishihara, R. Kudo, M. Mizoguchi, Y. Miyamoto, "Non-Data-Aided Wide-Range Frequency Offset Estimator for QAM Optical Coherent Receivers," OFC 2011, pp. OMJ1.

[13] Y. Mori, C. Zhang, K. Igarashi, K. Katoh, and K. Kikuchi, "Unrepeated 200-km transmission of 40-Gbit/s 16-QAM signals using digital coherent receiver," Opt. Express vol. 17, pp. 1435-1441, 2009.

[14] S. Zhang, P.Y. Kam, C. Yu, J. Chen, "Decision-aided carrier phase estimation for coherent optical communications," J. Lightw. Technol. 28, 1597-1607 (2010).

[15] T. Pfau, S. Hoffmann, R. Noé, "Hardware-efficient coherent digital receiver concept with feedforward carrier recovery for M-QAM constellations," J. Lightw. Technol. 27, 989-999, 2009.

[16] T.N. Huynh, L. Nguyen, L. Barry, "Effects of Phase Noise of Monolithic Tunable Laser on Coherent Communication Systems," Optics Express, vol. 20, pp. B244-B249, 2012.

[17] U. Mengali and A.N. D'Andrea, Synchronization Techniques for Digital Receivers, Plenum Press, 1997.

[18] Tam N. Huynh, Lim Nguyen, Liam P. Barry, "Phase Noise Characterization of SG-DBR Lasers using Phase Modulation Detection Method With Delayed Self-Heterodyne Measurement," IEEE/OSA Journal of Lightwave Technology, vol. 31, pp. 1300-1308, 2013.

[19] H. Zhang, Y. Cai, D. G. Foursa, and A. N. Pilipetskii, "Cycle slip mitigation in PolMux-QPSK modulation," OFC 2011, paper OMJ7, USA, 2011.

[20] C.R.S. Fludger, D. Nuss, T. Kupfer, "Cycle slips in 100G DP-QPSK transmission systems," OFC 2012, paper OTu2G.1, USA, 2012.

[21] A. Bisplinghoff et al., "Slip-Reduced Carrier Phase Estimation for Coherent Transmission in the Presence of Non-Linear Phase Noise", OFC 2013, paper OTu3I.1, USA, 2013.

[22] P.J. Winzer, G. Raybon, H. Song, A. Adamiecki, S. Corteselli, A.H. Gnauck, D.A. Fishman, C.R. Doerr, S. Chandrasekhar, L.L. Buhl, T.J. Xia, G. Wellbrock, W. Lee, B. Basch, T. Kawanishi, K. Higuma, Y. Painchaud,"100-Gb/s DQPSK Transmission: from laboratory experiments to field," J. Lightw. Technol. 26, 3388-3402, 2008.

[23] R.A. Griffin and A.C. Carter, "Optical differential quadrature phase-shift key (oDQPSK) for high capacity optical transmission," WX6, OFC 2002, USA, 2002.

[24] N. Kikuchi and S. Sasaki, "Highly sensitive optical multilevel transmission of arbitrary quadrature-amplitude modulation (QAM) signals with direct detection," J. Lightw. Technol. 28, 123-130, 2010.

[25] T.N. Huynh, L. Nguyen, and L.P. Barry, "Coherent optical receiver using phase modulation detection," ThL5, IEEE IPC 2011, USA, 2011.

[26] M. Vaez-Iravani and R. Toledo-Crow, "Pure linear polarization imaging in near field scanning optical microscopy," Applied Physics Letters 63, pp. 138-140, 1993.

[27] K. Wang, Z. Ding, Y. Zeng, J. Meng, and M. Chen, "Sinusoidal B-M method based spectral domain optical coherence tomography for the elimination of complex-conjugate artifact," Opt. Express 17, pp. 16820–16833, 2011.

[28] E. Ip, A.P.T. Lau, D.J.F. Barros, J.M. Kahn, "Coherent detection in optical fiber system", Opt. Express 16, pp. 753–791, 2008.

[29] F. Xia, S. Datta, and S.R. Forrest, "A monolithically integrated optical heterodyne receiver", Photon. Technol. Lett. 17, pp. 1716-1718, 2005.

[30] T. Kobayashi, A. Sano, A. Matsuura, Y. Miyamoto, K. Ishihara, K. Gustafson, P. Kelley, "Nonlinear Tolerant Spectrally-Efficient Transmission Using PDM 64-QAM Single Carrier FDM With Digital Pilot-Tone," J. Lightwave Technol., vol. 30, pp. 3805–3815, 2012.

[31] S. Shinada, M. Nakamura, Y. Kamio, N. Wada, "16-QAM optical packet switching and the real-time self-homodyne detection using polarization-multiplexed pilot-carrier," Optics Express, vol. 20, pp. B535–B542, 2012.

Chapter 5

Optical Packet Switching with Advanced Modulation Formats

As discussed in the previous chapters, to address the capacity crunch in optical networks, spectrally efficient transmission schemes employing high order quadrature amplitude modulation formats with coherent detection are being extensively explored as the potential candidates for next generation optical networks [1]. In addition, rapid reconfiguration of the optical network with optical packet/burst switching technology allows the amplification bandwidth of the fiber to be used more efficiently [2, 3, 4]. Combining coherent transmission techniques with optical packet/burst switching technology can enable optical networks that are highly efficient both temporally and spectrally. Optical packet switching that employs fully coherent detection for PM-QPSK [2], self-homodyne detection for DQPSK [3, 4], 16-QAM polarization multiplexed pilot with self-homodyne coherent detection [5], or 16-QAM Baudrate-Pilot-Aided transmission scheme with direct detection [6] have been recently reported.

As discussed in chapter 1, one of the potential optical networks configuration employing optical packet/burst switching with advanced modulation formats is as follows: At the optical transportation layer, we make use of fast-tunable optical transceivers in the optical nodes. These tunable transceivers can switch to or select an available wavelength on the ITU-grid that is used to transmit or receive the data optical packets. Obviously, the key component in fast-tuning transceivers will be the fast-wavelength-switching tunable lasers, and the SG-DBR laser is a potential choice as discussed previously. However the considerable phase/frequency noise in SG-DBR lasers would fluctuate even more during a wavelength switching transient in this highly dynamic network scenario, especially for short optical packets. In this chapter, we will investigate the performance of the system emulating the optical packet switching scenario utilizing advanced modulation formats. We will firstly examine such a system with DQPSK modulation format at 10.7 Gbaud in section 5.1. In section 5.2, we then move to optical packet switching systems employing higher order QAM modulation format with the proposed Baudrate-Pilot-Aided transmission scheme in the previous chapter. The last section, section 5.3 will conclude the chapter.

5.1 Optical packet switching with Self-Homodyne DQPSK

Wavelength switching times of less than 5ns have been demonstrated using the SG-DBR laser [7] making it suitable for optical packet switching, however its significant phase noise level may reduce its suitability if phase-shift-keying based advanced optical modulation formats are employed in the optical packet switched network. Even though the DQPSK modulation format with direct detection has a high tolerance to laser phase noise, this transmission scheme still suffers from the high level of phase/frequency instability during the wavelength switching event of the SG-DBR laser. In this section, through detailed experimental studies, this performance degradation during the transient state of the emulated optical packets is investigated.

5.1.1 Experiment setup for time resolved BER measurement

The experiment setup to investigate the performance of DQPSK transmission system during transient and steady states of a wavelength switching event is illustrated in Fig. 5.1. We demonstrate a 10.7 Gbaud DQPSK transmission system employing an SG-DBR transmitter. The SG-DBR laser was a simple butterfly packaged device without a wavelength locker, micro-controller or other circuitry, thus giving a realistic account of the device capabilities. The back mirror current was biased to operate with single mode static operation at wavelengths 1553.54 nm or 1547.3nm respectively. An IQ modulator (biased close to the null points) was driven by the complementary PRBS outputs of a 10.7Gb/s Pulse Pattern Generator (PPG) de-correlated by 12 bits using an electrical delay. The I and Q electrical driving signals were lowpass filtered and amplified before entering the IQ modulator. The modulated optical output is then passing through a two-stage optical pre-amplified receiver as in Fig. 5.1. A 10.7Gb/s one-bit-delay interferometer was implemented at the receiver side to differentially demodulate the in-phase or quadrature data independently.

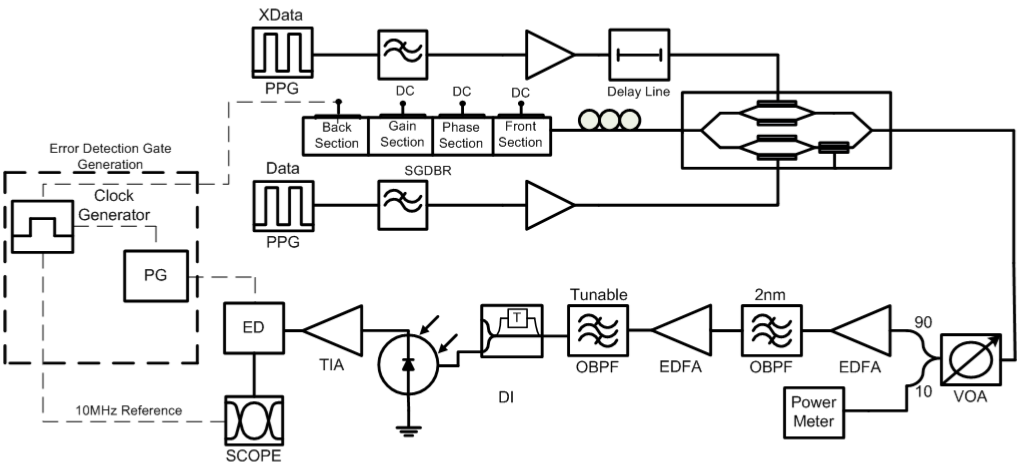

Figure 5.1: Experiment setup for time resolved BER measurement

To emulate an optical packet switching scenario, instead of a constant bias current to the Back section of the SG-DBR laser as in the static scenario, a square wave of 10MHz was used to drive the back section of the SG-DBR laser to switch between the two wavelengths (corresponding to 50ns data packets). The desired optical channel (wavelength) is selected by means of the narrow band optical filter at the front-end of the receiver as in Fig. 5.1. We then measured the time resolved BER during this process. To do so, the Error Detector (ED) was gated with 5ns pulses that could be varied in position with respect to the packet. The pulse generator and the oscilloscope were both triggered by the switching signal. The measurement results for both static and dynamic switching scenarios are presented in the next subsection.

5.1.2 Measurement results

Firstly, for the static scenario, the BER was measured separately for the I and Q components of the received signal at each wavelength (1553.54nm and 1547.3nm) as shown in Fig. 5.2a. Receiver sensitivities of between -29dBm and -30dBm at a BER of 10^{-9} were observed for I and Q on each channel. As illustrated by the results, we have the system operating well with stable performance in a static scenario. We then switch the operating wavelength of the SG-DBR laser between the two channels as described in the previous subsection. Figure 5.2b depicts the average optical spectrum observed from an optical spectrum analyzer (OSA) for the two optical channels when applying wavelength switching.

For the dynamic switching scenario, the time resolved BER performance during the switching event are shown in Fig. 5.2c. It can be seen that the time required to switch from 1547.3 nm to 1553.54 nm and obtain error free transmis-

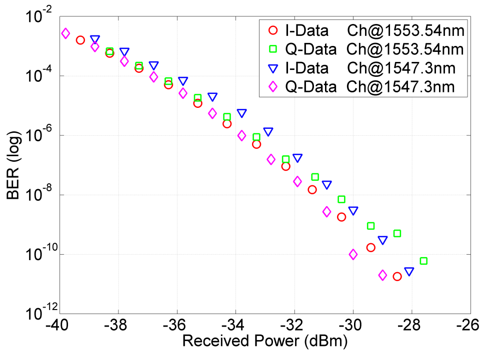

(a) Receiver sensitivity in Static scenario

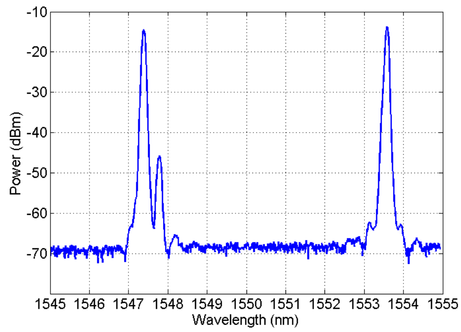

(b) Switching wavelengths

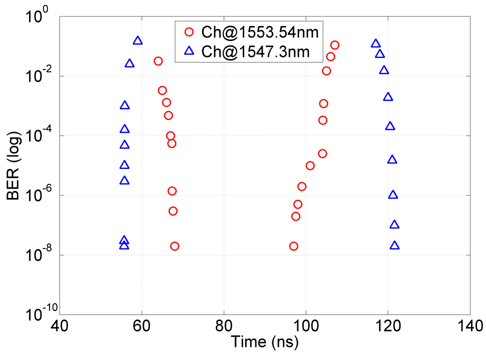

(c) Switching scenario

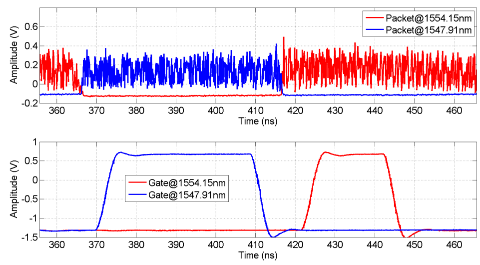

(d) Measured data packets

Figure 5.2: Time-resolved BER in switching event of SG-DBR

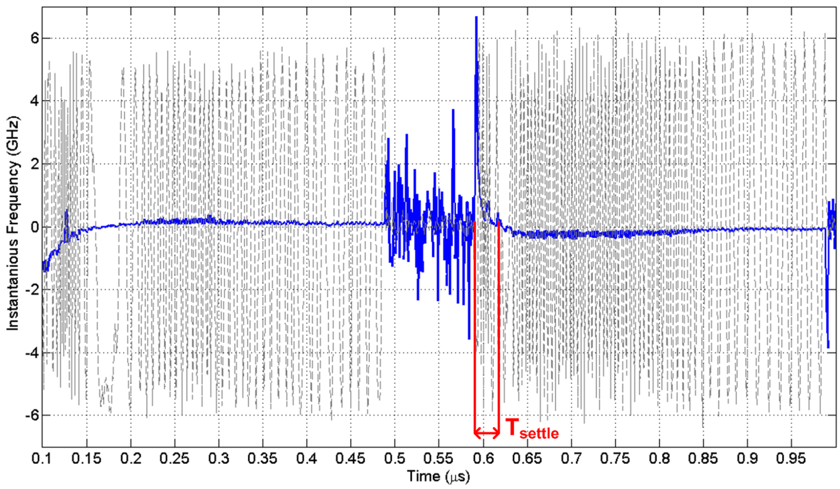

Figure 5.3: The measured instantaneous frequency (blue solid line) on top of the amplitude of the optical packets (dash gray line) for the switching event of SG-DBR laser

sion at this wavelength was approximately 12 ns while it takes approximately 24 ns to switch back to 1547.3nm. The upper figure in Fig. 5.2d shows the example oscilloscope traces of the measured data packets while the lower figure represents the error free transmission windows for the two optical channels.

Even though the SG-DBR lasers take about 5ns to switch from one wavelength to the other wavelength, it would take longer time for the frequency/phase of the optical output to settle down. The performance degradation during the transient stage can be attributed to the phase/frequency instability during the switching event. We then performed the phase/frequency instability measurement for wavelength switching events of the SG-DBR laser using the Self-Homodyne method with coherent receiver to clarify the above results. Similarly, the Back section was used to switch the wavelength as in the system experiments but at lower switching frequency, 1 MHz, for longer observation time. The instantaneous frequency was then calculated from the captured E-field. Figure 5.3 shows the instantaneous frequency (superimposed on captured data in gray dash line) during a wavelength switching event. The result shows that it would take less than 25 ns for the instantaneous frequency from the tunable laser to be within 500MHz of its target frequency, corresponding to the time for the DQPSK system obtain error free transmission after the wavelength switch as in the system experimental results.

5.2 Optical packet switching with Baudrate-Pilot-Aided modulation scheme

As demonstrated in chapter 4, the Baudrate-Pilot-Aided transmission scheme with direct detection has the advantage of immunity to laser phase/frequency noise. Obviously, this transmission scheme is highly suitable for optical packet switching networks where the phase/frequency of the optical carrier in each packet fluctuates strongly. Specially when the optical packets become shorter (for higher throughput of the entire network), the optical carrier might not be able to settle down sufficiently quickly to permit advanced modulation format transmission in the packet. In this section, we will investigate the system performance of the emulated optical packets in a switching network utilizing 16-QAM Baudrate-Pilot-Aided transmission at 2.5 Gbaud.

5.2.1 Experiment setup

The experiment setup is shown in Fig. 5.4 and is similar to the setup for Baudrate-Pilot-Aided transmission in the preceding chapter except some changes for the

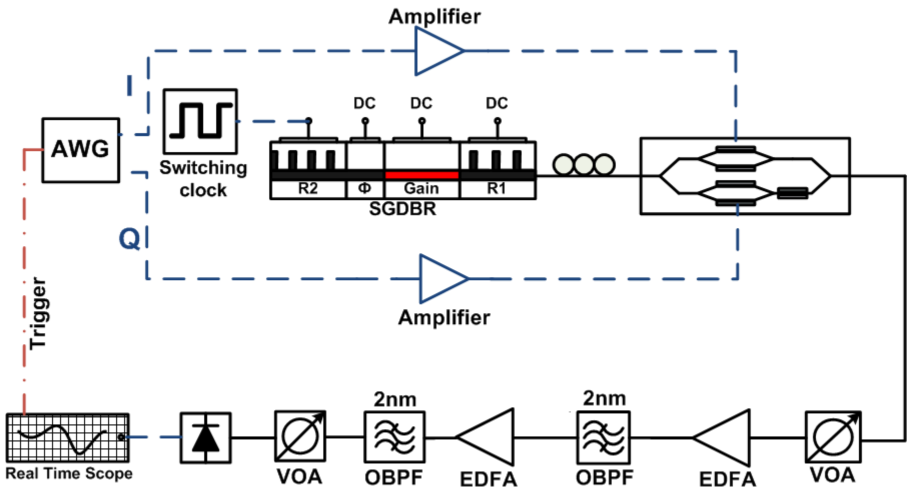

Figure 5.4: Experimental setup for baudrate-piloted-aided scheme for 16-QAM at 2.5 Gbaud for optical wavelength switching scenarios.

optical packet switching scenario. We investigate the performance of the proposed scheme in a dynamic scenario corresponding to a wavelength switching event of the SG-DBR laser. The optical packet switching was emulated by driving the back section of the SG-DBR device with a 1 MHz clock signal that has the high and low voltage levels adjusted for wavelength switching between $\lambda = 1547.9nm$ and $\lambda = 1541.8nm$. The gain section bias was kept at 120 mA throughout the experiment. The first optical bandpass filter was used to select the required channel. No power penalty was observed when the bandwidth of the optical band pass filter varied from 1 nm to 0.4 nm (as would be employed in a 100 GHz ITU-grid system). Figure 5.5 shows the example received optical packets at the photo-detector output over a $12\mu s$ time interval. A trigger signal from the AWG to the real-time scope, as shown in Fig. 5.4, supports clock recovery for the selected packet.

5.2.2 Measurement results

At 2.5 Gbaud with 16-QAM modulation format, the dynamic BER was found to reach stable performance after a transient period of 4.8 ns, or 12 symbols, following a wavelength switching event. Figures 5.6a and 5.6b display the symbol constellations of the recovered optical packets in Fig. 5.5 with and without the 12 transient symbols, respectively, immediately after the laser has switched wavelength.

The aggregated BER counting was carried out over 12 optical packets, each excluding the 12 transient symbols following the wavelength switching event.

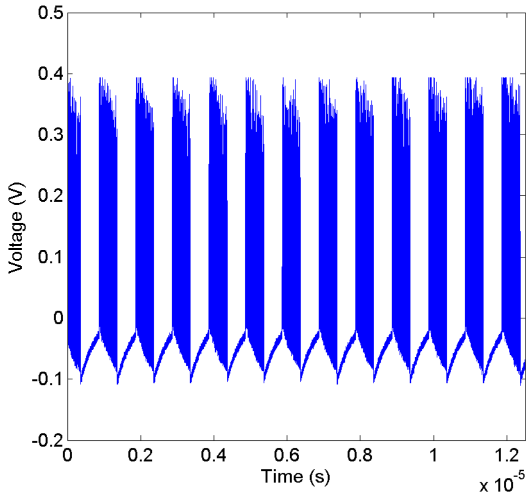

Figure 5.5: Emulated optical packets for optical packet switching scenario with SG-DBR lasers

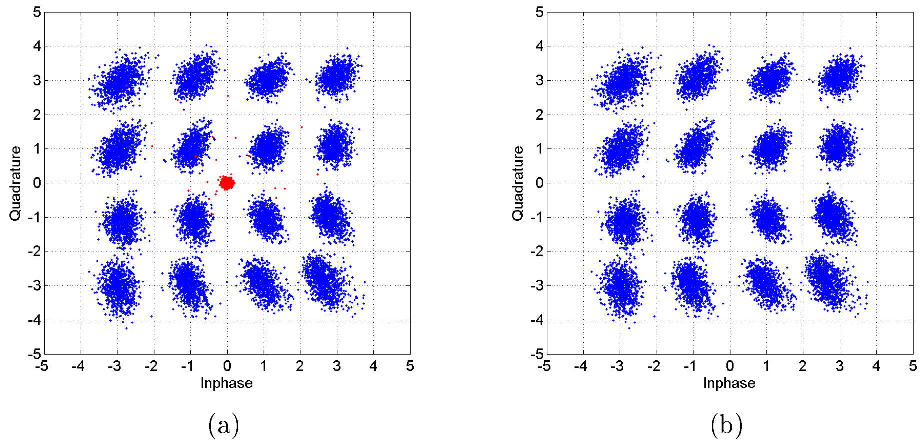

Figure 5.6: Emulated optical packet switching with SG-DBR lasers: (a) Received constellation with transient symbols (in red color), (b) Received constellation without transient symbols.

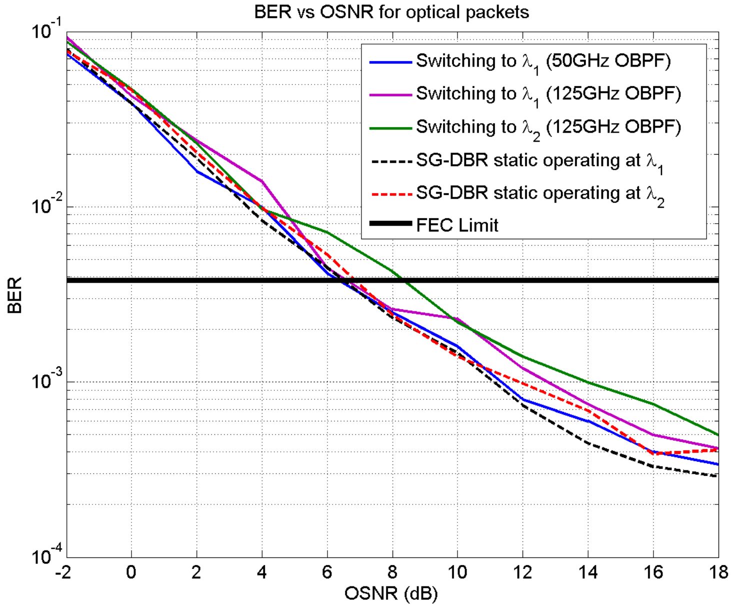

Figure 5.7: Aggregated BER vs. OSNR of optical packets selected less than 5 ns after switching event.

Figure 5.7 shows the aggregated BER versus OSNR for the wavelength switching packets that compares very well to the static BER. The results demonstrate that with the proposed pilot-aided scheme, the dynamic performance reaches the stable condition without any degradation within 12 symbols of a switching event. This is in spite of the inevitable laser frequency transients that have been found to degrade the performance of DQPSK in wavelength switching applications [4]. We note that coherent detection can support optical packet or burst switching with about an 8 dB improvement in receiver sensitivity. However, the receiver complexity would be higher and the duration of a switching transient would last much longer than 12 symbols, with the DSP taking a few hundred symbols to achieve the steady state performance [8]. This would greatly reduce the network throughput as the time required after a laser switching event for successful data transmission could be as high as hundreds of nano-seconds. Furthermore, coherent detection of high-order modulation formats is significantly affected by laser phase noise and requires very narrow linewidth laser for both transmitter and receiver LO lasers as discussed in the previous chapter.

To recap, the baudrate-pilot-aided transmission with direct detection scheme for 16-QAM modulation formats has shown that the low complexity receiver is highly immune to the laser phase noise and well suited for fast optical packet switching. The proposed scheme was demonstrated for a 16-QAM system operating at 2.5 Gbaud and employing an SG-DBR laser with large excess phase noise. The system reached the steady state operation in less than 5 ns following a switching event. Compared with an optical packet (burst) coherent receiver, the proposed scheme with its spectrally efficient pilot tone employs low complexity receiver and DSP implementation, and has the ability to migrate to higher modulation formats and baud rates.

5.3 Summary

In this chapter, we have examined the performance of the emulated optical packet switching scenario using the SG-DBR laser as a fast-wavelength-switching device. These systems employed advanced modulation formats which offer high spectral efficiency to increase the total throughput of the entire optical network. The performance degradation during the transient stage of the wavelength switching events, corresponding to the beginning of the optical data packet, has been observed and investigated. The instability of laser emission frequency along the optical data packet results in performance degradation of the system employing DQPSK modulation format.

To overcome the above issue, we then proposed and investigated the performance of the Baudrate-Pilot-Aided high order QAM transmission scheme with direct detection for optical packet switching networks. The proposed scheme significantly improves the system performance during the transient stage of the wavelength switching event, which satisfies the need to migrate to higher order modulation formats such as 16-QAM or 64-QAM. Experimental results in this chapter with 16-QAM at 2.5 Gbaud have confirmed this proposed solution.

Bibliography

[1] R. J. Essiambre, R.W. Tkach, "Capacity trends and limits of optical communication networks," Proceedings of the IEEE, vol. 100, pp. 1035-1055, 2012.

[2] J.E. Simsarian, J. Gripp, A.H. Gnauck, G. Raybon, P.J. Winzer, "Fast-tuning 224-Gb/s Intradyne receiver for optical packet networks," in OFC 2010, paper PDPB5.

[3] S. Shinada, H. Furukawa, N. Wada, "Huge capacity optical packet switching and buffering," Optics Express, vol. 19(26), B406–B414, 2011.

[4] T.N. Huynh, K. Shi, F. Smyth, L.P. Barry, "DQPSK optical packet switching using an SG-DBR laser," in CLEO Europe 2011, paper CI1.

[5] S. Shinada, M. Nakamura, Y. Kamio, N. Wada, "16-QAM optical packet switching and the real-time self-homodyne detection using polarization-multiplexed pilot-carrier," Optics Express, vol. 20, pp. B535–B542, 2012.

[6] Tam N. Huynh, Lim Nguyen, V. Vujicic, Liam P. Barry, "Pilot-Tone Aided Transmission of High-Order QAM for Optical Packet Switched Networks," IEEE/OSA Journal of Optical Communications and networking, vol. 6, no. 2, pp. 152-158, 2014.

[7] J.E. Simsarian, M.C. Larson, H.E. Garrett, H. Xu, T.A. Strand, "Less than 5-ns wavelength switching with an SG-DBR laser," IEEE Photon. Technol. Lett., vol. 18, pp. 565–567, 2006.

[8] R. Maher, D.S. Millar, S.J. Savory, B.C. Thomsen, "Widely Tunable Burst Mode Digital Coherent Receiver With Fast Reconfiguration Time for 112 Gb/s DP-QPSK WDM Networks," IEEE/OSA Journal of Lightwave Technology, vol. 30, pp. 3924-3930, 2012.

Chapter 6

Conclusions and Future Directions

The state-of-the-art optical transportation networks are moving to provide better communications services with higher total capacity and lower latency in the entire network. Advanced modulation formats accompanied by highly agile optical networks would enable the ability to cope with the above targets for a future communications network infrastructure. The aim of this thesis is to address some of the important challenges that need to be tackled for the implementation of both advanced optical modulation formats and fast re-configurable optical networks in the near future. In this chapter, we will summarize the achievements of the research presented in this thesis and also discuss future research directions.

6.1 Conclusion

Through chapters 1-5 in this thesis, we have extensively investigated the application of spectrally efficient optical modulation formats in future fast re-configurable optical networks. Firstly, we reviewed the current state of the art of optical transportation networks. The fundamental limit of the optical networks with the recent research and development trends have been revised. We then propose that one effective way to further increase the total throughput of the entire optical transportation network is to combine the advanced optical modulation formats with optical packet/burst switching networks. The key component in such a system is the fast-wavelength-switching monolithic tunable laser, particularly the Sampled-Grating Distributed Bragg Reflector laser. However as demonstrated previously, SG-DBR lasers experience sophisticated phase noise properties that would significantly impact their performance within systems which use advanced modulation formats. I then proposed and experimentally demonstrated a few approaches to overcome these issues. Finally, the application of the SG-DBR lasers in optical packet switching networks employing advanced modulation formats have been examined. The key findings resulting from this research are summarized as follows.

6.1.1 Device perspective

The SG-DBR laser device exhibits complicated phase noise characteristics. Firstly, we reviewed the fundamentals of phase noise in semiconductor lasers and then developed the theory for the multi-section monolithic tunable lasers. The theoretical phase/frequency noise of the SG-DBR laser consists of: (1) the Schawlow-Townes-Henry phase noise (quantum noise followed a random-walk process in phase, also call white FM-noise) with relaxation oscillation above 5GHz; (2) the filtered FM-noise from the dynamics of the carriers in passive sections (tuning sections); and especially the low frequency noise including the flicker $1/f$ noise and the frequency random-walk $1/f^2$ noise. Accurate phase noise measurement methods have been demonstrated and confirmed the phase noise processes in SG-DBR lasers. By looking at the detailed phase noise measurement results, we were able to resolve the contributions of the individual phase processes which will be useful for understanding their origin, and proposing techniques to reduce the phase noise in SG-DBR lasers.

The filtered FM-noise could be reduced through a careful laser design process to optimize the laser structure when the phase noise property was targeted. The noise from the current source injecting into the passive sections is one of the contributions to the filtered FM-noise and the low frequency noise (the $1/f^{\alpha}$ noise). A careful design for low noise current sources (especially for injecting into passive sections) would help to improve the spectral purity of these tunable lasers.

6.1.2 Communication Systems perspective

The detailed understanding of phase noise properties of the SG-DBR lasers supports the extensive investigation of the performance of optical communication systems with advanced modulation formats employing this type of tunable laser. Experimental results confirmed that the white FM-noise basically defines the lower limit for the BER performance of the coherent communications systems while the low frequency $1/f^{\alpha}$ noise in the SG-DBR lasers will potentially increase the instability of the system performance in term of BER and cycle slip probability.

Novel transmission schemes with advanced DSP algorithms have been proposed to effectively overcome these issues. For fully optical coherent reception, a second-order DD-PLL can be deployed to simultaneously track the fast phase and low frequency noise of the SG-DBR lasers. For self-coherent reception, a novel coherent self-heterodyne receiver with PM detection technique has been shown to give very high laser phase noise tolerance and be able to move to higher order modulation formats. For direct detection, a Baudrate-Pilot-Aided QAM transmission scheme was proposed and proved its robustness to any phase/frequency noise processes in the SG-DBR laser, while offering a high spectral efficiency solution for pilot-based communication systems.

6.1.3 Optical packet switching networks perspective

The performance degradation during the transient state of a wavelength switching event of the SG-DBR lasers has been examined. Experimental results show that the optical packet switching systems employing DQPSK modulation format would require tens of nano-seconds to achieve error-free transmission after a wavelength switching event. Even though the SG-DBR lasers take less than 5ns to switch from one wavelength to another, it would take a longer time (10s of ns) for the frequency/phase of the emission optical field to settle down . In this case, the Baudrate-Pilot-Aided QAM transmission scheme would be the most suitable solution due to its immunity to large phase/frequency fluctuations of the laser field. Experimental results confirmed that this transmission scheme can reach its static performance within 5 ns after the wavelength switching event.

6.2 Future research

From the current achievements of this research, some of future research directions would be as follows.

6.2.1 Devices perspective

A more complete mathematical model for monolithic tunable lasers would need to be developed to obtain a deeper understanding of the original physical processes of laser phase noise. The new model would account for more device parameters in terms of device structure and material of different sections in the tunable laser. This would allow us to compare the extensive characterization of the fabricated devices with the results from these models. Optimizing the monolithic device structure by targeting laser phase noise properties would be a challenging research direction.

Photonic integration for the transmitter and receiver used in coherent communication systems would also need to be carefully investigated. In the mean time, the peripheral electronic circuits for biasing, driving, temperature conditioning, etc. would need to be extensively re-examined. The final research target would be an integrated solution for the compact fast-tuning optical transceiver that would effectively realize the optical nodes for an all optical packet switching network.

6.2.2 Communication Systems perspective

In parallel with device research and development, advanced DSP for both the transmitter and receiver would need to be improved to optimize the ultimate system performance. Especially, for the fully coherent systems, advanced phase/frequency tracking algorithms in combination with a robust cycle sip correction method would require more intensive efforts to bring the monolithic tunable lasers to the commercially coherent communication applications. The total spectral efficiency of the networks would be significantly increased with space-division-multiplexing. A combination between advanced modulation formats with SDM and optical packet switching would drive a very interesting research direction with more challenges.

The baudrate-pilot-aided QAM transmission scheme with direct detection demonstrates a potentially commercial application for a low cost optical communication link. The proposed system would however require more detailed investigation into the hardware implementation that would be required. Even though the transmitter and receiver of such a system have been demonstrated digitally in this thesis with high sampling rate equipment, an analog solution for this low cost system is feasible and would be an interesting potential future research direction. It would be also interesting to develop the efficient analog circuitry for the functional blocks in this transceiver such as the pilot adding block for transmitter, clock recovery, match filter, etc.

6.2.3 Optical packet switching networks perspective

Developing advanced DSP to reduce the required settling time after the wavelength switching event for optical packet would require further investigation. The complex algorithms to compensate for the strongly fluctuating parameters during the transient time of the optical packet such as frequency, phase or polarization (in fully coherent systems) would need to be improved to increase the efficiency while reducing the computational cost. Adaptive modulation formats would also be a good solution to pursue in the future research to solve these problems.

The optical packet switching transportation networks would require a more efficient architecture for the upper network layers such as the network management layer. Software Defined Networks (SDN), which currently attracts considerable research and development effort, could be intensively investigated to adapt with this future optical network configuration. In addition, for future systems involving space-division-multiplexing, the network configuration would become very complex and that would also require an optimal network architecture design.

Appendix A

List of peer reviewed publications

Journals

1. **Tam N. Huynh**, An T. Nguyen, Wing-Chau Ng, Lim Nguyen, Leslie A. Rusch, Liam P. Barry, "*BER Performance of Coherent Optical Communications Systems Employing Monolithic Tunable Lasers With Excess Phase Noise,*" IEEE/OSA Journal of Lightwave Technology, vol. 32, no. 10, pp. 1973-1980, May 2014.

2. R. Zhou, **T.N. Huynh**, V. Vujicic, P.M. Anandarajah, L.P. Barry, "*Phase noise analysis of injected gain switched comb source for coherent communications,*" OSA Optics express, vol. 22, no. 7, pp. 8120-8125, Apr 2014.

3. **Tam N. Huynh**, Seán Ó Dúill, Lim Nguyen, Leslie A. Rusch and Liam P. Barry, "*A Simple Analytical Model for Low Frequency FM-Noise of Monolithic Tunable Lasers*," OSA Applied Optics, vol. 53, no. 5, pp. 830-835, Feb 2014.

4. **Tam N. Huynh**, Lim Nguyen, Vidak Vujicic and Liam P. Barry, "*Pilot-Tone Aided Transmission of High-Order QAM for Optical Packet Switched Networks*," IEEE/OSA Journal of Optical Communications and Networking, vol. 6, no. 2, pp. 152-158, Feb 2014.

5. Seán Ó Dúill, Sepideh T. Naimi, Aravind P. Anthur, **Tam N. Huynh**, Deepa Venkitesh, and Liam P. Barry, "*Simulations of an OSNR-Limited All-Optical Wavelength Conversion Scheme,*" IEEE Photonics Technology Letters, vol. 25, no. 23, pp. 2311-2314, Dec 2013.

6. Aravind P. Anthur, Regan T. Watts, **Tam N. Huynh**, Deepa Venkitesh,

Liam P. Barry, "*A general phase noise relationship for four-wave mixing,*" arXiv.org, arXiv:1308.0914, Aug 2013.

7. **Tam N. Huynh**, Lim Nguyen, Liam P. Barry, "*Phase Noise Characterization of SGDBR Lasers using Phase Modulation Detection Method with Delayed Self-Heterodyne Measurements,*" IEEE/OSA Journal of Lightwave Technology, vol. 31, no. 8, pp. 1300-1308, Apr 2013.

8. **Tam N. Huynh**, Frank Smyth, Lim Nguyen, Liam P. Barry, "*Effects of phase noise of monolithic tunable laser on coherent communication systems,*" OSA Optics Express, vol. 20, no. 26, pp. B244-B249, 2012.

9. J. O'Carroll, R. Phelan, B. Kelly, D. Byrne, **T.N. Huynh**, B. Cardiff, F. Smyth, P.M. Anandarajah, L.P. Barry, "*Narrow Linewidth Discrete Mode Laser Diodes for Coherent Communications Applications,*" IEEE/OSA Journal of Optical Communications and Networking, vol. 4, no. 9, pp. A90-A96, 2012.

10. J.A. O'Dowd, K. Shi, A.J. Walsh, V.M. Bessler, F. Smyth, **T.N. Huynh**, L.P. Barry, A.D. Ellis, "*Time resolved bit error rate analysis of a fast switching tunable laser for use in optically switched networks,*" IEEE/OSA Journal of Optical Communications and Networking, vol. 4, no. 9, pp. A77-A81, 2012.

11. Q. Lu, W. Guo, A. Abdullaev, M. Nawrocka, **T.N. Huynh**, J. O'Callaghan, M. Lynch, V. Weldon, L.P. Barry, J.F. Donegan, "*Two-Section Single Mode Lasers Based on Slots Suitable for Photonic Integration,*" IEE Electronic Letters, vol. 48, no. 15, 2012.

12. **Tam N. Huynh**, Lim Nguyen, Liam P. Barry, *"Novel coherent self-heterodyne receiver based on phase modulation detection,"* OSA Optics Express, vol. 20, no. 6, pp. 6610-6615, 2012.

13. **Tam N. Huynh**, Lim Nguyen, Liam P. Barry, "*Delayed Self-Heterodyne Phase Noise Measurements with Coherent Phase Modulation Detection,*" IEEE Photonics Technology Letters, vol. 24, no. 4, pp. 249-251, 2012.

14. K. Shi, R. Watts, D. Reid, **T. Huynh**, C. Browning, A.Prince, F. Smyth, L. Barry, "*Dynamic Linewidth Measurement Method via an Optical Quadrature Frontend,*" IEEE Photonics Technology Letters, vol. 23, no. 21, pp. 1591-1593, 2011.

Conferences

1. **Tam N. Huynh** and Liam P. Barry, *"Overcoming the Effect of Cycle Slips Caused by Low Frequency Noise from Monolithic Tunable Lasers ,"* OFC/NFOEC 2017, paper W4K.5, USA, Mar 2014.

2. **T. N. Huynh**, L. Nguyen, Vidak Vujicic, L. P. Barry, *"Baudrate-Pilot-Aided tranmission for high oder QAM modulation format in optical communications,"* Photonics Ireland Conference 2013, Sep 2013, Belfast, Northern Ireland (Best Poster Award).

3. Anthony Walsh, **Tam Huynh**, James Mountjoy, Anthony Fagan, Andrew Ellis, and Liam P. Barry, '*Employing DDBPSK in Optical Burst Switched Systems to Enhance Throughput*', ECOC 2013, paper P.3.17, London, UK, Sept 2013.

4. Rui Zhou, Vidak Vujicic, **Tam N. Huynh**, Prince M. Anandarajah, and Liam P. Barry, '*Effective Phase Noise Suppression in Externally Injected Gain Switched Comb Source for Coherent Optical Communications*', ECOC 2013, paper P.2.5, London, UK, Sept 2013.

5. Wing-Chau Ng, **Tam N. Huynh**, An T. Nguyen, S. Ayotte, C.S. Park, Liam P. Barry, Leslie A. Rusch, *"Improvement due to Optically Filtered Lasers in Parallel Decision-Directed Phase Recovery for 16-QAM ,"* Opto-Electronics and Communications Conference / Photonics in Switching Conference 2013, paper WR3-2, Japan, Jul 2013.

6. **Tam N. Huynh**, Wing-Chau Ng, An T. Nguyen, Lim Nguyen, Leslie A. Rusch, Liam P. Barry, *"Tracking Excess Noise from a Monolithic Tunable Laser in Coherent Communication Systems,"* OFC/NFOEC 2013, paper JW2A.46, USA, Mar 2013.

7. **T.N. Huynh**, F. Smyth, L. Nguyen, L.P. Barry, *"Effects of SGDBR Laser Phase Noise on Coherent Communication Systems,"* ECOC 2012, paper P2.09 , Netherlands, Sep 2012.

8. **T.N. Huynh**, J. O'Carroll, F. Smyth, K. Shi, L. Nguyen, P. Anandarajah, R. Phelan, B. Kelly, L.P. Barry, *"Low linewidth lasers for enabling high capacity optical communication systems,"* International Conference on Transparent Optical Networks 2012, paper Mo.C4.2, UK, July 2012 (invited).

9. **Tam Huynh**, Rui Zhou, Sylwester Latkowski, Frank Smyth, Liam Barry, Prince Anandarajah, *"Multi-Carrier Transmitter for Future Access Networks,"* International Conference on Transparent Optical Networks 2012, paper We.D3.2, UK, July 2012 (invited).

10. **T. N. Huynh**, L. Nguyen, L. P. Barry, *"Self-heterodyne optical transceiver with PM detection and phase compensation for pre-coded differential QAM,"* International Conference on Communications and Electronics, pp. 54-58, Vietnam, Aug 2012.

11. **T. N. Huynh**, L. Nguyen, L. P. Barry, *"A Novel Phase Modulation Detection Technique For Coherent Self-Heterodyne Optical Receiver,"* Signal Processing in Photonic Communications 2012 - OSA, paper SpW2B.2, USA, June 2012.

12. **T. N. Huynh**, L. Nguyen, K. Shi, L. P. Barry, *"Coherent phase modulation detection for selfheterodyne phase noise measurement,"* Asia Communications and Photonics Conference & Exhibition, Proc. SPIE 8309, paper 830920, China, Nov 2011.

13. **T. N. Huynh**, L. Nguyen, L. P. Barry, *"Coherent Delayed Self-Heterodyne Measurement of Laser Phase Noise,"* International Photonics & OptoElectronics Meetings, Proc. SPIE 8331, paper 83313, China, Nov 2011 (Best Paper Award).

14. **T. N. Huynh**, L. Nguyen, L. P. Barry, *"Coherent Optical Receiver using Phase Modulation Detection,"* 2011 IEEE Photonics Conference, paper ThL5, USA, Oct 2011.

15. **T. N. Huynh**, L. Nguyen, L. P. Barry, *"Laser phase noise measurement with novel Coherent Self-heterodyne technique,"*, Photonics Ireland Conference 2011, Ireland, Sep 2011.

16. **T. N. Huynh**, K. Shi, F. Smyth, L.P. Barry, "*DQPSK Optical Packet Switching using an SG-DBR laser*," CLEO/Europe and EQEC 2011 Conference, paper CI1_4, Munich, Germany, May 2011.